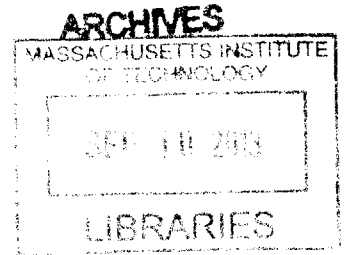


# Polarimetry Measurements of Current Density Profile and Fluctuation Changes during Lower Hybrid Experiments on Alcator C-Mod

by

Peng Xu

B.E. (2005), M.E. (2007), Engineering Physics  
Tsinghua University, China



Submitted to the Department of Physics  
in partial fulfillment of the requirements for the degree of  
Doctor of Philosophy

at the

MASSACHUSETTS INSTITUTE OF TECHNOLOGY

September 2013

© Massachusetts Institute of Technology 2009. All rights reserved.

Author.....

.....  
Department of Physics  
June 17, 2013

Certified by.....

.....  
Earl S. Marmor  
Senior Research Scientist, Department of Physics  
Thesis Supervisor

Certified by

.....  
~~Principal Research Engineer, Plasma Science and Fusion Center~~  
James H. Irby  
Thesis Supervisor

Accepted by.....

.....  
John Belcher  
Professor of Physics, Associate Department Head for Education



# **Polarimetry Measurements of Current Density Profile and Fluctuation Changes during Lower Hybrid Experiments on Alcator C-Mod**

by

Peng Xu

Submitted to the Department of Physics  
on June 17, 2013, in partial fulfillment of the  
requirement for the degree of  
Doctor of Philosophy

## **Abstract**

As a possible method to achieve steady-state plasma operation in a tokamak fusion reactor, Lower Hybrid Current Drive (LHCD) has been extensively studied on Alcator C-Mod. The measurement of current density profiles (or poloidal magnetic field or safety factor) is essential to the understanding of the LH physics. A polarimeter measures the line-integral of the electron density times the magnetic field parallel to a chord through the plasma, and is capable of deriving the current density profile with multi-chord measurements. A three-chord poloidally viewing far-infrared (FIR) polarimeter has therefore been developed for C-Mod. FIR optics, FIR detectors, electronics and mechanical components were custom designed and fabricated. Various sources of vibrations and systematic errors have been carefully dealt with.

A synthetic polarimeter signal has been derived from density profiles from Thomson scattering and magnetic field profiles from EFIT. The polarimeter results confirm that the magnetic field profiles from Kinetic EFIT (with Motional Stark Effect and plasma pressure constraints) is much more accurate than those from normal EFIT (no internal constraints, central safety factor  $q_0 \sim 0.95$ ) during the LHCD. The polarimeter data were used to constrain  $q_0$ , and the result shows that the current density profile is flattened, and  $q_0$  increases to  $\sim 2$  with strong LHCD.

Experiments during LHCD with a plasma density scan, a current scan, and LH power and phase scans have been carried out. The Polarimetry observations confirm the off-axis current drive, and strongly decreasing driven current when the density exceeds a limit of about  $1.0 \times 10^{20} / \text{m}^3$ . They also indicate that the driven current is closer to the plasma edge for  $I_p \sim 820$  kA than for  $I_p \sim 580$  kA, and that lower LH phasing is preferred for higher current drive efficiency.

The polarimeter is the first diagnostic to measure core magnetic fluctuations in Alcator C-Mod. These include broadband magnetic fluctuations during EDA H-modes that are suppressed with the application of LH power.

Thesis supervisor: Earl S. Marmor  
Title: Senior Research Scientist, Department of Physics

Thesis supervisor: James H. Irby  
Title: Principal Research Engineer, Plasma Science and Fusion Center

Thesis reader: Miklos Porkolab  
Title: Professor of Physics, Department of Physics

Thesis reader: Iain Stewart  
Title: Associate Professor of Physics, Department of Physics

## Acknowledgements

I would like to express my deepest gratitude to my supervisors, Dr. James Irby and Dr. Earl Marmor, for their guidance and support throughout my research at MIT. With great patience, Jim has taught me how good experimental physics should be done. He is always there for me if I have any questions or need any help. Earl has provided insightful discussions and suggestions about the physics of my thesis.

I also would like to thank my thesis readers, Prof. Miklos Porklab and Prof. Iain Stewart, for their valuable suggestions for my research and thesis writing.

I thank all of the Alcator C-Mod members, for their assistant and kind help during the last six years. Without the contributions from Rick Murray, Rick Leccacorvi, Rui Viera, Ed Fitzgerald, Bill Parkin, Joe Bosco, Tom Toland, Gary Dekow, Yuri Rokhman, Andy Pfeiffer, Lihua Zhou and many other talented engineers and technicians, it would be impossible to turn the idea of the polarimeter into an operational system. Also, many professors, scientists and fellow graduate students helped me with experiments and analyzing the C-Mod data, and I could only list a few of them here: Chi Gao, Seung Gyou Baek, Yunxing Ma, Syun'ichi Shiraiwa, Steve Wolfe, Cornwall Lau, Robert Mumgaard, Greg Wallace, Jerry Hughes, Liang Lin, Ron Parker, Steve Scott, John Walk, Yijun Lin, Jim Terry, Ted Golfinopoulos, Choongki Sung, Arturo Dominguez, and Darin Ernst.

I also thank collaborates from UCLA: Will Bergerson, David Brower and Weixing Ding. Will has been very supportive in both improving the polarimeter system and discussing the data.

I would like to thank my parents. Without their support and encouragement, I would not have come to study in the US. Finally, a special thanks to my wife, Ziqiu and son, Guangyan, for giving me so much love and happiness, which helped me go through all the difficulties.



# Contents

<b>1. Introduction.....</b>	<b>21</b>
1.1 Thermal Nuclear Fusion.....	21
1.2 Tokamak.....	24
1.3 Alcator C-Mod .....	26
1.3.1 Machine Parameters and Geometry .....	26
1.3.2 C-Mod Diagnostics .....	29
1.4 Lower Hybrid Current Drive.....	34
1.4.1 Basic Theory .....	35
1.4.2 C-Mod LH System .....	37
1.5 Motivations for Polarimetry Studies .....	39
1.6 Thesis Outline .....	40
<b>2. Basic Polarimetry Theory .....</b>	<b>43</b>
2.1 Basic Polarimetry Theory.....	44
2.1.1 Dispersion Relations .....	44
2.1.2 Limiting Cases.....	47
2.1.3 Normal Case .....	50
2.2 Review of Polarimetry Techniques.....	52
2.2.1 Different Beam Modulation Methods .....	52
2.2.2 Different Viewing Geometries .....	60
2.3 Current Density Profile .....	61

<b>3. Development of the Polarimeter Diagnostic on C-Mod .....</b>	<b>65</b>
3.1 Measurement Scheme and System Geometry .....	65
3.1.1 Schematic Measurement Scheme .....	65
3.1.2 Three-Chord Geometry .....	66
3.2 Instrumental Design .....	70
3.2.1 Laser Wavelength Selection.....	70
3.2.2 FIR Laser System .....	73
3.2.3 Gaussian Beam Propagation.....	78
3.2.4 Quartz Vacuum Window and Waveplates .....	79
3.2.5 Copper Mesh Beam Splitter .....	82
3.2.6 Focusing Elements .....	85
3.2.7 Retro-reflectors and Protecting Shutter.....	85
3.2.8 Mixers.....	88
3.3 Phase Analysis.....	91
3.3.1 Digital Phase Comparator .....	91
3.3.2 Analog Phase Comparator.....	93
<b>4. Polarimetry Noise Improvements and Performance Analysis.....</b>	<b>95</b>
4.1 Noise Improvements .....	96
4.1.1 Acoustic Noise .....	96
4.1.2 Mechanical Vibration Noise.....	97
4.1.3 IF Stabilization .....	99
4.1.4 Laser Beam Co-linearity .....	99
4.1.5 Spurious Reflections .....	100
4.1.6 TF Ramp-Induced Error .....	102
4.1.7 TF Effect .....	105
4.2 Calibration.....	106

4.3	Measurement Performance Analysis.....	108
4.3.1	Density Sensitivity .....	108
4.3.2	Plasma Current Sensitivity .....	111
4.3.3	Plasma Position Sweep.....	112
4.3.4	Sawtooth Crashes .....	115
<b>5.</b>	<b>LHCD Experimental Results .....</b>	<b>121</b>
5.1	A Typical LHCD Discharge.....	122
5.2	LHCD Experiments.....	126
5.2.1	LH Power and Pulse Scan .....	126
5.2.2	Plasma Density Scan .....	130
5.2.3	Plasma Current Scan .....	136
5.2.4	LH Launcher Phase Scan .....	141
5.3	Validate Kinetic-EFIT .....	149
5.3.1	Synthetic Polarimeter Signals from EFIT and TS.....	149
5.3.2	Faraday Rotation Measurements Compared with EFIT Prediction ...	150
5.3.3	C-M Measurements Compared with EFIT Predictions.....	156
5.4	Incorporating Polarimeter Data into EFIT to Constrain $q_0$ .....	158
<b>6.</b>	<b>Polarimetry Measured Fluctuations .....</b>	<b>163</b>
6.1	LH Waves Alter Fluctuations during EDA H-mode.....	164
6.2	I-mode Fluctuations.....	170
<b>7.</b>	<b>Summary and Future Work .....</b>	<b>175</b>
7.1	Summary .....	175
7.2	Future work .....	177



# List of Figures

Figure 1-1: Schematic of the tokamak with magnetic coils, toroidal plasma current and magnetic fields (Figure from [6]) ..... 25

Figure 1-2: Alcator C-Mod poloidal cross-section with magnetic flux surfaces, divertor, outboard limiter (for a secondary protection of the plasma heat flux), inner wall and vacuum vessel. .... 28

Figure 1-3: C-Mod cross section with locations of the certain measurements. .... 33

Figure 1-4: Contours of the electron velocity distribution function, when the parallel LH phase velocity is  $\sim 3-5$  times of the electron thermal velocity ( $v_T$ ) (Figure from [22]) .... 36

Figure 1-5: Model drawing of the LH2 launcher ..... 38

Figure 1-6: In vessel view of the installed LH2 launcher ..... 38

Figure 2-1: Coordinate system ..... 46

Figure 2-2: Schematic drawing of the polarimetry/interferometry system on TEXTOR with the linearly polarized beam measurement technique (Figure from [33]) ..... 54

Figure 2-3: Schematic drawing of the Polarimetry/Interferometry system on MTX with a rotating elliptically polarized beam measurement technique (Figure from [34]). .... 55

Figure 2-4: Simulated time history of the polarimetry waveforms. The phase of the 1MHz IF contains the interferometry information. The phase difference between the envelopes of the reference detector and the probing detector is twice the Faraday rotation  $\alpha$  (Figure from [46]) ..... 56

Figure 2-5: Schematic of the PEM polarimeter configuration on C-Mod. (Figure from [49]). .... 60

Figure 3-1: Schematic design for the polarimetry system on C-Mod ..... 66

Figure 3-2: System geometry for the three-chord double-pass polarimeter on C-Mod. To simplify the optical path in the figure, only the beam for one chord (red line) is shown. 68

Figure 3-3: Optical layout on the upper table. Yellow lines are beam paths. The beam from the lower table is split into a reference and three probe beams by beam-splitters (BS). Each chord has a quartz-waveplate to transfer beams into circularly-polarized beams and a TPX lens to focus the beams onto the retro-reflectors. .... 69

Figure 3-4: Poloidal cross section of the magnetic flux on C-Mod. The viewing paths for six available chords are shown. All of them are above the vessel midplane. The top chord with retro-reflector at  $z=0.39$  m ( $x=35$  cm) views outside of the last closed flux surface (LCFS). During operations, chords with  $x=10$  (#1) and 16 (#2) cm are always used, and the third channel (#3) is typically alternated between  $x=20$  and 23 cm. .... 70

Figure 3-5: FIR#1 has a peak power for  $p\sim 650$  mTorr, while FIR#2 has a peak power for  $p\sim 750$  mTorr ..... 73

Figure 3-6: Air tight enclosure for the lower table. Detachable side panels in the enclosures provide good accessibility for optical adjustments ..... 74

Figure 3-7: Air tight enclosure for the upper table. The tube connecting the two enclosures is shown. Detachable side panels in the enclosures provide good accessibility for optical adjustments ..... 75

Figure 3-8: Resonant peaks found on IF signal, when driving the PZT with input signals near 235 Hz (FIR#1) or 210 Hz (FIR#2). The Y axis is the change in the signal IF frequency for 1 mV of drive to the PZT. .... 76

Figure 3-9: (a) Significant drift on IF ( $>1$  MHz) and detector RMS voltage dropped to near zero without magnetic shielding (b) Minor drifts on IF ( $< 80$  kHz) and detector RMS voltage with magnetic shielding ..... 77

Figure 3-10: Both lasers boxed in a steel enclosure to reduce the stray field effects ..... 78

Figure 3-11: Gaussian Beam radius along the laser beam path. .... 79

Figure 3-12 : Comparison of the transmission rate of the quartz window with and w/o AR coating ..... 81

Figure 3-13: Mesh transmission for different mesh spacings and two linearly polarized incident beams (H: horizontal polarized incident beam, V: vertical polarized incident beam). The number, such as 70, specifies the lines-per-inch(LPI) for the mesh. The mesh is mounted at a  $45^\circ$  angle of incident, and is rotated over  $90^\circ$  in the holder to sweep out the curve. .... 83

Figure 3-14: Transmitted orthogonal component for horizontal (square) and vertical (circle) polarized incident beam; reflected orthogonal component for horizontal (plus) and vertical (diamond) polarized incident beam ..... 84

Figure 3-15: (a) Glass retro-reflector with gold coating (b) Prototype molybdenum retro-reflector with gold coating ..... 86

Figure 3-16: (a) Plasma facing side of the shutter assembly showing protection tiles and location of the retro-reflectors (b) Inner wall side of the shutter assembly showing the push-pull bellows. .... 87

Figure 3-17: C-Mod inner wall with six retro-reflectors. The shutter is open, and we can see all six retro-reflectors..... 88

Figure 3-18: Figure 3-18: Four mixers tested. (a) Farran Corner-cube Mixer (optimal operation for 100-150  $\mu\text{m}$ ) (b) Corner-cube Mixer for 180  $\mu\text{m}$  (loan from UCLA) (c) Waveguide coupling mixer from Radiometer-Physics (d) Planar diode mixer (developed by VDI for our wavelength at 117.73  $\mu\text{m}$  ) ..... 90

Figure 3-19: (a) Micrograph of the planar Schottky diode and a portion of the coupling structure (b) Pyramidal horn where FIR power couples through ..... 90

Figure 3-20: Faraday rotation from both digital and analog comparators for shot 1110113010. Analog phase from the XOR circuit agrees perfectly with the digital phase. .... 94

Figure 4-1:  $\pm 0.3^\circ$  Faraday rotation phase error when a panel is off the enclosure (black curve). Smaller phase error with the enclosure closed (red curve)..... 97

Figure 4-2: TF-only test shot. The Faraday rotation has a  $\sim 0.5^\circ$  slow drift during the TF ramps, but it is close to zero during the TF flattop, indicating the phase error is sensitive to the magnetic field change, but not the magnetic field itself. .... 102

Figure 4-3: Three-chord measurements with improved baselines before the plasma (-0.2 to 0 s), by adjusting the TF ramp starting time 0.1 s earlier than usual. The shadowed area is expanded and compared with another shot with noisy baselines in Figure 4-4..... 104

Figure 4-4: Baseline comparison for three discharges with normal TF ramp (black curve) and adjusted TF ramp (red and blue curves). For the adjusted cases, the TF ramp-up starts 0.1 seconds earlier than normal, so that flat-top is reached by  $t \approx -0.2$  s for the red shot and by  $t \approx -0.3$  s for the blue shot. (Polarimeter only records signals from -0.2 to 2.2 s at 20 MHz, due to the limitation of the digitizer memory)..... 105

Figure 4-5: Faraday rotation signals are the same for two shots while the density and current are the same (shaded region).  $B_t=7.5$  T for the black curve, and  $B_t=5.4$  T for the red curve. No significant TF misalignment or C-M effect was observed..... 107

Figure 4-6: System calibration with a rotating half-waveplate. The measured phase responds linearly to the half-waveplate rotation angle, with an error of less than 5% for all three chords, when the mesh grid of the beam-splitter is set at  $45^\circ$ . The measured phase shows significant non-linearity, with large systematic error, when the mesh grid of the beam-splitter is far away from  $45^\circ$  (purple). ..... 108

Figure 4-7: Faraday rotation (chord#1) shows similar spikes as on the density trace, during the flat-top of the plasma current..... 109

Figure 4-8: H-modes observed on three-chord Faraday rotation signals, with a similar shape as the density trace during the current flat-top. .... 110

Figure 4-9: A zeroth-order check on polarimetry sensitivity to the changes in the plasma current. Discharges with reversed plasma current show the Faraday rotation reverses sign. .... 111

Figure 4-10: Plasma current ramps down from 680 to 440 kA (1.51 to 1.7 s), with relatively constant line averaged electron density. The plasma minor radius reduces  $\sim 1.1$  cm (5%). This process is during the flat-top for  $B_t$ , so there is no phase error due to a  $B_t$  ramp. .... 113

Figure 4-11: (a) C-Mod poloidal magnetic flux at  $t=0.6$  s for shot 1120516020. The red contour indicates the LCFS, and the green lines are the three polarimetry chords. (b) C-Mod poloidal magnetic flux at  $t=1.6$  s for shot 1120516020. (c) Major radius of the LCFS reduces  $\sim 10$  cm during plasma sweeping for 1120516019 (black) & 1120516020 (red) ..... 114

Figure 4-12: Three-chord Faraday rotation measurements for two plasma sweep discharges, 1120516019 (black) & 1120516020 (red). Plasma is shrinking while maintaining density and current in the core, as implied by the polarimetry and TCI measurements..... 116

Figure 4-13: Effects of sawtooth crashes on the polarimeter Faraday rotation angle. The angle on chord#1 increases during each crash..... 118

Figure 4-14: Sawtooth crash effect seen on all three polarimetry chords (1120621019). For this shot, the Faraday rotation drops for chord#1, and increases for other two chords during each crash. .... 119

Figure 5-1: A typical LHCD discharge (shot 1120612027). Loop voltage drops in magnitude during LHCD, since some of the Ohmically driven current is replaced by LH driven current. Sawtooth oscillations, as measured with soft x-rays, are seen to disappear after the LH turn-on. .... 124

Figure 5-2: Current density and safety factor ( $q$ ) profiles at three time-slices from Kinetic-EFIT: before the LH ( $t= 0.72$  s, black traces), during the LH ( $t=1.32$  s, red traces) and after the LH ( $t= 1.72$  s, blue traces). The LH pulse is from 0.8-1.4 s. .... 125

Figure 5-3: Faraday rotation time traces (FR#1) for shots 1120612002, 1120612003 and 1120612005 with LH pulse scan. The LH power is 600 kW, 700 kW and 800 kW respectively, and the LH turns off at different times. The Faraday rotation immediately starts to responds to the changes in LH power. .... 129

Figure 5-4: Faraday rotation changes for all three chords with shot-by-shot LH power scans. The systematic increase of rotation angle is clearest for the innermost chord (#1). .... 130

Figure 5-5: For LHCD discharges with densities below about  $1 \times 10^{20} \text{ m}^{-3}$ , HXR count rates drop at approximately the expected exponential rate as a function of line average density. At higher densities, the fall-off becomes unexpectedly rapid, and LHCD efficiency on C-Mod is weak above this density threshold. (Figure from [81])..... 131

Figure 5-6: Four consecutive discharges with a shot-by-shot density scan ( $0.4$  to  $0.7 \times 10^{20} / \text{m}^2$ ).  $I_p=580$  kA, LH=800 kW. Strong LHCD effect observed on FR#1, for low density shots (black and red), very weak LHCD effect observed for shot over the density limit (green shot). .... 133

Figure 5-7: Faraday rotation change during the LHCD for a shot-by-shot density scan. Both the change of FR#1 and FR#2 decrease with higher density ..... 134

Figure 5-8: HXR count rate as a function of the line averaged density. Inner wall limited discharges (blue starts) has higher count rate than the diverted discharges with large and small (3-5 mm) inner gaps. (Figure from [79])..... 135

Figure 5-9: Time traces of a high density limited discharge (red) are compared with a diverted discharge (black). Some weak LHCD for the limited discharge is observed by the polarimeter, which is qualitatively consistent with non-thermal ECE measurements. .... 136

Figure 5-10: LHCD power deposition for 300 kA (red) and 800 kA (black) discharges, simulated by GENRAY/CQL3D. LH deposits more power close to the edge for high current shot. (Figure from [82])..... 137

Figure 5-11: Different LHCD effects are observed by the polarimeter for shots with  $I_p=580$  kA (black, red) and  $I_p=800$  kA (blue, green) ..... 139

Figure 5-12: Faraday rotation changes for the four discharges in Figure 5-11. FR #1 has a significant change for both the low and high current shots, while FR #2 sees a big drop only for the high current shots ( $I_p=820$  kA)..... 140

Figure 5-13: Two similar LHCD discharges. FR#1 shows a better sensitivity to the current profile changes than  $V_{loop}$ . .... 141

Figure 5-14: GENRAY/CQL3D simulation shows LH deposits more power and thus more driven current close to the edge for lower antenna phasing. (Figure from [80])... 142

Figure 5-15: The current density profiles flatten with decreased launched phase, as inferred from Kinetic-EFIT reconstructions with MSE constraints (Figure from [69]) 143

Figure 5-16: Faraday rotation on chord#1 with a shot-by-shot LH phasing scan ( 1120912017, 1120912012, 1120912021, 1120912024 with  $75^\circ$ ,  $90^\circ$ ,  $105^\circ$  and  $115^\circ$  phasing respectively).  $N_{I04} \approx 4 \times 10^{19}/m^2$ ,  $I_p \approx 600$  kA, and LH  $\approx 600$  kW. .... 144

Figure 5-17: FR#1 change decreases with higher LH phasing, which agrees with LH theory. .... 145

Figure 5-18: LH phase scan within one shot:  $115^\circ$ ,  $105^\circ$ ,  $90^\circ$ ,  $75^\circ$ . The magnitude of the time derivative of FR#1 becomes larger when the LH phasing decreases. .... 147

Figure 5-19: The slope of FR#1 by linear regression for different LH phases (the slope for  $115^\circ$  LH phasing is calculated near  $t=1.2$  s). Larger slope for lower phasing shows that lower phase yields higher LHCD efficiency..... 148

Figure 5-20: Linear least squares fitting between the FR#1 slope and  $1/n_{||}^2$ . .... 148

Figure 5-21: Faraday rotation measurements agree well with the synthetic signals calculated by EFIT and TS density, for all three chords. Shot 1120216017,  $I_p=1.1$  MA,  $n_{l04}$  ramps from  $0.4$  to  $0.9 \times 10^{20}/m^2$  during the current flat top. .... 151

Figure 5-22: Faraday rotation measurements agree well with the synthetic signals calculated by EFIT and TS density, for all three chords. Shot 1120216003,  $I_p=1.1$  MA,  $n_{l04}$  ramps from  $0.3$  to  $0.5 \times 10^{20}/m^2$  during the current flat top. .... 152

Figure 5-23: Comparison between the measurements and the EFIT predictions for a LHCD discharge. FR#1 shows a big discrepancy between two traces, which confirms the poloidal magnetic field from normal EFIT is inaccurate during LHCD . .... 154

Figure 5-24: Comparison between the measurements and the EFIT predictions for a LHCD discharge. The FR#1 shows a big discrepancy between two traces..... 155

Figure 5-25: Faraday rotation agrees with the prediction from Kinetic-EFIT (blue squares, 100 ms resolution). The discrepancy between measurement and Kinetic-EFIT prediction is much smaller than that from the normal EFIT during the LH pulse..... 156

Figure 5-26: a) C-M effect measurement (black) with the EFIT prediction (red); b) Faraday effect measurement (black) with the EFIT prediction (red). Agreement is reasonably good for both C-M and Faraday effects..... 158

Figure 5-27: Large differences are observed between measurement (black curve in 3<sup>rd</sup> frame) and normal EFIT prediction (blue curve) for FR#1 during LHCD.  $q_0$  was chosen to minimize the difference between the measurements and EFIT predictions (green curve). .... 160

Figure 5-28: Current density (a) and safety factor (b) profiles for three time-slices, before the LH at  $t= 0.6$  s (red), during the LH at  $t=1.2$  s (blue) and after the LH at  $t=1.5$  s (green). .... 161

Figure 6-1: (a) Three-chord polarimetry fluctuation measurements with the EDA H-mode. Polarimetry observed QCM mode is consistent with PCI and reflectometer measurements in (b). Higher frequency broadband fluctuations are only found on core channels (#1, #2). (b) QCM on PCI and reflectometer signals. A second order harmonic of the QCM is shown on reflectometer..... 166

Figure 6-2: (a) With 600 kW LH applied during the EDA H-Mode, the QCM drifts down in frequency and becomes more coherent. (b) The fluctuation intensity integrated over

250-600 kW is reduced with LH. Sawtooth crashes are seen on the integrated fluctuation intensity. The plasma stored energy from EFIT and the core toroidal rotation increase, and the line averaged density decreases, during the LH. .... 168

Figure 6-3: LH power scan for four discharges(0, 300, 500 and 600 kW). As the LH power is increased, so too does the downshift in frequency for the QCM mode, while the broadband fluctuations decrease. .... 169

Figure 6-4: The broadband fluctuation intensity (integrated over 250-600 kHz) decreases as the LH power is increased. .... 170

Figure 6-5: Poloidal asymmetry of WCM during I-mode observed by polarimeter. (Figure from [110])..... 172

Figure 6-6: NTMs shown on polarimetry, with the same frequencies as the magnetic coil measurements, during I-mode. (Figure from [110]) ..... 172

# List of Tables

Table 1-1: Alcator C-Mod Parameters.....	27
Table 3-1 : Laser wavelength selection. Shot# 1080320019 (L-mode) at $t=1.0$ s, $n_{l04}\approx 0.5\times 10^{20}/\text{m}^2$ , $I_p\approx 830$ kA, $B_t=6.2$ T. (Phase signals are for chord#1. Refraction is the max beam displacement on inner wall) .....	72
Table 3-2: Laser wavelength selection. Shot# 1120614012, $t=1.0$ s (H-mode), $n_{l04}\approx 2.9\times 10^{20}/\text{m}^2$ , $I_p\approx 830$ kA, $B_t= 5.2$ T. (Phase signals are for chord#1. Refraction is the max beam displacement on inner wall) .....	72
Table 3-3: Comparisons of four Schottky diode mixers.....	91



# 1. Introduction

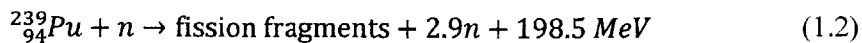
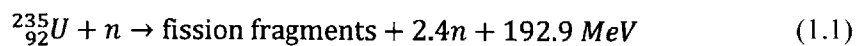
Since the fossil fuels on the earth may only last hundreds of years according to the projected world energy consumption rate, future generations could face an energy shortage, if we do not find new energy sources.

Besides the renewable sources of power from the sun and wind, nuclear energy is a candidate with great potential. There are two kinds of nuclear energy: fission and fusion. There are over 400 fission power plants operational around the world, which provided 13% of the world's electricity in 2012. The physics and engineering of a fusion reactor are much more complicated, and are still under development by fusion scientists and engineers.

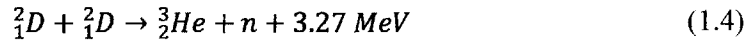
In section 1.1, we will introduce the basics of thermal nuclear fusion, including its benefits, challenges and possible ways of implementation. Section 1.2 introduces the concept of the tokamak. Section 1.3 introduces Alcator C-Mod and some plasma diagnostics that have been extensively used in this thesis. The Lower Hybrid Current Drive (LHCD) system used to drive the non-inductive current in C-Mod will be discussed in section 1.4. Finally, we will present the motivation and outline of the thesis.

## 1.1 Thermal Nuclear Fusion

Both nuclear fusion and fission reactions release a large amount of energy resulting from the transformation of the atomic mass into energy. During nuclear fission, heavy nuclei, such as  $^{235}_{92}\text{U}$  and  $^{239}_{94}\text{Pu}$ , break into lighter ones by reacting with thermal neutrals. Two typical fission reactions are shown below. Because there are many possible fission products, we only list an average number of the ejected neutrons and released energy.



Fusion is a nuclear process in which two light nuclei fuse into a heavier one. While there are many possible fission reactions, researches mainly focus on the following two:



where deuterium ( ${}^2_1\text{D}$ ) and tritium ( ${}^3_1\text{T}$ ) are isotopes of hydrogen. These reactions are preferred because they have relatively large cross sections, high energy gain, and require relatively low incident energies.

In theory, there is unlimited fuel for fusion reactions. Deuterium is a natural isotope, with an abundance of ~0.01% in hydrogen. We could extract ~10 mg of deuterium from a kg of water, which could release the energy equal to 300 kg of gasoline through deuterium-deuterium (D-D) fusion. Therefore, the deuterium from the ocean is enough to power our needs for billions of years. Tritium has a short half-life of ~12 years, and thus does not naturally exist. It can be bred by bombarding lithium with neutrons in fission or fusion reactors through one of the following reactions.



Fusion energy has some advantages over fission. Fusion energy is more efficient than the fission energy with about 4 times the energy density by weight as fission. Fission produces long-lived wastes which have a half-life of millions of years, making the by-product storage a serious problem, while fusion products are primarily helium. However, the walls of a fusion reactor are bombarded by neutrons and become activated. These components typically have a short half-life of ~50-100 years and are confined on the vessel wall, which does not need to be replaced or transported for disposal regularly. Thirdly, there are always criticisms about the safety issue of fission plant, especially after level 7 nuclear accidents, which happened in Chernobyl and Fukushima. Fusion reactors do not have this drawback. It requires precise parameter controls,

such as the current, magnetic field and pressure, to generate and smoothly release the net energy. If any unexpected condition happens, the fusion reactor will just stop operation and cool down by itself.

However, making controlled fusion energy on the earth is extremely difficult. Two nuclei, both with a positive charge, experience a strong repulsive Coulomb force when they are close to each other. Consequently, the nuclei need to have an energy of >10 keV to overcome the Coulomb barrier before they can be captured by the short-range strong nuclear force. The fusion reaction rate is given by

$$R_{ab} = n_a n_b \langle \sigma_{ab} v \rangle \quad (1.7)$$

where  $n_a$ ,  $n_b$  are the densities of two nuclei species and  $\langle \sigma_{ab} v \rangle$  is the cross section averaged over the Maxwellian velocity distribution function with nuclei temperature  $T$ .  $\langle \sigma_{ab} v \rangle$  is peaked at  $T \sim 10-100$  keV (1 keV=11,600 K) depending on nuclei species. At such high temperatures, the fuel atoms are ionized, forming mixed charged particles called a plasma. Some of the generated energy needs to be confined in the plasma, so that it can be used to sustain the fusion reaction without continuous external power input. The energy loss rate is usually quantified as an energy confinement time,  $\tau_e$ , the aggregate time over which the plasma loses all of its stored energy.

Therefore, high density and high temperature plasmas with long energy confinement times are required to achieve a high fusion reaction rate. The Lawson criterion specifies what is needed to achieve break-even in a fusion reactor (energy out = energy in). For D-T fusion, the Lawson criterion [1] is

$$n_e T \tau_E \geq 10^{21} \text{ keV s/m}^3 \quad (1.8)$$

at  $T=20$  keV, where  $n_e$  is the plasma electron density.

There are different ways to confine the plasma and exceed this limit. In the case of the Sun, the plasma is trapped gravitationally because of the Sun's very large mass. We are mainly pursuing two different technologies for earth based reactors, inertial confinement fusion (ICF) and magnetic confinement fusion (MCF).

The idea of ICF is to rapidly compress and heat a pellet of fusion fuel with powerful pulsed laser beams arriving at the target from many directions. The momentum and energy of the laser beams are transferred to the cold pellet, making it extremely dense and hot. The National Ignition Facility (NIF), operated since 2009, is the largest ICF research device in the world, but has not achieved ignition yet [2].

Since the fusion fuel is in a plasma state, it can be controlled by strong magnetic fields by the Lorentz force. Different kinds of MCF machines have been built, such as Stellarators, Tokamaks, Reversed Field Pinches (RFP) and the Levitated Dipole Experiment (LDX) [3]. The tokamak is thus far the most competitive device achieving the best plasma performance.

The fusion energy gain factor  $Q$ , the ratio of the fusion power produced in a reactor to the power required to maintain the steady-state plasma, quantifies the performance of a fusion reactor. The current world record for  $Q$  is 1.25, achieved on JT-60. The next generation fusion machine, the International Thermonuclear Experimental Reactor (ITER) now under construction, is designed with  $Q=10$ . After the successful operation of ITER, a proposed fusion power plant DEMONstration Power Plant (DEMO) would achieve  $Q=25$ . With high  $Q$ , the plasma could be continually heated by the fusion energy itself, and the large amount of net fusion energy could be used to generate electricity.

## **1.2 Tokamak**

The tokamak, which is a Russian acronym based on the words for toroidal magnetic chamber, was invented in the 1950s [4]. It bends the strong magnetic fields ( $B_z$ ) into a toroidal shape, so that the charged particles cycle around the field lines in the chamber and do not suffer end losses.

$B_t$  is usually a few Tesla, and is produced by a set of toroidal field coils as shown in Figure 1-1. The Larmor radius of the charged particles is less than a millimeter with such high field; much smaller than the minor radius of the tokamak,

The plasma is not well confined with only  $B_t$ , since there are particle drifts in the radial direction, such as  $E \times B$ , curvature, and  $\nabla B$  drifts [3][5], due to the asymmetry of the system in the poloidal plane. A toroidal plasma current, which is driven by a central solenoid, is necessary to balance the plasma pressure between the hot core and cooler edge, through Lorentz force. The combination of  $B_t$  and  $B_p$  (poloidal magnetic field from toroidal plasma current) causes field lines to have a helical geometry (black lines in Figure 1-1). An additional vertical field, produced by the equilibrium field (EF) coils, controls the plasma position and shape.

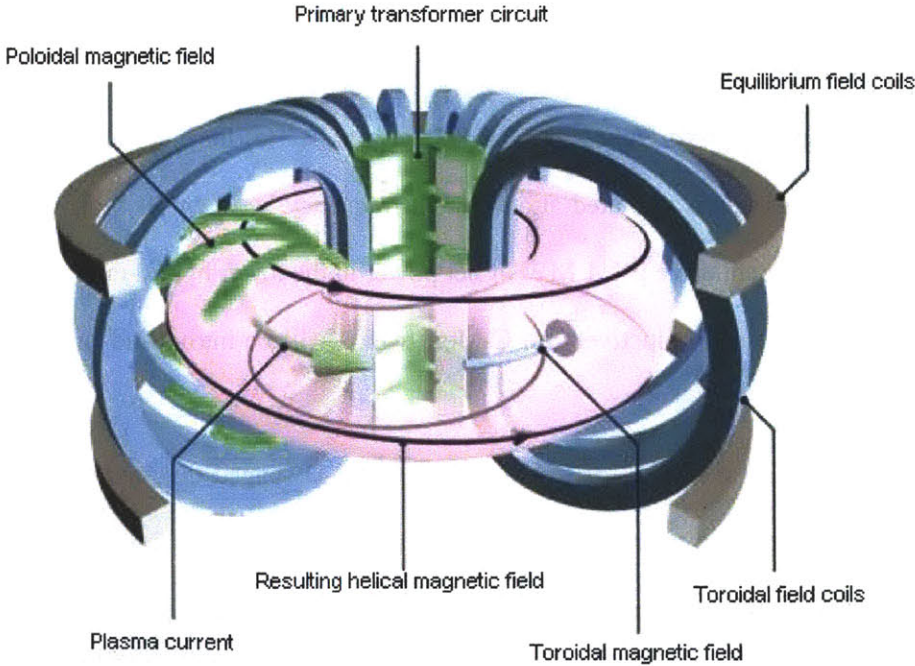


**Figure 1-1: Schematic of the tokamak with magnetic coils, toroidal plasma current and magnetic fields (Figure from [6])**

### 1.3 Alcator C-Mod

Alcator C-Mod [7] is a tokamak which began operation in 1993 at the Plasma Science and Fusion Center (PSFC) at MIT, and is the successor to Alcator A (1973-1979) and Alcator C (1978-1987). It is the largest fusion experiment operated by a university, serving as a training site for the next generation of fusion scientists. The thesis work described here was done on this device.

#### 1.3.1 Machine Parameters and Geometry

The fundamental parameters of C-Mod are listed in Table 1.1. With a compact size, C-Mod has the highest magnetic field and plasma pressure among existing tokamaks, which allows the ability to study a very broad range of plasma conditions. It typically runs at  $B_t=5.4$  T. It takes  $\sim 15$  minutes between plasma discharges to cool down the copper magnetic coils with liquid nitrogen. As a result, there are typically about 30 discharges in a run day. Up to 6 MW of power in the ion cyclotron range of frequencies (ICRF) is coupled for auxiliary plasma heating via three fast wave antennas. Two antennas are operated at 80 MHz for the standard minority heating scenarios: D(H) (minority species in parentheses) for 4.4-6.9 T and D( $^3\text{He}$ ) for high field operation (7.3-8.0 T) [8]. Another Antenna is operated at a variable frequency between 50 MHz and 80 MHz for both heating and current drive [9]. 1 MW of net power in the lower hybrid range of frequencies is used to drive current non-inductively on C-Mod, which will be introduced in detail in the next section.

A poloidal cross section of C-Mod with typical D-shaped diverted plasma is shown in Figure 1-2. The green curves are contours of constant poloidal flux, which are projections of the nested closed magnetic surfaces (produced by helical magnetic field) in the poloidal plane. The red curve is the last closed fluxed surface (LCFS), outside of which the magnetic field lines are open (meaning they intersect material surfaces), and the plasma in this region is lost quickly to the divertor and other metal surfaces. The x-point or null in Figure 1-2 indicates the location where the poloidal field goes to zero. C-Mod can also run limited plasma discharges, in which

case the plasma boundary is defined by the Molybdenum surface on the inner cylinder of the vacuum vessel, known as the limiter. Since impurities generated by material erosion from the limiter can easily get into the confined core plasma, the plasma radiation loss is usually larger for limited discharges than for diverted discharges. Plasma boundary conditions also affect the core plasma, as we will find for the LHCD experiments discussed in chapter 5.

**Table 1-1: Alcator C-Mod Parameters**

Parameter	Symbol	Value
Major radius	$R_0$	0.67 m
Minor radius	$A$	0.22 m
Central toroidal magnetic field	$B_t$	3-8 T
Plasma elongation	$K$	0.9~1.8
Plasma current	$I_p$	0.3-2.1 MA
Central Plasma density	$n_e$	$0.2 - 20 \times 10^{20} /m^3$
Central plasma temperature	$T_e$	0.5-8.0 keV
Plasma pulse length	$t_{pulse}$	<5 s (typically 2s)
Energy confinement time	$\tau_e$	~50 ms
ICRF Power (source)	$P_{ICRF}$	8 MW ( 80/50 MHz )
LH Power (source)	$P_{LH}$	3 MW ( 4.6 GHz )

Quantitatively, the poloidal flux at minor radius  $r$  is defined as

$$\psi(r) = \int_0^r 2\pi(x + R_{axis})B_p(x)dx \quad (1.9)$$

where  $R_{axis}$  is the major radius of the magnetic axis and  $B_p(x)$  is the poloidal magnetic field at minor radius  $x$  on the mid-plane.  $\psi(r)$  increases with  $r$  and reaches the maximum at the plasma edge. It is usually normalized by

$$\psi_{norm}(r) = \frac{\psi(r) - \psi(0)}{\psi(r_{LCFS}) - \psi(0)} \quad (1.10)$$

where  $r_{LCFS}$  is the minor radius at the LCFS. Therefore,  $\psi_{norm} = 0$  at the magnetic axis, and  $\psi_{norm} = 1$  at the LCFS.

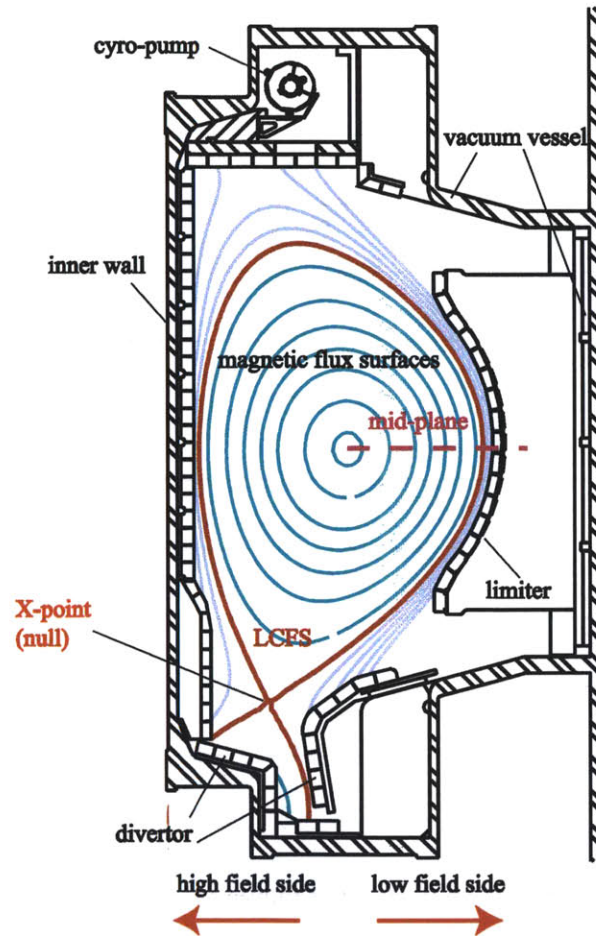


**Figure 1-2: Alcator C-Mod poloidal cross-section with magnetic flux surfaces, divertor, outboard limiter (for a secondary protection of the plasma heat flux), inner wall and vacuum vessel.**

The safety factor ( $q$ ) is related to the twist of the helical magnetic field, the number of toroidal turns the magnetic field line makes when it takes one poloidal turn. For a circular cross-section tokamak plasma with large aspect ratio ( $R_0/a$ ),

$$q(r) \approx \frac{rB_t}{R_0B_p(r)} \quad (1.11)$$

The  $q$  profile usually increases with minor radius, as will be shown in chapter 5. The on-axis safety factor ( $r \rightarrow 0$ ) is

$$q_0 = \frac{rB_t 2\pi r}{R_0 \mu_0 j_0 \pi r^2} = \frac{2B_t}{\mu_0 R_0 j_0} \quad (1.12)$$

where  $j_0$  is the on-axis plasma current density. Since the safety factor profile correlates with the poloidal magnetic field, and therefore the current density profile, it can be measured by the polarimeter as well.

### 1.3.2 C-Mod Diagnostics

To study various aspects of the C-Mod plasma, many diagnostics have been developed [10][11]. We will briefly introduce some of the diagnostics extensively used in this thesis.

#### Motional Stark Effect

The Motional Stark Effect (MSE) diagnostic [10] measures the magnetic pitch angle to infer the current profile. A diagnostic neutral beam (DNB) with energy of 50 keV and  $\sim 10$  cm diameter is injected into C-Mod at the mid-plane with a toroidal angle  $\sim 7^\circ$  off the poloidal plane. When the hydrogen atoms move across the magnetic fields, they experience an electric field given by  $\vec{E} = \vec{V} \times \vec{B}$  in the rest frame of the moving atoms. This electric field produces very large Stark shifts for the energetic hydrogen atoms, which generate a complicated spectrum of light by

interacting with the plasma. The emitted photons are linearly polarized either parallel to or perpendicular to the electric field. Therefore, the direction of the electric field and thus the magnetic pitch angle could be derived by measuring the photon polarizations. The  $H_{\alpha}$  line is chosen for measurements because of its high intensity and visible wavelength ( $\sim 656$  nm). To achieve an  $\sim 2$  cm spatial resolution, 10 MSE channels are needed from the magnetic axis to the outer board side of the plasma edge around the mid-plane, as shown in Figure 1-3.

A main challenge of C-Mod MSE diagnostic is the shot-by-shot drift of the measured pitch angles caused by thermal-stress induced birefringence of the in-vessel lenses [12][13]. The absolute value of the measured pitch angle is therefore usually not correct. Therefore, the relative pitch angle change during a plasma discharge is used for the current profile analysis. This relative change measurement should have a reasonable accuracy, considering the slow temperature variation for the lens during a 2 s plasma discharge [13][14].

Another disadvantage of the MSE system is its relatively slow time response. The MSE measurement is usually averaged over 100 ms to reduce the background. Therefore, it cannot follow fast evolution of the current density profiles, such as during sawtooth events.

MSE may not work on future large, high density, tokamaks, since the penetration depth for the high energy beam is insufficient to reach the plasma core.

### **Two Color Interferometer**

The two color interferometer (TCI) system [10][15] measures the line-integrated density along ten vertically viewing chords in a Michelson configuration on C-Mod. Lasers with two wavelengths ( $\text{CO}_2$  and HeNe) are co-aligned along the same beam path, to subtract the vibration error for the phase shift measurements. The locations of the ten chords are shown in Figure 1-3. The measurement resolution is typically  $\sim 5 \times 10^{18}/\text{m}^2$ . The line integrated density on channel 4 (nl04), at  $R=0.68$  m, is used for feedback control of the plasma density.

One disadvantage of the TCI system is that all ten vertical chords are close to the plasma core ( $r/a=0-0.55$ ) due to the beam-path constraints of the port window. It is not possible to invert the density profile without edge density measurements. This is one reason that we are developing a poloidally viewing polarimetry system, which has the potential to span over the whole poloidal cross-section with multiple chords, instead of choosing the vertically viewing geometry more commonly used on other experiments.

### **Thomson Scattering**

The Thomson scattering (TS) system [10] measures the local electron density and temperature by measuring the spectrum of the scattered photons from the plasma electrons. The C-Mod TS system fires two high power Yttrium Aluminum Garnet (YAG) lasers vertically near the plasma magnetic axis, as shown in Figure 1-3. Each laser is fired at a rate of 50 Hz, and therefore a time resolution of 10 ms is achieved by setting up the lasers with a 10 ms offset.

The measurement locations are mapped to the outboard mid-plane assuming the plasma density and temperature are constant on a given flux surface (because of the rapid transport along the magnetic field). The data points on the mid-plane are fit to a profile using the numerical codes Nfits [16] or Quickfit [17]. Quickfit, which fits the core and edge Thomson separately with low order polynomials and combines them smoothly with a tanh function, is used extensively in this thesis.

Since the two YAG lasers usually run at different power level with imperfect co-alignment, it is typical to see a systematic density discrepancy between the two measurements, which can be eliminated by a careful diagnostic calibration. TS can be benchmarked with TCI to estimate the systematic errors in the density measurement. The TS density is mapped onto the TCI beam-path, line integrated and compared with the TCI data. The required correction is usually less than 10% throughout the time of the discharge when the TS system is well calibrated.

### **EFIT (with magnetic coil measurements)**

The equilibrium fitting code EFIT [18][19] determines the poloidal magnetic flux surfaces on C-Mod, by solving the following Grad-Shafranov equation (defined in toroidal coordinate:  $R$ ,  $\phi$ ,  $z$ )[7].

$$\Delta^* \psi = -2\pi R \mu_0 j_\phi \quad (1.13)$$

with

$$\Delta^* \equiv R \frac{\partial}{\partial R} \left( \frac{1}{R} \frac{\partial \psi}{\partial R} \right) + \frac{\partial^2 \psi}{\partial z^2} \quad (1.14)$$

The toroidal plasma current is given by

$$j_\phi = \frac{2\pi}{\mu_0} \left( \mu_0 R \frac{dP}{d\psi} + \frac{F}{R} \frac{dF}{d\psi} \right) \quad (1.15)$$

where  $P(\psi)$  is the plasma pressure, and  $F(\psi) = RB_\phi$ . By fitting  $P(\psi)$  and  $F(\psi)$  with low order (usually 2nd or 3rd) polynomial or spline functions, EFIT minimizes the error between the reconstructed magnetic field and the external magnetic coil measurements (Figure 1-3).  $q_0$  is assumed to be 0.95 in the reconstructions, which is a good approximation for sawtooth discharges. The reconstruction results are available shortly after a shot in the MDSplus [20] tree “ANALYSIS”. Since there are no internal constraints from plasma pressure or MSE, this version of EFIT is called normal EFIT.

Since the assumption on  $q_0$  is not true during the LHCD discharges, normal EFIT normally shows larger errors on the reconstructed core magnetic fields, which will be discussed in detail in chapter 5. Kinetic-EFIT [21] has been developed to simulate the current density profile for LHCD discharges on C-Mod. In addition to the input diagnostic data for normal EFIT, Kinetic-EFIT takes the plasma pressure, and magnetic pitch angles from MSE as internal constraints to improve the reconstruction accuracy. The sawtooth inversion radius (SIR), where the safety factor  $q=1$ , is also a constraint option. As described in chapter 5, polarimetry measurements have been used to show that the Kinetic-EFIT reconstructions are more accurate than those from normal EFIT.

Normal EFIT is automatically run right after each plasma discharge, while Kinetic-EFIT needs some extra work on preparing good MSE data, such as removing bad data points and choosing a reference time-slice during the Ohmic phase to provide the baseline error offsets. Kinetic-EFIT also takes some manpower on the fitting process for manually picking the proper fixed nodes for the spline fitting of the flux function  $FF'$ . Since MSE data are averaged over several time points to reduce the background noise during LHCD, Kinetic-EFIT usually has a time resolution no better than 100 ms.

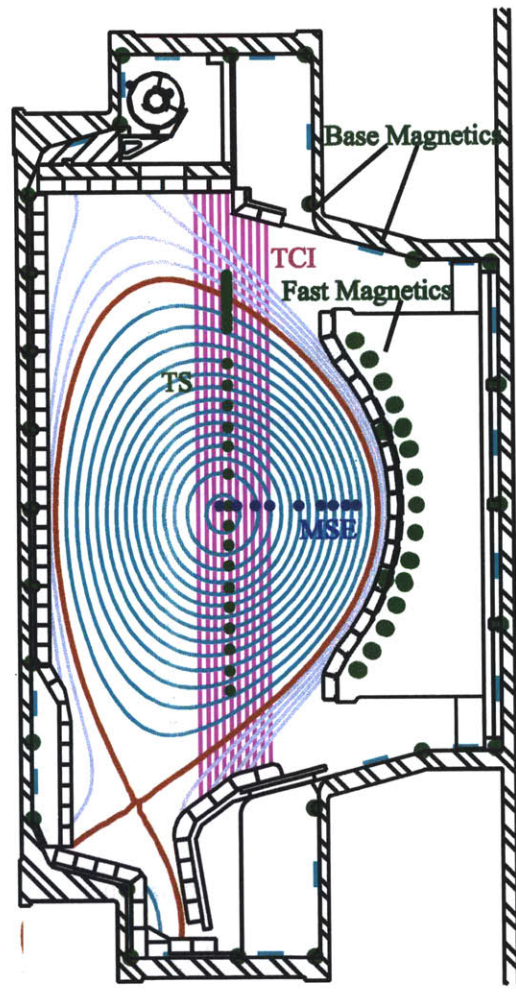


Figure 1-3: C-Mod cross section with locations of the certain measurements.

## 1.4 Lower Hybrid Current Drive

C-Mod has a toroidal plasma current, ranging from 0.3 to 2.1 MA. This current is usually driven by mutual induction between a central solenoid and the plasma itself, which is called Ohmic or inductive current drive. According to transformer theory, the swing of the central solenoid current ( $\frac{dI_{coil}}{dt}$ ) needs to be maintained to sustain the plasma current. This process can not last long, considering the limits of the maximal current and heat load in the solenoid. On C-Mod, we can run a plasma discharge up to 5 s (typically  $\sim 2$  s) long, and after that the toroidal magnetic coils needs to be cooled by liquid nitrogen before the next discharge. To achieve steady-state operation for future reactors, various non-inductive current drive methods have been intensively studied.

One technique is to drive the current with Neutral Beam Injection (NBI) [22] by injecting high energy neutral atoms into the plasma along a tangential direction. The incident neutral atoms are ionized by the hot plasma, and ultimately generate a net current in the preferred direction. Another method is to drive the current with high power radio frequency waves, such as Electron Cyclotron Current Drive (ECCD) [22][23] or LHCD [3][22]. ECCD selectively heats the electrons moving in the toroidal direction, which decreases their collision frequency and therefore increases their contribution to the toroidal current. The asymmetry of the electron distribution function in the toroidal direction from electron cyclotron heating produces a net toroidal current. LHCD drives the current by electron Landau damping, and will be briefly discussed in the following section. All of these current drive methods have their own pros and cons, and none of them could solely drive the whole plasma current for the future fusion reactors. A self-driven plasma current, bootstrap current [24], is a necessary complement for the external driven current. The bootstrap current is generated by the trapped electrons with the pressure gradients in the plasma. Optimal current drive scheme for ITER uses a combination of different current drive

methods considering the cost and reliability, and the bootstrap current is proposed to drive ~50% of the total current.

Basic theory and the LHCD system on C-Mod will be presented in this section. Details about the LH physics can be found in review paper [22].

### 1.4.1 Basic Theory

The LH wave is an electrostatic wave with a frequency between electron and ion cyclotron frequencies:  $\omega_{ci}^2 \ll \omega^2 \ll \omega_{ce}^2$ . The wave dispersion relation can be deduced with cold plasma approximation as

$$n_{\perp}^2 \approx n_{\parallel}^2 \frac{m_i}{m_e} \frac{\omega_{LH}^2}{\omega^2 - \omega_{LH}^2} \quad (1.16)$$

where  $\omega_{LH}$  is

$$\omega_{LH}^2 \approx \frac{\omega_{pi}^2}{1 + \frac{\omega_{pe}^2}{\omega_{ce}^2}} \quad (1.17)$$

$$n_{\perp} = \frac{ck_{\perp}}{\omega} \quad (1.18)$$

$$n_{\parallel} = \frac{ck_{\parallel}}{\omega} \quad (1.19)$$

$\omega_{pi} = \left(\frac{n_i z_i^2 e^2}{m_i \epsilon_0}\right)^{\frac{1}{2}}$ ,  $\omega_{pe} = \left(\frac{n_e e^2}{m_e \epsilon_0}\right)^{\frac{1}{2}}$ , and  $k_{\perp}$ ,  $k_{\parallel}$  are the LH wavenumbers perpendicular or parallel to the magnetic field. On C-Mod, the incident LH wave has a frequency of  $f = 4.6 \text{ GHz}$  ( $f_{ci} \approx 40 \text{ MHz}$  and  $f_{ce} \approx 140 \text{ GHz}$  with  $B_1 \approx 5 \text{ T}$ ), and is launched into the plasma with a phased waveguide array launcher that defines the initial value of  $n_{\parallel}$  [25]. Therefore,  $n_{\perp}$  can be estimated from local plasma parameters by Equation 1.16. Ray tracing (GENRAY) [26] and full-wave (LHEAF) codes [27] have been used to simulate the propagation of LH waves in the C-Mod plasma.

Electron Landau damping of the LH waves results in current being driven in the plasma. When the LH wave is launched with a phase velocity of 3-5 times that of the electron thermal velocity ( $v_{te} = \sqrt{2T_e/m_e}$ ) parallel to the magnetic field, electrons slightly faster than the wave will be decelerated, and electrons with slightly lower velocity will be accelerated by the wave. With a Maxwellian velocity distribution function, more electrons are accelerated than damped, and a plateau is created in the velocity distribution function (Figure 1-4). The asymmetry of the velocity distribution function results in a driven current, given by

$$J_{\parallel} = -e \int_{-\infty}^{+\infty} v_{\parallel} f(v_{\parallel}) dv_{\parallel} \quad (1.20)$$

where  $J_{\parallel}$  is the driven current density parallel to the magnetic field, and  $v_{\parallel}$  is the electron parallel velocity. A Fokker-Plank code, CQL3D [28], has been widely used on C-Mod to simulate the LH wave power deposition and the driven current profile.

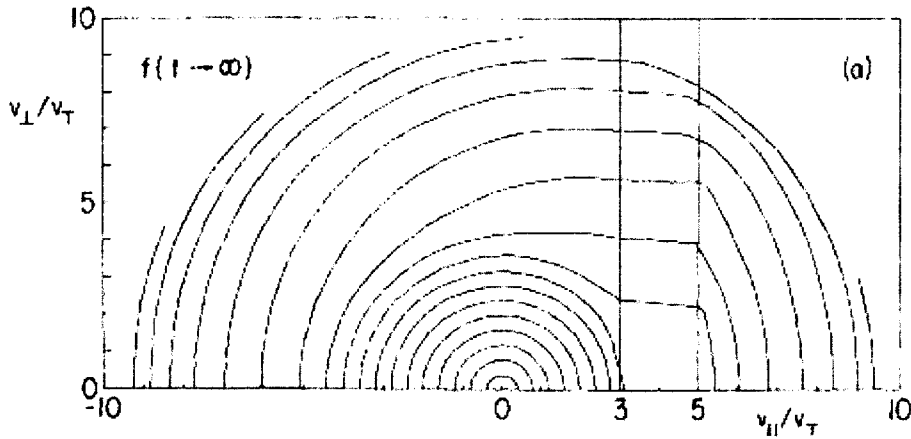


**Figure 1-4: Contours of the electron velocity distribution function, when the parallel LH phase velocity is ~3-5 times of the electron thermal velocity ( $v_T$ ) (Figure from [22])**

To determine the cost effectiveness of the LH system, it is crucial to evaluate current drive efficiency and its relation to the plasma and LH wave parameters. The LHCD efficiency is defined as the ratio of the driven current to the dissipated power.

$$\eta_{LH} = \frac{J_{\parallel}}{P_d} \quad (1.21)$$

It can be estimated with a single particle model [25][29], which shows that low density and lower  $n_{\parallel}$  are preferred for high current driven efficiency

$$\eta_{LH} \propto \frac{1}{n_e n_{\parallel}^2} \quad (1.22)$$

#### 1.4.2 C-Mod LH System

The LH system on C-Mod has a source power of up to 3 MW, generated by 12 klystrons. These tubes produce 250 kW each of microwave power at 4.6 GHz. The power is coupled into the plasma through a launcher, which for historical reasons is referred to as LH2.

Through a series of protection and feedback control components [25][29], the LH power from the klystrons is divided and transmitted to LH2 with 64 separated waveguides (16 columns X 4 rows, Figure 1-5). The central 4 columns are each powered by a single klystron, while the other 12 columns are divided into 6 pairs, powered by 6 klystrons respectively. A photograph of the launcher in the C-Mod vacuum vessel is shown in Figure 1-6. Molybdenum limiters on both sides of the launcher provide protection from the plasma.

The  $n_{\parallel}$  of the launched LH wave is determined by the phase difference between the columns of the waveguides, which is normally tuned by the phase of the klystrons. However, for any two adjacent columns sharing one klystron, a mechanically controlled “phase shim” whose length can be adjusted is installed on one column to set the desired relative phase.

The LH2 system was regularly operated at 800 kW net power for 0.75 s during the plasma flat top. It can be remotely controlled to do an  $n_{\parallel}$  scan, from 2.4 to 1.6 (phasing from 115°

to 75°), while maintaining high LH power. Consistent high quality LH pulses have contributed to the success of the LHCD experiments presented in chapter 5.

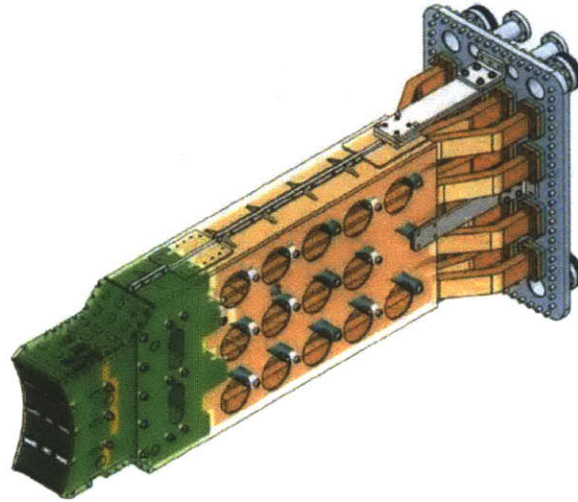


**Figure 1-5: Model drawing of the LH2 launcher**

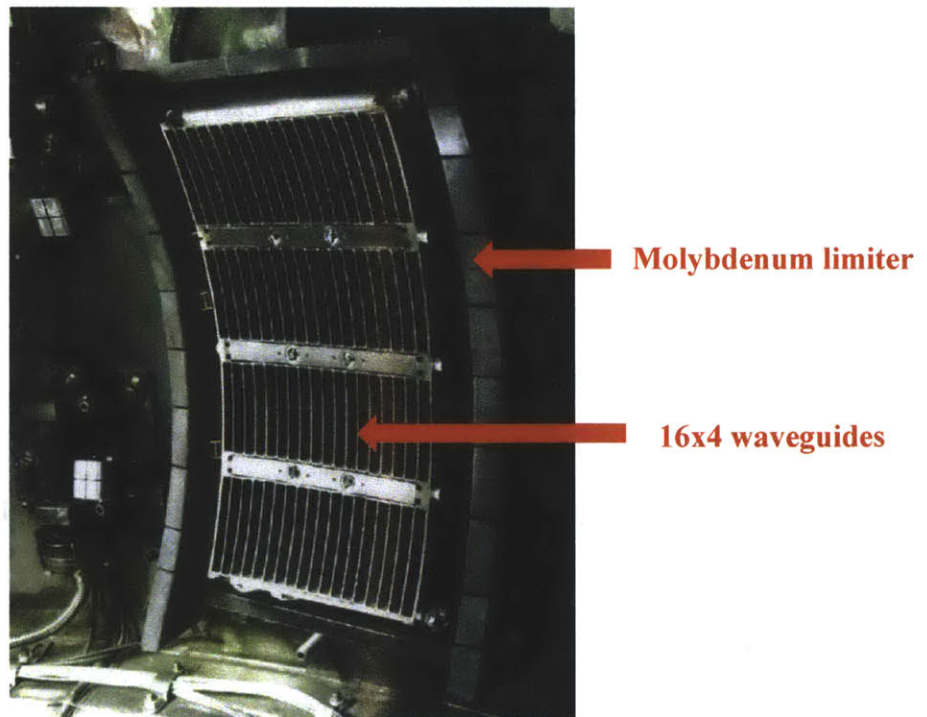


**Figure 1-6: In vessel view of the installed LH2 launcher**

## 1.5 Motivations for Polarimetry Studies

Although the total plasma current in a tokamak can be easily measured with an external Rogowski coil, it is much more difficult to measure the current density profile inside the plasma. On C-Mod, the current density profile is based on EFIT reconstructions using the external magnetic coil measurements, which may have a large uncertainty in the plasma core due to insufficient internal magnetic field information. A new multi-chord polarimetry diagnostic which measures the line integrals of the internal poloidal magnetic fields (weighted by the electron density) and therefore the toroidal current profile has been developed on C-Mod with the following motivations.

- Accurate current density profile measurement is crucial for LH physics research.
- The polarimeter works as a benchmark for the MSE diagnostic, which suffers from thermal drift problems. It also complements the MSE system with much higher time resolution, off mid-plane measurements and the capability of measurements during high density plasma operation, when the DNB has difficulty penetrating beyond the edge plasma.
- Controlling the shape of the current density profile is a key element to enhance the plasma performance. Potential real-time control of the current density profile with the polarimeter is critical to reach a steady-state high performance regime of operation in a tokamak.
- The polarimeter uses a similar laser wavelength and poloidal-viewing geometry as those proposed for the ITER polarimeter. Our development experience has already contributed to improvements in experiments on J-TEXT [30], EAST and DIII-D [31], and will significantly contribute to the future diagnostic development on ITER.
- The polarimetry system has a 2 MHz bandwidth, which allows measurements of high frequency magnetic and density fluctuations. It is the only diagnostic thus far to measure

the core magnetic fluctuations on C-Mod. These fluctuation measurements will enhance our understanding of turbulence and transport.

## 1.6 Thesis Outline

We have developed a 3-chord poloidal viewing polarimeter on C-Mod, which senses current density profile changes during LHCD experiments, and diagnoses a wide frequency band for both density and magnetic fluctuations.

Chapter 2 briefly introduces the polarimetry theory and reviews various measurement techniques previously developed to improve the diagnostic accuracy.

In chapter 3, we will present the development of the 3-chord polarimeter, including designing the beam-path geometry and improving the optical components. Digital and analog phase analysis techniques for detector signals are compared.

The processes to reduce the noise and calibrate the polarimetry errors are presented in chapter 4. Polarimetry sensitivity to plasma density, current and position changes are evaluated. A sufficiently low noise level allows sawtooth crashes to be regularly observed on all three polarimetry chords.

Chapter 5 presents the polarimetry observations during LHCD experiments. We scan the LH power, timing, and phasing, and plasma density and current, and infer the current drive efficiency through polarimetry measurements. We also validate the Kinetic-EFIT results through comparisons of polarimetry measurements with synthetic signals. Finally, polarimetry data are incorporated into normal EFIT to constrain the central safety factor,  $q_0$ .

Chapter 6 introduces fluctuations as measured by the polarimeter. Broadband fluctuations during the EDA H-mode are observed by polarimeter, and are found to be significantly suppressed with high power LH waves. The polarimeter also confirms the poloidal asymmetry of the weakly coherent mode (WCM) in I-Mode.

Finally, we will summarize the experimental results and discuss the possible future polarimetry upgrades in Chapter 7.



## 2. Basic Polarimetry Theory

Diagnosing the internal magnetic field in fusion machines with polarimetry was first proposed by De Marco and Segre in 1972 [32]. The Faraday rotation of a linearly polarized probing beam propagating through the magnetized plasma contains the magnetic field information parallel to the probing beam propagation direction. Since then, polarimetry diagnostics have been developed with various improvements, including different probing beam modulation and phase detecting techniques, different optical path geometries, and different parameter measurements (magnetic field and/or plasma density, equilibrium and/or fluctuations) [33][34][35][36][37][31]. To design a polarimeter according to the specific geometry and plasma parameters of C-Mod, we need to understand basic polarimetry theory, and to be familiar with the pros and cons of the previous polarimetry systems on other experiments around the world.

In section 2.1, we will introduce the basic theory of the interferometry/polarimetry measurements in magnetized plasma.

Section 2.2 reviews previously successful polarimetry measurement techniques, and discusses the pros and cons for each method. Different optical viewing geometries for the polarimetry systems are also discussed.

Since the polarimeter measurement is the line integral along the beam path, it is not straightforward to deduce the local magnetic field or the current density profile, even from multi-chord measurements. Section 2.3 presents the methods to infer the current density profile from multi-chord polarimetry data.

## 2.1 Basic Polarimetry Theory

A polarimeter is a diagnostic based on a plasma refractive-index measurement, similar to an interferometer. When a probing laser beam propagates through the plasma, it has a different phase shift compared to free space propagation. The phase shift is proportional to the plasma density, and can be measured by an interferometer. In highly anisotropic magnetized plasma, the polarization of the probing beam can be rotated: an effect called Faraday rotation. The Faraday rotation depends on both the plasma density and internal magnetic field. To understand how these refractive-index based diagnostics work, especially for the polarimeter, we start from the plasma dispersion relations.

### 2.1.1 Dispersion Relations

The propagation of the electromagnetic waves in plasma follows Maxwell's equations:

$$\nabla \times \vec{E} = -\frac{\partial \vec{B}}{\partial t} \quad (2.1)$$

$$\nabla \times \vec{B} = \frac{1}{c^2} \frac{\partial \vec{E}}{\partial t} + \mu_0 \vec{J} \quad (2.2)$$

The plasma current is a function of the electric field, according to Ohm's Law

$$\vec{J} = \vec{\sigma} \cdot \vec{E} \quad (2.3)$$

where  $\vec{\sigma}$  is the plasma conductivity tensor. By eliminating  $\vec{B}$  and  $\vec{J}$ , Equations 2.1-2.3 are combined into

$$\nabla \times (\nabla \times \vec{E}) + \frac{1}{c^2} \frac{\partial^2 \vec{E}}{\partial t^2} + \mu_0 \frac{\partial (\vec{\sigma} \cdot \vec{E})}{\partial t} = 0 \quad (2.4)$$

With the plane-wave assumption (short wavelength compared to gradient scale lengths),  $\vec{E} = \vec{E}_0 e^{i(\vec{k} \cdot \vec{x} - \omega t)}$ , we can apply a Fourier technique to Equation 2.4 by relating  $\nabla$  to  $i\vec{k}$  and  $\frac{\partial}{\partial t}$  to  $-i\omega$ .

Equation 2.4 becomes

$$\vec{k} \times (\vec{k} \times \vec{E}) + \frac{\omega^2}{c^2} \vec{E} + i\mu_0 \omega \vec{\sigma} \cdot \vec{E} = 0 \quad (2.5)$$

or

$$\left[ \vec{k}\vec{k} - k^2 \vec{I} + \frac{\omega^2}{c^2} \left( \vec{I} + \frac{i}{\omega \epsilon_0} \vec{\sigma} \right) \right] \cdot \vec{E} = 0 \quad (2.6)$$

To make sure there is a non-trivial solution, the determinant of the coefficient matrix has to be zero. Thus, we find the dispersion relation from

$$\det \left[ \vec{k}\vec{k} - k^2 \vec{I} + \frac{\omega^2}{c^2} \vec{\epsilon} \right] = 0 \quad (2.7)$$

where  $\vec{\epsilon} = \vec{I} + \frac{i}{\omega \epsilon_0} \vec{\sigma}$  is the dielectric tensor. The refractive index is defined as  $\vec{N} = \frac{c}{\omega} \vec{k}$ ,

$$\det[\vec{N}\vec{N} - N^2 \vec{I} + \vec{\epsilon}] = 0 \quad (2.8)$$

The thermal motions of the charged particles are neglected (cold plasma approximation), and the particles are driven by the electrical field

$$\vec{J} = \vec{\sigma} \cdot \vec{E} = \sum_i n_i q_i \vec{v}_i \quad (2.9)$$

where  $i$  represents different species of charged particles. Since the velocity of the electrons is much higher than that of the ions, the electrons are usually the dominant contributors to the plasma current

$$\vec{J} \approx -n_e e \vec{v}_e \quad (2.10)$$

To solve for the electron velocities, we use the momentum equation for a single electron,

$$-e(\vec{E} + \vec{v} \times \vec{B}) = m_e \frac{\partial \vec{v}}{\partial t} \quad (2.11)$$

which can be simplified by substituting  $-i\omega$  for  $\frac{\partial}{\partial t}$

$$-e(\vec{E} + \vec{v} \times \vec{B}) = -i\omega m_e \vec{v} \quad (2.12)$$

Equation 2.12 can be transformed to three scalar equations in the following coordinate system: The z-axis is the wave vector direction, and magnetic field and wave vector (with relative angle  $\theta$ ) define the y-z plane, as shown in Figure 2-1.

$$v_x = \frac{-ie}{\omega m_e} (E_x + v_y B \cos \theta - v_z B \sin \theta) \quad (2.13)$$

$$v_y = \frac{-ie}{\omega m_e} (E_y - v_x B \cos \theta) \quad (2.14)$$

$$v_z = \frac{-ie}{\omega m_e} (E_z - v_x B \sin \theta) \quad (2.15)$$

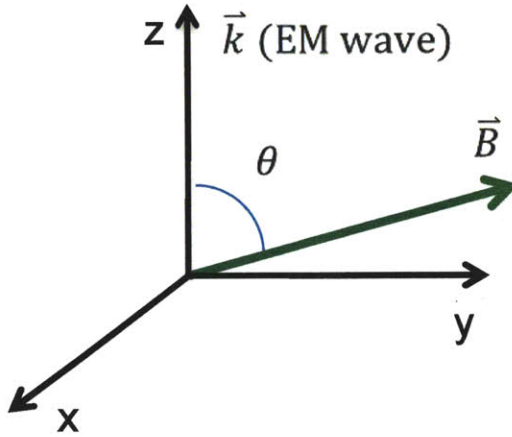


Figure 2-1: Coordinate system

The three velocity components are then solved as

$$v_x = A(E_x - iY \cos \theta E_y + iY \sin \theta E_z) \quad (2.16)$$

$$v_y = A[iY \cos \theta E_x + (1 - Y^2 \sin^2 \theta)E_y + (-Y^2 \sin \theta \cos \theta)E_z] \quad (2.17)$$

$$v_z = A[-iY \sin \theta E_x + (-Y^2 \sin \theta \cos \theta)E_y + (1 - Y^2 \cos^2 \theta)E_z] \quad (2.18)$$

where  $Y = \frac{eB}{m_e \omega} = \frac{\omega_{ce}}{\omega} \ll 1$ , and  $A = \frac{-ie}{m_e \omega (1 - Y^2)}$ . Substituting the velocities into Equation 2.9,

the dielectric tensor becomes

$$\vec{\epsilon} = \begin{bmatrix} 1 - \frac{X}{1-Y^2} & \frac{iXY \cos \theta}{1-Y^2} & -\frac{iXY \sin \theta}{1-Y^2} \\ -\frac{iXY \cos \theta}{1-Y^2} & 1 - \frac{X(1-Y^2 \sin^2 \theta)}{1-Y^2} & \frac{XY^2 \cos \theta \sin \theta}{1-Y^2} \\ \frac{iXY \sin \theta}{1-Y^2} & \frac{XY^2 \cos \theta \sin \theta}{1-Y^2} & 1 - \frac{X(1-Y^2 \cos^2 \theta)}{1-Y^2} \end{bmatrix} \quad (2.19)$$

where  $X = \frac{n_e e^2}{m_e \epsilon_0 \omega^2} = \frac{\omega_{pe}^2}{\omega^2} \ll 1$ . Since the wave vector  $\vec{k}$  (also  $\vec{N}$ ) is along the z-axis, Equation 2.7

becomes

$$\begin{vmatrix} 1 - N^2 - \frac{X}{1-Y^2} & \frac{iXY \cos \theta}{1-Y^2} & -\frac{iXY \sin \theta}{1-Y^2} \\ -\frac{iXY \cos \theta}{1-Y^2} & 1 - N^2 - \frac{X(1-Y^2 \sin^2 \theta)}{1-Y^2} & \frac{XY^2 \cos \theta \sin \theta}{1-Y^2} \\ \frac{iXY \sin \theta}{1-Y^2} & \frac{XY^2 \cos \theta \sin \theta}{1-Y^2} & 1 - \frac{X(1-Y^2 \cos^2 \theta)}{1-Y^2} \end{vmatrix} = 0 \quad (2.20)$$

The solution for the refractive index is the Appleton-Hartree formula [38],

$$N^2 = 1 - \frac{X(1-X)}{1-X - \frac{1}{2}Y^2 \sin^2 \theta \pm \sqrt{\left(\frac{1}{2}Y^2 \sin^2 \theta\right)^2 + (1-X)^2 Y^2 \cos^2 \theta}} \quad (2.21)$$

where  $\pm$  correspond to different characteristic polarizations. The related transverse characteristic polarizations are

$$\frac{E_x}{E_y} = -\frac{iY \sin^2 \theta}{2(1-X) \cos \theta} \pm i \left[ 1 + \frac{Y^2 \sin^4 \theta}{4(1-X)^2 \cos^2 \theta} \right]^{\frac{1}{2}} \quad (2.22)$$

### 2.1.2 Limiting Cases

(1) If we neglect the birefringence of the plasma (assume  $Y=0$ ), the plasma refractive index simplifies to

$$N^2 = 1 - X \quad (2.23)$$

$$N = (1 - X)^{\frac{1}{2}} \approx 1 - \frac{X}{2} \quad (2.24)$$

The phase difference measured by interferometry comes from the different refractive index between vacuum and plasma,

$$\phi = \int \frac{\omega}{c} (N - 1) dl \approx \frac{\omega}{2c} \int X dl = \frac{e^2 \lambda}{4\pi \epsilon_0 c^2 m_e} \int n_e dl \quad (2.25)$$

Therefore, the interferometer measures the line-integral of the electron density along the laser beam-path, and the phase shift, for a given density, is proportional to the laser wavelength.

(2) In a strong magnetic field, we have to take plasma birefringence into consideration, and the plasma refractive indices depend on  $\theta$ . When the magnetic field is parallel to the wave vector ( $\theta = 0^\circ$ )

$$N^2 = 1 - \frac{X}{1 \pm Y} \approx 1 - X(1 \mp Y) \quad (2.26)$$

$$N_{\pm} \approx 1 - \frac{X(1 \mp Y)}{2} \quad (2.27)$$

The characteristic polarizations are counter-rotating circularly-polarized beams

$$\frac{E_x}{E_y} = \pm i \quad (2.28)$$

The Faraday rotation effect is caused by the phase difference between these two characteristic waves. Assuming a linearly polarized beam aligned with the x-axis, it can be decomposed into two circularly polarized beams  $\vec{E}_0 = E_0 \hat{x} = \vec{E}_+ + \vec{E}_-$

$$\text{where } \vec{E}_{\pm} = \frac{E_0}{2} (\hat{x} \mp i\hat{y}) e^{-i\omega t}$$

After propagation a small distance  $z$  in the plasma,

$$\begin{aligned} \vec{E}_z &= \vec{E}_+ e^{ik_+z} + \vec{E}_- e^{ik_-z} \\ &= \frac{E_0}{2} e^{i\left(\frac{k_+ + k_-}{2}z - \omega t\right)} \left[ \left( e^{i\frac{k_+ - k_-}{2}z} + e^{-i\frac{k_+ - k_-}{2}z} \right) \hat{x} - i \left( e^{i\frac{k_+ - k_-}{2}z} - e^{-i\frac{k_+ - k_-}{2}z} \right) \hat{y} \right] \\ &= E_0 e^{i\left(\frac{k_+ + k_-}{2}z - \omega t\right)} (\cos \alpha \hat{x} + \sin \alpha \hat{y}) \end{aligned} \quad (2.29)$$

where  $\alpha = \frac{k_+ - k_-}{2}$ ,  $z = \frac{\omega z}{2c}(N_+ - N_-)$ . The laser beam not only experiences a phase shift of  $\frac{k_+ + k_-}{2}z$  (interferometry effect), but also has a Faraday rotation through angle  $\alpha$ . According to the

WKBJ approximation [38], the total Faraday rotation through the plasma is

$$\alpha = \int \frac{\omega}{2c}(N_+ - N_-)dl = \frac{\omega}{2c} \int XYdl = \frac{e^3 \lambda^2}{8\pi^2 \epsilon_0 c^3 m_e^2} \int n_e B_{\parallel} dl \quad (2.30)$$

Therefore, the polarimeter measures the line-integral of the electron density and the magnetic field along the laser beam-path, and the rotation angle is proportional to  $\lambda^2$ . It is about two orders of magnitude smaller than the interferometry phase shift with the FIR wavelength and C-Mod magnetic fields.

(3) When the magnetic field is perpendicular to the wave vector ( $\theta = 90^\circ$ ),

$$N^2 = 1 - X \text{ or } 1 - \frac{X(1 - X)}{1 - X - Y^2} \quad (2.31)$$

$$N_o \approx 1 - \frac{X}{2} \quad (2.32)$$

$$N_x \approx 1 - \frac{X(1 - X)}{2(1 - X - Y^2)} \quad (2.33)$$

Since  $N_o$  is the same as the refractive index without magnetic field (Equation 2.24), it is named the ordinary-mode (O-mode). For the O-mode, the characteristic polarization is a linear polarization along the y-axis ( $E_x = E_z = 0$ ). The other mode is the extraordinary-mode (X-mode).

The characteristic polarization for X-mode is

$$\frac{E_x}{E_z} = \frac{1 - X - Y^2}{iXY} \quad (2.34)$$

If the incident linearly polarized beam only has an x or y component, it will only see either X-mode or O-mode, and will sustain the linear polarization. When the incident beam polarization is  $45^\circ$  relative to the magnetic field,  $\vec{E}_0 = \frac{E_0}{\sqrt{2}}(\hat{x} + \hat{y})e^{-i\omega t}$ , the  $\hat{x}$  and  $\hat{y}$  components

experience different indices of refraction, and thus have different phase after going through a thin slab of magnetized plasma with thickness  $z$ .

$$\vec{E}_0 = \frac{E_0}{\sqrt{2}}(e^{ik_x z} \hat{x} + e^{ik_o z} \hat{y})e^{-i\omega t} = \frac{E_0}{\sqrt{2}}(e^{i(k_x - k_o)z} \hat{x} + \hat{y})e^{i(k_o z - \omega t)} \quad (2.35)$$

Therefore, the linearly polarized beam turns into an elliptically polarized beam. The phase difference between the  $\hat{x}$  and  $\hat{y}$  components is called the Cotton-Mouton (C-M) effect,  $\varphi_{CM}$ , which is calculated by

$$\varphi_{CM} = (k_x - k_o)z = \frac{\omega z}{c}(N_x - N_o) \quad (2.36)$$

According to the WKBJ approximation, the total C-M effect of the beam propagation through the plasma is

$$\varphi_{CM} = \int \frac{\omega}{c}(N_x - N_o) dl \approx \frac{\omega}{c} \int \frac{XY^2}{2} dl \approx \frac{e^4 \lambda^3}{16\pi^3 \epsilon_o c^4 m_e^3} \int n_e B_{\perp}^2 dl \quad (2.37)$$

Thus, the C-M effect is proportional to  $\lambda^3$ , the line-integral of the electron density and the square of the perpendicular magnetic field.

### 2.1.3 Normal Case

We have deduced the Faraday rotation and C-M effects separately in limiting cases, when the magnetic field is either parallel or perpendicular to the laser propagation direction. However, the angle between  $\vec{k}$  and  $\vec{B}$  is usually neither  $0^\circ$  or  $90^\circ$  in our plasma, and the Faraday rotation and C-M effects are mixed together. It is nontrivial to extract either effect accurately, unless one of them is much smaller than the other, and thus can be neglected.

When  $\frac{Y}{\cos \theta} \ll 1$ , we have

$$N_{\pm} \approx 1 - \frac{X(1 \mp Y \cos \theta)}{2} \quad (2.38)$$

$$\frac{E_x}{E_y} \approx \pm i \quad (2.39)$$

which is close to the limiting case (2) with two circularly-polarized characteristic polarizations, and the incident beam has a Faraday rotation

$$\alpha \approx \frac{e^3 \lambda^2}{8\pi^2 \epsilon_0 c^3 m_e^2} \int n_e B \cos \theta \, dl \quad (2.40)$$

Similarly, when  $\frac{Y}{\cos \theta} \gg 1$ , the two characteristic polarizations are O-mode and X-mode, with respective refractive indices

$$N_o \approx 1 - \frac{X}{2} \quad (2.41)$$

$$N_x \approx 1 - \frac{X(1-X)}{2(1-X-Y^2 \sin^2 \theta)} \quad (2.42)$$

In this case, the C-M effect is given by

$$\varphi_{CM} \approx \frac{e^4 \lambda^3}{16\pi^3 \epsilon_0 c^4 m_e^3} \int n_e B^2 \sin^2 \theta \, dl \quad (2.43)$$

On C-Mod, the polarimetry wavelength is  $\lambda = 117.73 \, \mu m$  (chapter 3), and the toroidal magnetic field is  $\sim 5.4$  T, so that  $Y = \frac{\omega_{ce}}{\omega} = \frac{eB\lambda}{2\pi m_e c} \approx 0.06$ . Since the poloidal magnetic field along the polarimetry beam-path depends on total plasma current and the location of the polarimetry chords, it changes with the plasma conditions and measurement locations. It is estimated to be 0.2 to 0.6 T, and  $\cos \theta \approx 0.04$  to 0.1. Thus,  $\frac{Y}{\cos \theta} \approx 0.6$  to 1.5, where none of the previous approximations hold. Segre has utilized the Poincare sphere and Stokes parameters to deal with the case where the Faraday rotation and C-M effects are mixed with each other and the two effects are comparable [39][40]. It was shown that when both effects are small ( $\alpha^2 + \varphi^2 \ll 1$ ), either Faraday rotation or the C-M effect can be obtained directly with the approximation equations we have deduced. For the C-Mod polarimetry data we will present in the following chapters, especially for the LHCD discharges,  $\alpha^2 + \varphi^2 \ll 1$  is well satisfied, and therefore we can freely use the approximation equations we deduced for analysis.

## 2.2 Review of Polarimetry Techniques

Polarimetry/interferometry systems have been built on many machines [33][34][41][42][43][44][45]. To achieve high spatial and temporal resolution, some of the polarimetry systems were successfully upgraded to more than 10 chords with a time resolution up to  $\sim 1\mu\text{s}$  [45]. To enhance the measurement accuracy and reduce the systematic errors, new detecting and probing beam modulation techniques have been developed. Poloidally viewing systems have replaced the previously more typical vertically viewing geometry, in order to span the whole plasma poloidal cross section. Tangentially viewing polarimeters have been used to measure the plasma density as an alternative to the interferometer. In this section, we will go through these polarimetry systems, by mainly covering different beam modulation methods and different optical geometries.

### 2.2.1 Different Beam Modulation Methods

#### (a) Linear polarization beam measurement technique

The traditional and most straightforward method to measure the Faraday rotation is to launch a linearly polarized beam, and measure how much the polarization plane rotates in the plasma. The first successful multi-chord interferometer/polarimeter system was built with this measurement scheme by Soltwisch on TEXTOR [33]. The system had a nine-chord simultaneous measurement of both the phase shift and rotation, with  $0.15^\circ$  accuracy and 3 ms time resolution for the polarimeter.

To discuss the measurement technique, only a single chord optical system is shown in Figure 2-2. A linearly polarized beam with a wavelength of  $337\ \mu\text{m}$  is split into two beams by a beam splitter. The probing beam goes through the plasma, and experiences both the interferometry phase shift and Faraday rotation. The reference beam is given a frequency shift  $\Delta\omega$  by a rotating grating, allowing a heterodyne measurement to be made. These two beams are recombined with a beam combiner after the plasma, and form beat signals on detectors  $D_1$  and  $D_p$ .

Neglecting beam ellipticity induced by the plasma or optical system, the signals on the two detectors are approximately

$$S_{I,P} = C_{I,P} + A_{I,P} \sin(\Delta\omega t + \Delta\phi + \phi_{I,P}) \quad (2.44)$$

where  $\Delta\phi$  is the interferometry phase shift. The detector signal amplitudes are

$$A_I = [(1 - \psi_p)I_p I_r]^{\frac{1}{2}} \quad (2.45)$$

$$A_P = [\psi_p^2 I_p I_r]^{\frac{1}{2}} \quad (2.46)$$

where  $\psi_p$  is the Faraday rotation angle, and  $I_p$  ( $I_r$ ) is the power of the probe (reference) beam.

By comparing  $S_I$  with the signal from another beam, which does not go through the plasma but with the same path length, we can extract  $\Delta\phi$ . While  $\psi_p$  can be directly extracted from  $A_P$ , it usually suffers from large systematic errors, since  $I_p$  and  $I_r$  vary due to laser power changes or beam refraction in the plasma. The amplitude effect can be eliminated by calculating  $\psi_p$  from  $A_I/A_P$ , if the two detectors are calibrated to the same response.

This method worked well on TEXOR by using pyro-electro detectors, which have large apertures relative to the beam size and are not sensitive to the beam offsets from plasma refraction. As will be discussed in chapter 3, the pyro-electric detector has low sensitivity at high frequency and has been replaced with Schottky diode mixers in the newly developed polarimetry systems. One disadvantage of the Schottky diode mixer is that it is extremely sensitive to the beam coupling, thus the signal amplitude may drop significantly with strong beam refraction in the plasma. This effect cannot be easily calibrated out, because it is different on each detector, largely depending on the detector alignment.

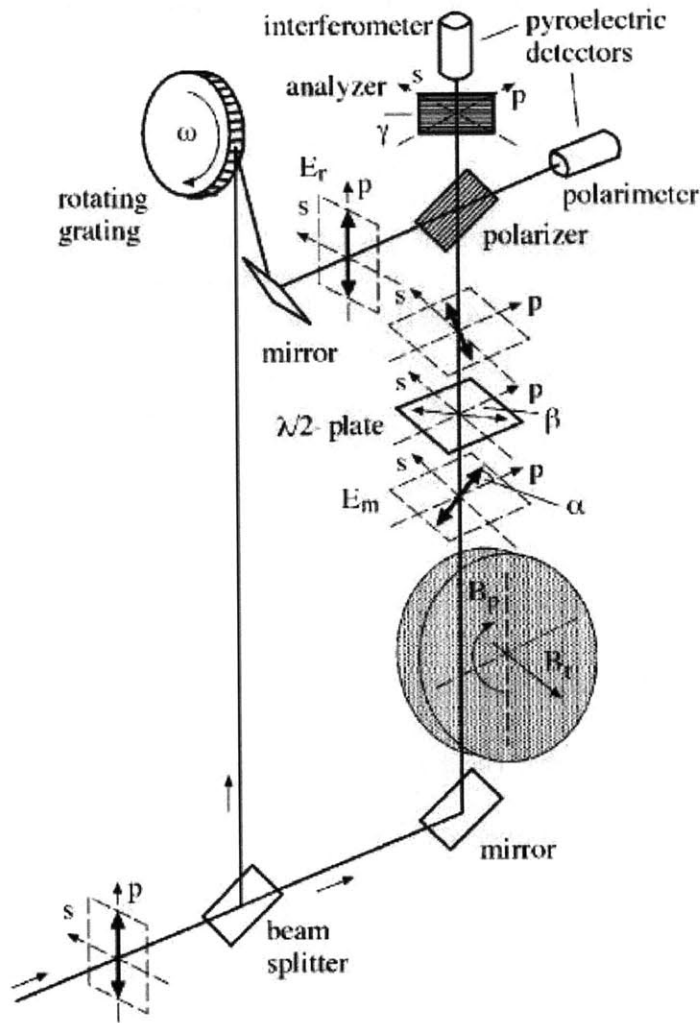


Figure 2-2: Schematic drawing of the polarimetry/interferometry system on TEXTOR with the linearly polarized beam measurement technique (Figure from [33])

**(b) Rotating elliptically polarized beam measurement technique**

With large measurement errors for the amplitude measurement technique at high bandwidth, more accurate phase measurement techniques have been developed to measure the Faraday rotation. These methods typically require modulating the incident beams instead of using a linearly polarized beam.

A rotating elliptically polarized beam scheme was developed on MTX [34], shown schematically in Figure 2-3. A linearly polarized probe beam is converted to a rotating elliptically

polarized beam with a quarter-wave plate followed by a half-wave plate which rotates at  $\sim 1$  kHz. The reference beam comes from a second laser with a frequency offset of  $\Delta\omega=1$  MHz, and is combined with the probe beam on both the reference and plasma mixers. The detected signals have two beat frequencies, with a fast beat at 1 MHz which carries the interferometry phase, and the envelop at a few kHz carrying the Faraday rotation phase (shown in Figure 2-4). By demodulation and filtering, both the interferometry and polarimetry phases can be deduced by comparing the signals between a probe detector and a reference detector. An accuracy of  $0.2^\circ$  has been achieved using this technique.

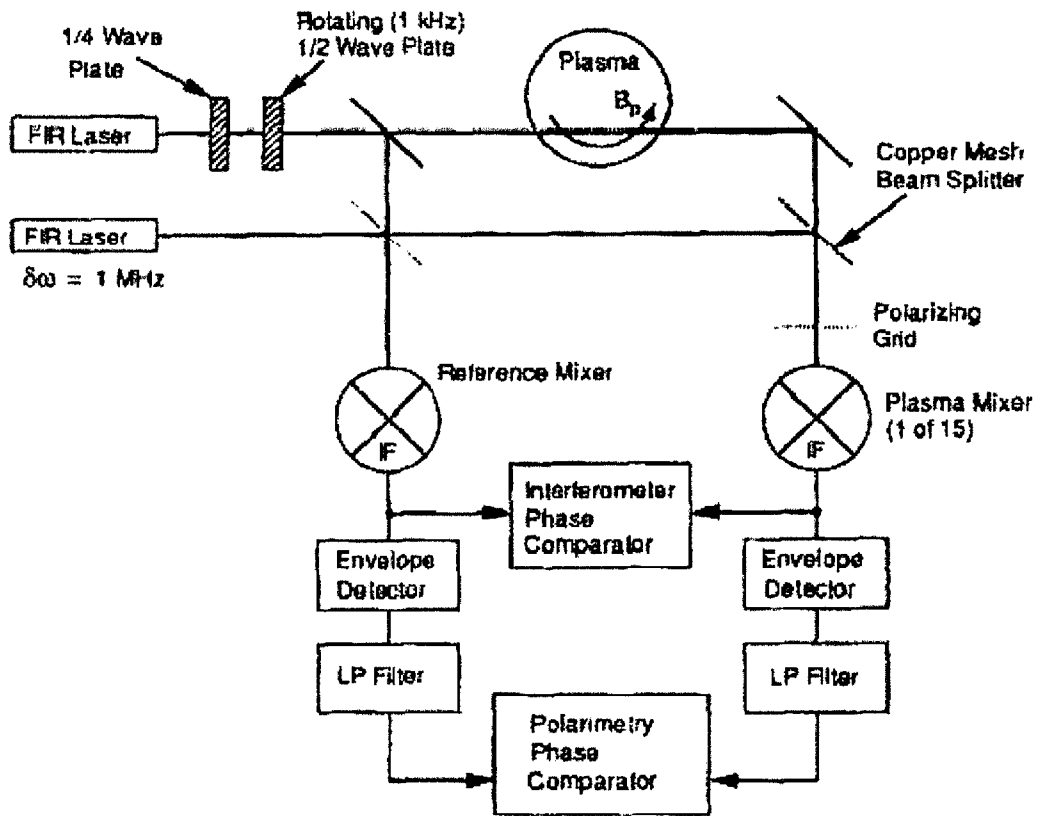


Figure 2-3: Schematic drawing of the Polarimetry/Interferometry system on MTX with a rotating elliptically polarized beam measurement technique (Figure from [34]).

Since this is a phase measurement technique, changes of the signal amplitude due to plasma refraction are not a big concern. Another advantage is that it only requires one detector for each chord. With fewer detectors, this method not only reduces cost per channel, but also saves space that can be used to accommodate more polarimetry chords in a compact system design.

The main disadvantage for this method is that the time resolution for the Faraday rotation measurement is restricted by the rotating frequency of the half-wave plate, which is limited to a few kHz. The time resolution is sufficient for current density profile analysis, but restricts the application in fluctuation measurements.

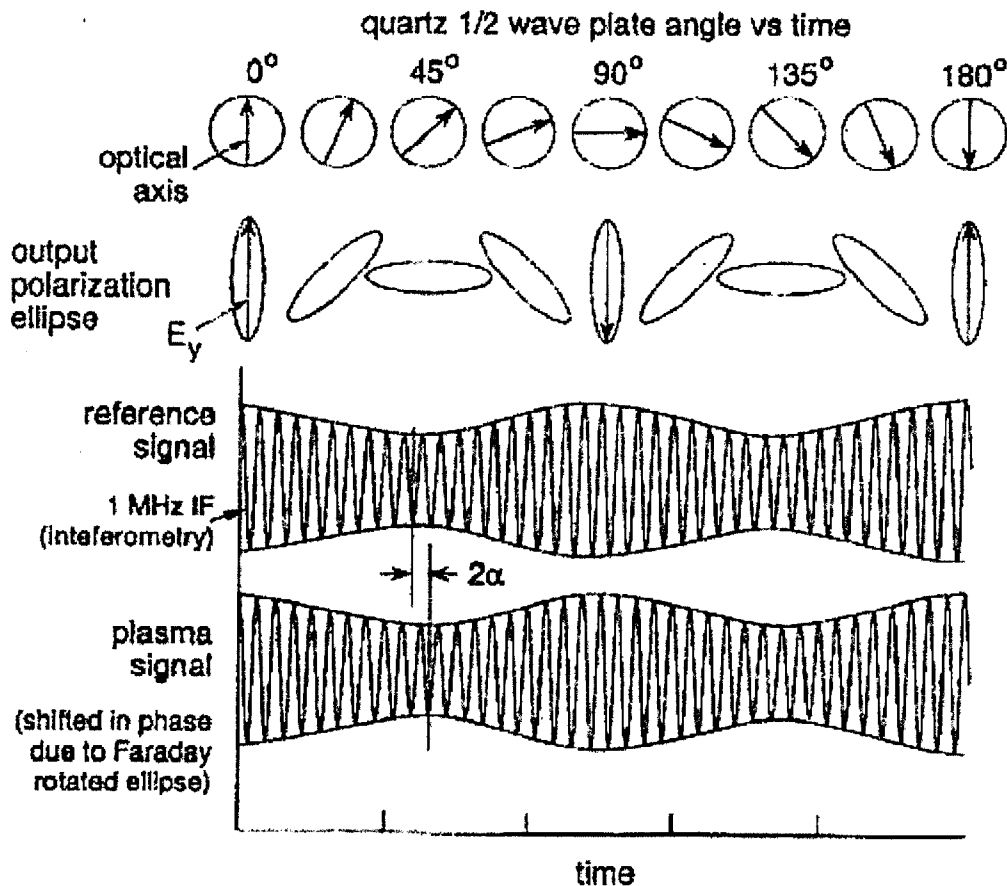


Figure 2-4: Simulated time history of the polarimetry waveforms. The phase of the 1MHz IF contains the interferometry information. The phase difference between the envelopes of the reference detector and the probing detector is twice the Faraday rotation  $\alpha$  (Figure from [46])

**(c) Counter-rotating circularly-polarized beam measurement technique**

Another phase measure technique is called the Dodel-Kunz method [35], which modulates two perpendicular linearly polarized laser beams into two counter-rotating circularly polarized beams. This method has been successfully implemented on RTP [47] and MST [45], and was also adopted for the C-Mod polarimeter.

Two orthogonal linearly polarized probe beams with a frequency offset  $\Delta\omega \ll \omega$  are transformed by a  $\frac{1}{4}$  wave-plate into L- and R- circularly polarized beams with amplitude  $a$  and  $b$ , respectively .

$$\vec{E}_L = a[\cos(\omega t) \hat{x} + \sin(\omega t) \hat{y}] \quad (2.47)$$

$$\vec{E}_R = b[\cos((\omega + \Delta\omega)t) \hat{x} - \sin((\omega + \Delta\omega)t) \hat{y}] \quad (2.48)$$

If we measure the  $\hat{x}$  component of the superposition of these two beams with a square law detector as a reference,

$$\begin{aligned} P_{ref} &= [a \cos(\omega t) + b \cos((\omega + \Delta\omega)t)]^2 \\ &= \frac{a^2[\cos(2\omega t) + 1] + b^2[\cos(2\omega t + 2\Delta\omega t) + 1]}{2} \\ &\quad + ab \cos(2\omega t + \Delta\omega t) \cos(\Delta\omega t) \end{aligned} \quad (2.49)$$

By picking out the low frequency component  $\Delta\omega$  with a band pass filter, we find

$$P_{ref} = ab \cos(\Delta\omega t) \quad (2.50)$$

After going through a slab of plasma with thickness  $z$

$$\vec{E}'_L = a'[\cos(\omega t - k_-z) \hat{x} + \sin(\omega t - k_-z) \hat{y}] \quad (2.51)$$

$$\vec{E}'_R = b'[\cos((\omega + \Delta\omega)t - k_+z) \hat{x} - \sin((\omega + \Delta\omega)t - k_+z) \hat{y}] \quad (2.52)$$

considering R- (L-) rotating beams with wavenumbers  $k_+$  ( $k_-$ ). Similar to the reference, the probe detector measures the superposition of their  $\hat{x}$  components, and keeps the  $\Delta\omega$  component by using a bandpass filter

$$P_{prob} = a'b' \cos(\Delta\omega t + 2\alpha) \quad (2.53)$$

where  $\alpha = \frac{k_+ - k_-}{2} z = \frac{\omega z}{2c} (N_+ - N_-)$  is the Faraday rotation. Although the reference and probe detectors have different amplitudes, the Faraday rotation is calculated from their phase difference, and is not affected by amplitude variations.

By introducing a third laser with a different frequency,  $\omega_3$ , as a local oscillator (LO) beam, either of the rotating probe beams, together with the reference beam, form a traditional interferometer. An advantage of this triple-laser interferometer/polarimeter system is that it measures both the Faraday rotation and interferometry signals with high time resolution ( $\sim 1\mu s$ ), and only one detector for each chord is used, which reduces cost and saves significant space for a compact multi-chord system. A challenge for this technique is that it needs well co-aligned laser beams. Misalignment between two probing beams will cause a systematic error on the Faraday rotation measurement, the details of which will be discussed in chapter 4.

#### (d) Photoelastic modulation methods

An alternative idea, instead of modulating the input beam, is to modulate the output beam after going through the plasma, with a photoelastic modulator (PEM). This approach has been applied to the CO<sub>2</sub> polarimetry systems on JT-60U [48] and C-Mod (in Figure 2-5) [49]. A linearly polarized beam is launched along x-direction, as a probing beam,

$$\vec{E} = a \cos(\omega t) \hat{x} \quad (2.54)$$

After going through the plasma, its polarization rotates by an angle  $\alpha$  (we neglect the signal amplitude change in the following analysis, as we only care about the phase).

$$\vec{E} = a \cos(\omega t) [\cos \alpha \hat{x} + \sin \alpha \hat{y}] \quad (2.55)$$

Then, the beam traverses a PEM, with the optical axis aligned in the x-direction. The output beam is then:

$$\vec{E} = a \cos(\omega t) \left[ \cos \alpha e^{\frac{iA}{2}} \hat{x} + \sin \alpha e^{-\frac{iA}{2}} \hat{y} \right] \quad (2.56)$$

$$A = A_0 \cos(\Omega t) \quad (2.57)$$

where  $A$  is the optical retardation of the PEM, and  $\Omega$  is the angular frequency of a piezoelectric transducer (PZT) used to stress the photoelectric element.

A polarizer orientated at  $45^\circ$  with respect to the x-axis picks up part of the laser beam which is then directed onto a square-law detector.

$$\vec{E}_{det} = \frac{\sqrt{2}}{2} a \cos(\omega t) \left[ \cos \alpha e^{\frac{iA}{2}} + \sin \alpha e^{-\frac{iA}{2}} \right] \frac{\hat{x} + \hat{y}}{\sqrt{2}} \quad (2.58)$$

$$P_{det} = |\vec{E}_{det}|^2 = \frac{a^2}{4} [1 + \cos(2\omega t)] [1 + \sin 2\alpha \cos(A_0 \cos(\Omega t))] \quad (2.59)$$

If we filter out the high frequency component ( $2\omega$ ), and then expand the detector power in Bessel functions, we get

$$P_{det} = \frac{a^2}{4} [1 + \sin(2\alpha) J_0(A_0) + 2 \sin(2\alpha) \sum_{n=1}^{\infty} J_{2n}(A_0) \cos(2n\Omega t)] \quad (2.60)$$

We find the ratio of the amplitude of the second harmonic to the DC component is then

$$V_r = \frac{2 \sin(2\alpha) J_2(A_0)}{1 + \sin(2\alpha) J_0(A_0)} \quad (2.61)$$

and the Faraday rotation is

$$\alpha = \frac{1}{2} \sin^{-1} \left( \frac{V_r}{2J_2(A_0) - V_r J_0(A_0)} \right) \quad (2.62)$$

as long as the maximum retardation  $A_0$  is known.  $A_0$  depends on both the setup of the PEM (applied voltage on PZT) and the incident angle of the linearly polarized beam. A calibration by rotating the incident beam angle is necessary to find  $A_0$  [50]. With this method, only one laser is necessary, and one detector is required for each channel.

A disadvantage of this method is that the PEM is limited to short wavelengths, typically only available up to the near infrared region. Recently, a PEM for a wavelength of  $\sim 50 \mu\text{m}$  has

been developed and bench tested by Akiyama [50]. With the development of a PEM for longer wavelengths, this modulation method may receive wider application for future polarimetry systems.

Another disadvantage is that the time resolution for this method is only up to tens of kHz, which is determined by the modulation frequency of the PEM. The fluctuation measurement capability is thus restricted when using this technique.

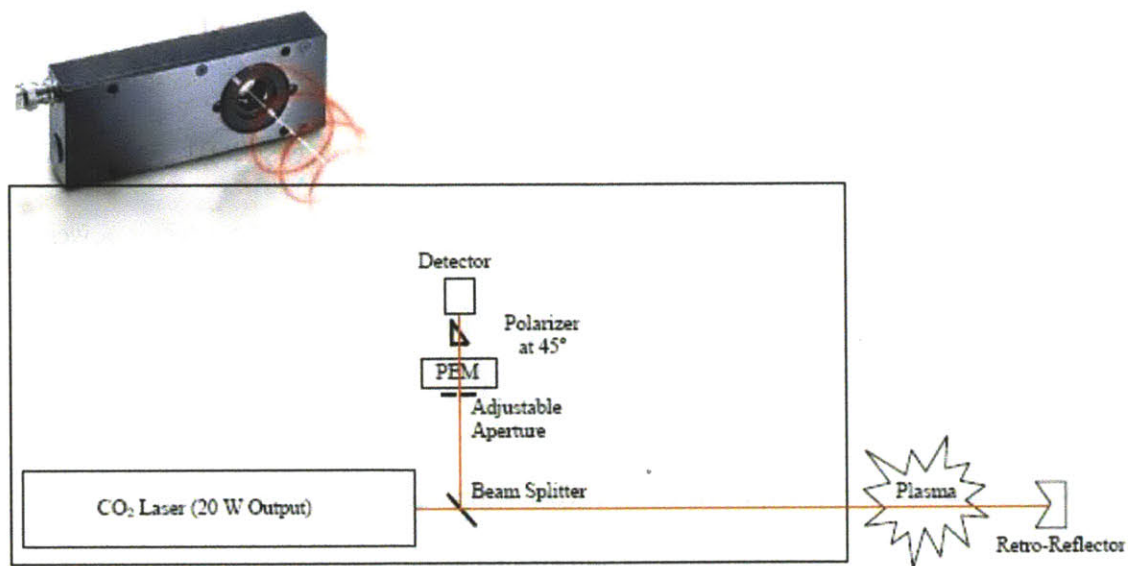


**Figure 2-5: Schematic of the PEM polarimeter configuration on C-Mod. (Figure from [49])**

### 2.2.2 Different Viewing Geometries

Early interferometer/polarimeter systems were developed with vertical viewing geometry. Since the laser beams went through vertical port windows, in-vessel optics were not needed. With this geometry, it is convenient to design a multi-chord system either by expanding the incident beam to a large slab beam, or by splitting it into multiple, discrete beams. The polarimeters on TEXTOR (Figure 1-1), MTX, RTP and MST all adapted this geometry, with approximately 10 chords of simultaneous measurements, which achieved low noise level [33][34][47][45].

However, on C-Mod, constraints of the vertical port geometry would limit the interferometry/polarimetry chords to the core plasma, missing the edge.

To achieve better profile inversions, the chords should fully span the whole plasma cross-section. A multi-chord poloidal viewing polarimetry was developed for this purpose, and has been implemented on JET, and C-Mod, and is proposed for ITER. The laser beams are injected into the machine through a horizontal port window, and reflected back by corner-cube retro-reflectors installed in the inner wall. The beams have to be split and directed into the machine with different incident angles, which make a multi-chord compact design challenging.

A radially viewing polarimeter designed for NSTX-U has been tested on DIII-D [31][36]. The probing beam has a long wavelength ( $\lambda=1.04 \text{ mm}$ ) and is reflected by the inner-wall tiles instead of in-vessel optics. By scanning the toroidal field, the relative dominance of Faraday rotation and C-M effects have been studied. This system shows promise for diagnosing global magnetic fluctuations.

Some polarimeters are designed with a tangential geometry [37][51]. The laser beams enter the machine through a tangential port window, and hit retro-reflectors mounted in the outer wall or outside the vacuum vessel. Because the toroidal magnetic field can be well known, tangential polarimeter can be used to measure the line averaged plasma density. The Faraday rotation is usually less than  $2\pi$ , and thus it has no fringe jump issue, and can be a more robust way to measure the density than an interferometer. LHD has implemented a  $\text{CO}_2$  tangential polarimeter with a noise level below  $0.01^\circ$  at 3 ms time resolution [51]. A  $\text{CO}_2$  tangential polarimeter is also proposed for installation on ITER [52].

### 2.3 Current Density Profile

Both interferometers and polarimeters yield line-integral measurements. To measure electron density and current density profiles, the line-integrated data needs to be inverted to get the local plasma quantities.

Various techniques have been used to invert interferometry data in order to derive profiles [15]. A typical method is to use Abel inversion [38], which works well for a circular plasma. For a D-shaped plasma, more complicated techniques are used. We can discretize the density profile into some unknown density parameters according to the magnetic flux surfaces, and the interferometry integral for each chord becomes a summation of the density parameters weighted by the path-lengths between flux surfaces. The multi-chord measurements can be represented as a matrix:

$$A n_{\psi} = \phi \quad (2.63)$$

where the matrix  $A$  contains the path-length information for each chord,  $n_{\psi}$  is the unknown density vector, and  $\phi$  is the interferometry phase vector. The dimension of  $\phi$  (chord number) has to be larger than that of  $n_{\psi}$ , so that  $n_{\psi}$  can be solved by non-linear least square method. Direct inversion of  $A$  numerically may cause large errors, so Singular Value Decomposition (SVD) techniques [53] are typically used to invert  $A$ , and then calculate the density profile matrix using:

$$n_{\psi} = A^{-1} \phi \quad (2.64)$$

The poloidal magnetic field, as a vector, is much more difficult to be inverted from the polarimetry data, since the projected magnetic field components on the beampaths are different, even on the same magnetic flux surface. An inversion technique by using Fourier expansion of the magnetic field profile was developed for the proposed ITER polarimeter, and high-resolution plasma current profiles were successfully generated in a numerical simulation [54]. The expansion contains a large number of base functions, so a large number of polarimetry chords (16-chord data used in the reference) is necessary to achieve an inversion with reasonable accuracy.

An alternative approach, which requires fewer measurement chords, is to fit the current density profile or q-profile with a model function characterized by some free parameters [55][56]. For Ohmically driven plasma, a simple toroidal current profile model might be assumed as

$$J = J_0 \left[ 1 - \left( \frac{r}{a} \right)^2 \right]^m \quad (2.65)$$

where  $J_0$  is the on-axis current density and  $a$  is the minor radius. In this case there is only one free parameter,  $m$ , considering that  $J_0$  is constrained by the total plasma current. The location of the magnetic axis can be determined by the polarimetry chords around the magnetic axis, when the chords are purely vertical or horizontal and the plasma is left-right or up-down symmetric, as the sign of the Faraday rotation changes across the magnetic axis. The internal magnetic field can be calculated by the plasma current model with the location of the magnetic axis. We can integrate the density from the interferometer and the magnetic field along the beam-paths, to get the simulated polarimetry signals. The free parameter  $m$  is obtained by minimizing the errors between the simulation and the measurement data. Since this method only takes the total current and interferometry and polarimetry data as input, the time resolution can be very good ( $\sim 1 \mu\text{s}$ ). The limitation is that the current density profile model will most likely be unacceptable during LHCD.

A more accurate and robust method is to incorporate the polarimetry data into EFIT as an internal constraint. Kinetic-EFIT takes external magnetic field, plasma pressure profile, MSE pitch angles (if available), sawtooth inverse radius and total plasma current as constraints, and can produce a more accurate current density profile reconstruction than normal EFIT, which uses only the external magnetic measurements to constrain the reconstruction. With extra information from the polarimeter, it should be possible to further improve the EFIT reconstruction accuracy of parameters, such as the plasma elongation, since the polarimetry contains off mid-plane measurements. As shown in section 5.4, this is indeed the case. A multi-chord polarimeter constrained EFIT (without MSE) will have good time resolution, and could be used to measure the current density profile for real-time feedback during the plasma discharge.



### **3. Development of the Polarimeter Diagnostic on C-Mod**

The C-Mod Polarimetry system uses Far Infrared (FIR) lasers, for reasons that will be made clear later in this chapter. Since there are few commercially available optical components for FIR wavelengths, most of the optics had to be custom designed. The C-Mod Polarimeter is designed with a poloidal viewing geometry, which requires in-vessel optics, and thus is more complicated than the typical vertical viewing polarimeter, used on many of the other facilities.

A multi-chord polarimetry system has been developed for C-Mod thus far, while the addition of a third laser would allow interferometry to be added in the future. A single chord proto-type polarimetry system was installed in the C-Mod cell for the 2010 C-Mod campaign, which was then upgraded to three chord measurements for the 2012 campaign. An upgrade to six chords with an interferometer-polarimetry combined system has been planned for the near future. The schematic design and the three-chord system geometry will be described in section 3.1. Details of the lasers, optics, detectors and optical path design will be presented in section 3.2.

#### **3.1 Measurement Scheme and System Geometry**

##### **3.1.1 Schematic Measurement Scheme**

The C-Mod polarimetry system uses the Dodel-Kunz method [35] to measure the Faraday rotation. As shown in Figure 3-1, two laser beams with a 4 MHz intermediate frequency (IF), which is tunable over a 10 MHz bandwidth with little laser power loss, are combined with a half-waveplate and a wire-mesh polarizer. Two orthogonal beams pass through the quarter-waveplate resulting in two co-aligned counter-rotating circularly-polarized beams. A small percentage of the laser beam power is reflected by a beam-splitter to produce a reference signal, and the remaining power goes through the plasma with a poloidal view, hitting the corner-cube retro-reflectors mounted in the inner wall, is reflected back, and finally reflects off another beam-splitter.

The detected signals with the phase information are amplified and then recorded by high speed digitizers (up to 20 Msps). A frequency meter (shown by the dotted line box in Figure 3-1) is used to lock one laser frequency relative to the other. The reference signal is passed into the frequency meter, which produces a voltage signal proportional to the deviation of the IF from the target frequency ( $IF - IF_{\text{target}}$ ). This signal is integrated and fed back to a piezoelectric transducer (PZT), which controls the length and therefore the operational frequency of the FIR cavity, and thus keeping the IF locked to the target frequency.

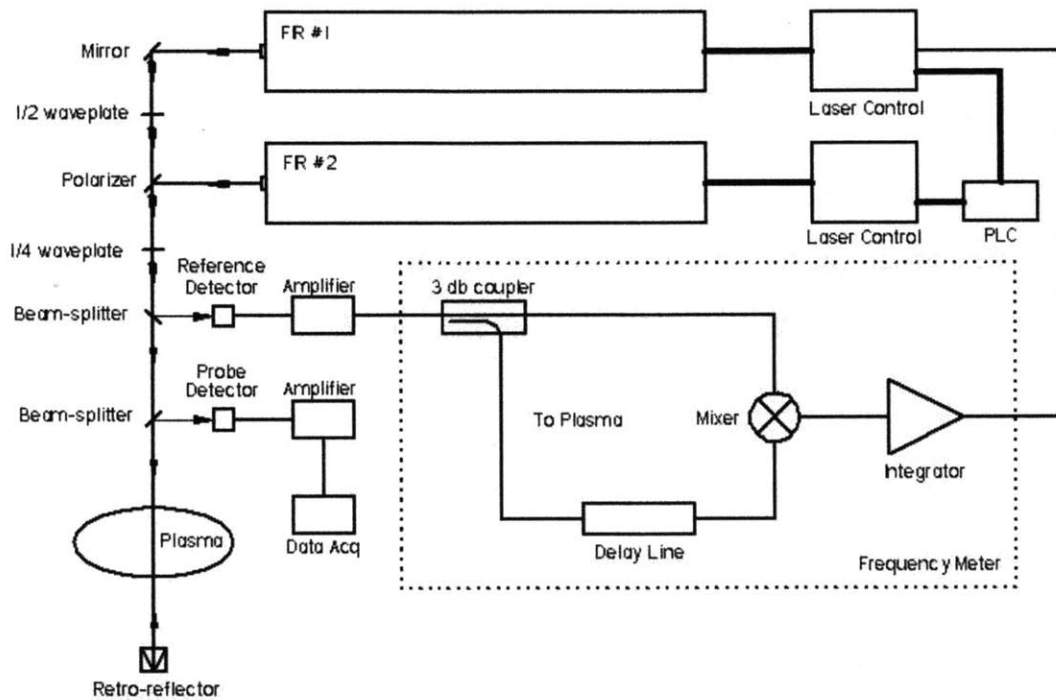


**Figure 3-1: Schematic design for the polarimetry system on C-Mod**

### 3.1.2 Three-Chord Geometry

In Figure 3-2, the geometry of the three-chord double pass polarimetry system is shown, from the laser source to the corner-cube retro-reflectors mounted within the inner wall of C-Mod. The lasers are located on the lower optical table (1.3 m x 3 m x 0.3 m) sitting on the C-Mod cell floor.

Two lasers are stacked together, which makes it easier to deal with the laser power cables and gas lines, while keeping the output window of two lasers close to each other. It also saves space for other components on the optical table, considering the big size of the FIR lasers. Air pucks are installed between the table legs and the table surface, and Sorbothane<sup>™</sup> is installed between legs and cell floor, both of which greatly reduce vibrations of the lower table. The laser beams are collimated using a 3 m radius of curvature spherical mirror, and are then directed to a second optical table (0.9 m x 1.8 m x 0.07 m) that is attached to the mechanically very stable 60 cm thick concrete igloo that surrounds C-Mod. On the upper table the beam is split into a reference beam and three chords that probe the plasma, as shown in Figure 3-3. A reference beam is picked off from the chord#1 beam with a beam-splitter. Plano-convex plastic TPX lenses focus the probe beams onto the 13 mm aperture of the retro-reflectors located on the inner wall. The return beam from the retro-reflector for each chord is picked off by another beam-splitter and focused onto a detector by a 90° off-axis parabolic mirror. The detector is mounted on a 3-axis linear stage combined with a goniometer and a rotation stage, and thus has the flexibility of both position and angle adjustment to achieve the best signal level. The overall path length from lasers to the probe detector is roughly 14 m.

Although the polarimetry system can only make three chord measurements simultaneously, it has flexibility to choose from any three of the six available measurement positions. The six chords available for viewing are shown with the cross section of typical poloidal magnetic flux in Figure 3-4 and are located from 0.04 to 0.39 m above the mid-plane on the inner wall. All six chords must be above the magnetic axis at this point, since the viewing position and angle of the polarimetry system are restricted by other diagnostics on the same horizontal port. The projected distances (defined as  $x$ ) from the magnetic axis to these chords are 10, 16, 20, 23, 29, 35 cm. All chords enter the vessel through a single z-cut quartz vacuum window which does not affect the state of polarization of the probe beam. During operations, chords with  $x=10$  (#1) and 16 (#2) cm are always used, and the third channel (#3) is typically

alternated between  $x=20$  and 23 cm. When it is upgraded to a six chord measurement, at least one chord will view below the mid-plane of the machine, which will help to derive central safety factor ( $q_0$ ) directly from Faraday rotation measurements near the magnetic axis [56], and also enhance the ability to differentiate magnetic fluctuations from density fluctuations, as will be discussed in chapter 6.

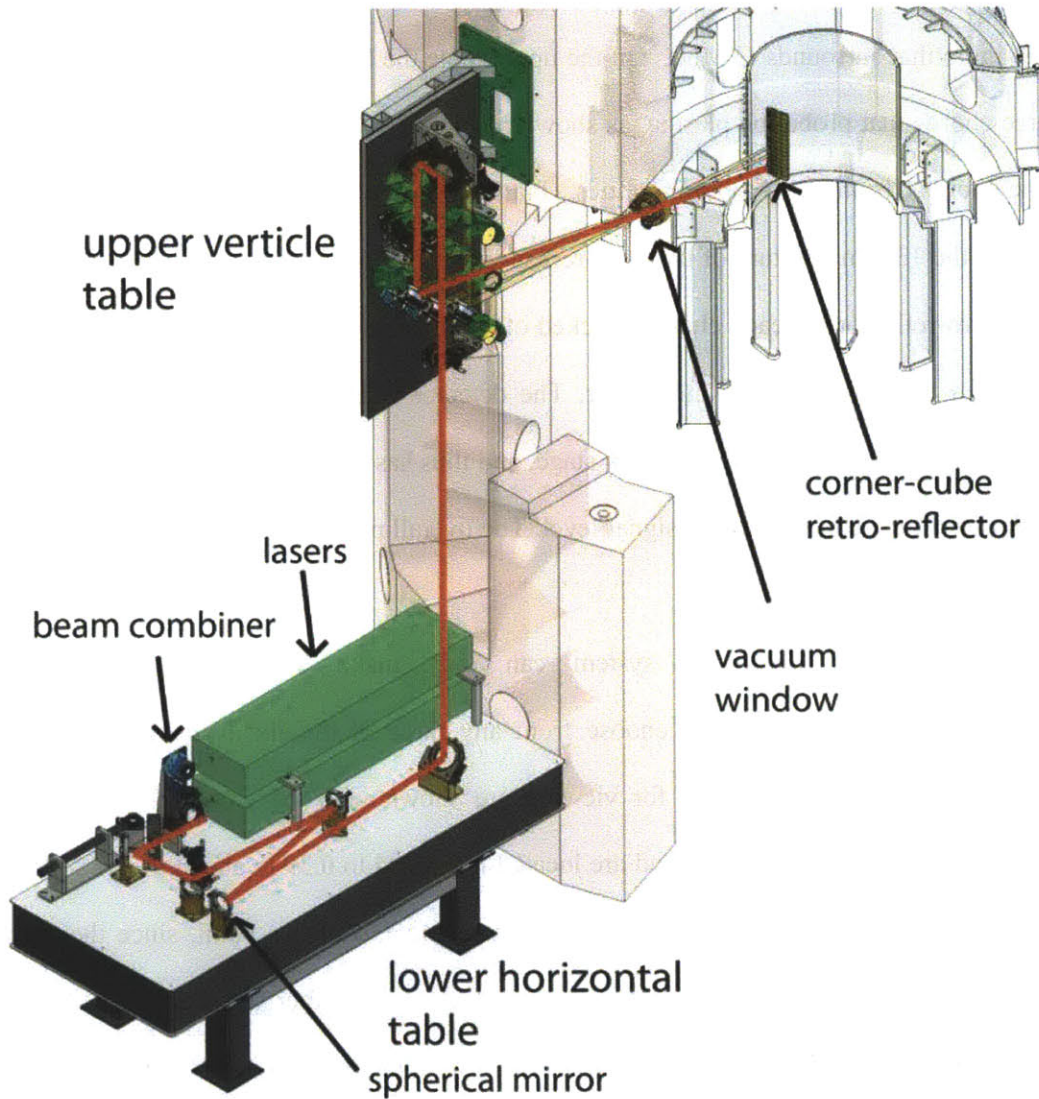


**Figure 3-2: System geometry for the three-chord double-pass polarimeter on C-Mod. To simplify the optical path in the figure, only the beam for one chord (red line) is shown.**

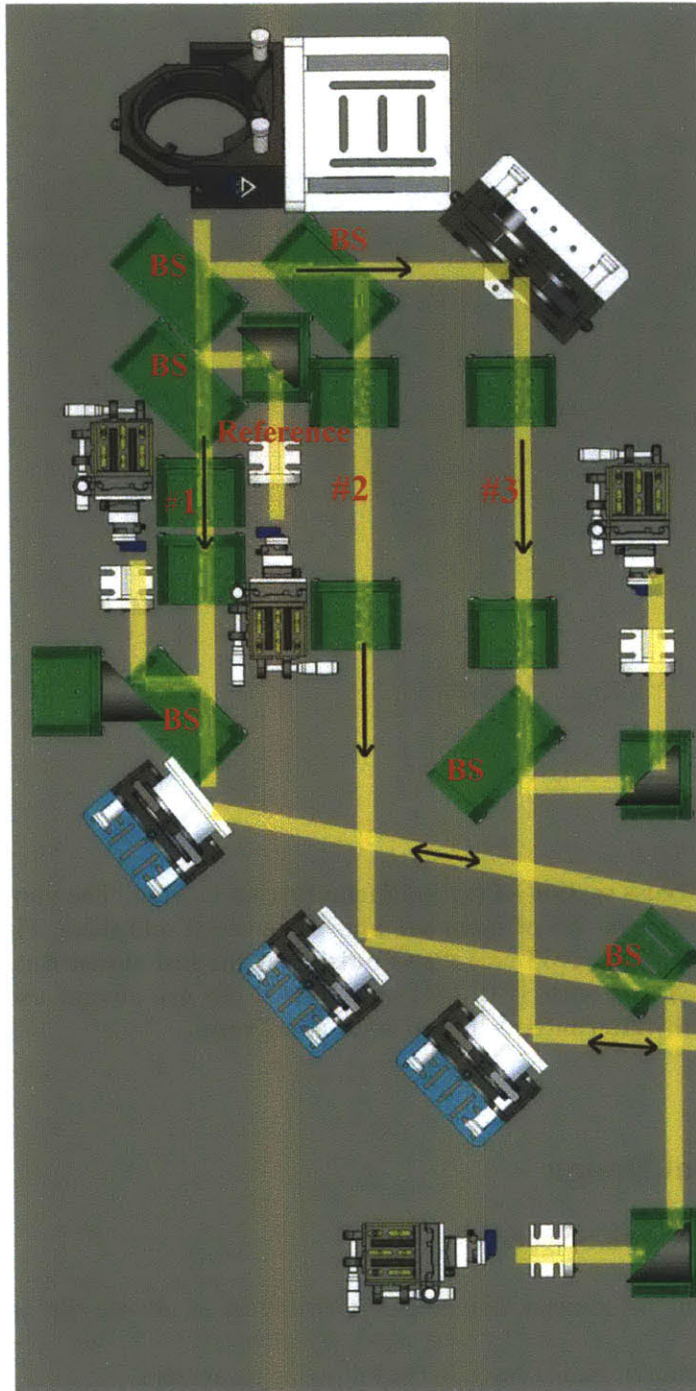


**Figure 3-3: Optical layout on the upper table. Yellow lines are beam paths. The beam from the lower table is split into a reference and three probe beams by beam-splitters (BS). Each chord has a quartz-waveplate to transfer beams into circularly-polarized beams and a TPX lens to focus the beams onto the retro-reflectors.**

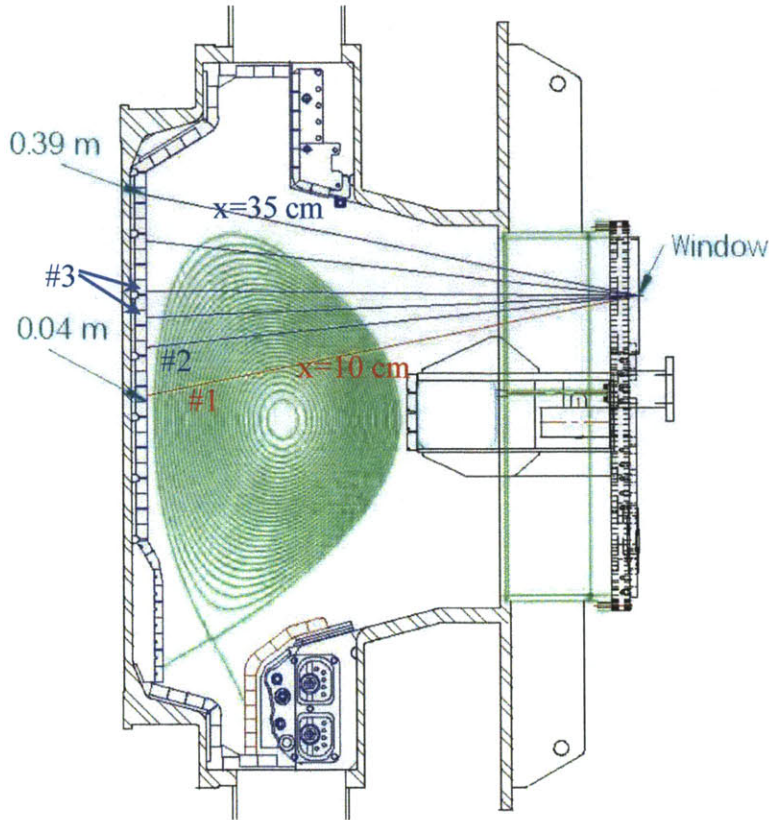


**Figure 3-4: Poloidal cross section of the magnetic flux on C-Mod. The viewing paths for six available chords are shown. All of them are above the vessel midplane. The top chord with retro-reflector at  $z=0.39$  m ( $x=35$  cm) views outside of the last closed flux surface (LCFS). During operations, chords with  $x=10$  (#1) and 16 (#2) cm are always used, and the third channel (#3) is typically alternated between  $x=20$  and 23 cm.**

## 3.2 Instrumental Design

### 3.2.1 Laser Wavelength Selection

To design a successful polarimetry diagnostic, it is critical to choose the proper laser source according to several criteria, as discussed in the following paragraphs.

The Faraday effect needs to be large enough for accurate measurements. Since the Faraday rotation signal is proportional to  $\lambda^2$  (Equation 2.30), it is desirable to choose a long wavelength to get good signal-to-noise ratio. However the Cotton-Mouton (C-M) effect is proportional to  $\lambda^3$  (Equation 2.37), and we want to make sure it is not much larger than the Faraday effect, which might contaminate the Faraday rotation measurements.

When the laser beam propagates in the plasma, we need to make sure the refraction of the laser beam by plasma density gradient is small. Therefore, the laser wavelength should not be too long, as the refraction is proportional to  $\lambda^2 \nabla n_e$ . For a vertical-viewing single pass polarimetry system, the beam offset on detectors due to plasma refraction might be significant, considering the long distance from plasma to detectors. Therefore, the signal amplitude changes significantly during a plasma discharge, especially for edge channels which have suffered large refraction effects. For the C-Mod polarimetry system, this refraction problem is minimized with a poloidal-viewing double pass geometry. Assuming the retro-reflectors on the inner-wall work perfectly to reflect the beams back along the original path, the beam offsets on the detectors should be negligible. For the C-Mod system it is important to make sure the beam deviation is small at the inner-wall where the retro-reflector is mounted. A large refraction effect in the plasma would deflect the laser beam away from the center of the retro-reflectors, and there could be significant beam power loss and increased error in the phase measurements. Ray tracing simulations of laser beams in C-Mod plasmas show that the refraction effect is small (Table 3-1& Table 3-2) over the range of plasmas of interest.

The laser wavelength also determines the size of the beam required to allow a properly sized focal spot at the inner wall retro-reflector from outside the vacuum vessel (Gaussian beam propagation), which sets a limitation on the number of polarimetry chords that can be accommodated in the limited space available. If we choose a longer wavelength, the beam size for a given propagation path is larger, and it is more difficult to build multiple chord systems compactly. This effect also restricts the chordal spatial resolution.

To optimize the laser wavelength, consideration is also given to the availability of commercial detectors. High sensitivity detectors for the particular laser wavelength we choose are desirable. Details about the detectors will be discussed in section 3.2.8.

In order to quantify the measurement signal levels and refraction offsets, three laser wavelengths from the IR into the FIR region ( 10.6  $\mu\text{m}$ , 117.73  $\mu\text{m}$  and 432.6  $\mu\text{m}$  ) have been

analyzed using typical L-mode and H-mode C-Mod plasma discharges. The expected Faraday rotation, C-M and interferometric responses are simulated numerically using Thomson Scattering measured density and the magnetic field from EFIT, both of which are mapped to the polarimetry chord path. Table 3-1 and Table 3-2 list the Faraday rotation, C-M and interferometric responses for chord#1. The refraction is the max vertical beam displacement on the inner wall for all six chords.

**Table 3-1 : Laser wavelength selection. Shot# 1080320019 (L-mode) at  $t=1.0$  s,  $n_{l04} \approx 0.5 \times 10^{20}/m^2$ ,  $I_p \approx 830$  kA,  $B_t = 6.2$  T. (Phase signals are for chord#1. Refraction is the max beam displacement on inner wall)**

Wavelength( $\mu m$ )	FR/deg	C-M/deg	Interferometer/fringes	Refraction/mm
10.6	0.03	0.003	0.19	0.01
117.73	3.9	3.8	2.1	0.14
432.6	52	190	7.8	1.8

**Table 3-2: Laser wavelength selection. Shot# 1120614012,  $t=1.0$  s (H-mode),  $n_{l04} \approx 2.9 \times 10^{20}/m^2$ ,  $I_p \approx 830$  kA,  $B_t = 5.2$  T. (Phase signals are for chord#1. Refraction is the max beam displacement on inner wall)**

Wavelength( $\mu m$ )	FR/deg	C-M/deg	Interferometer/fringes	Refraction/mm
10.6	0.16	0.011	1.06	0.01
117.73	20.1	15.5	11.8	1.7
432.6	272	770	43.2	18

According to the tables, 117.73  $\mu m$  has reasonable Faraday and C-M effect for both L-mode and H-mode plasmas, while keeping the refraction low compared to the size of the retro-reflectors (13 mm in diameter), and thus has been chosen as the operating wavelength for the C-Mod polarimetry system.

### 3.2.2 FIR Laser System

Two commercially available CO<sub>2</sub> pumped, FIR lasers are used in the polarimeter diagnostic (Coherent SIFIR-50 FPL). They operate at 117.73 μm with 150 mW each, using difluoromethane (CH<sub>2</sub>F<sub>2</sub>) as the fill gas.

The operating gas pressure for each laser cavity is optimized to for maximum FIR laser power. The optimal pressure was measured for the two lasers, as shown in Figure 3-5: FIR#1 has a peak power for p~650 mTorr, while FIR#2 has a peak power for p~750 mTorr. If the laser cavities are filled with gas and then isolated, a continuous gas pressure increase was observed at a rate of ~3 mTorr/min for each laser. An analysis of the gas in the cavities with a Residual Gas Analyzer indicated that the pressure change comes from outgassing of the fill gas from the laser cavity, and not a leak of outside air. To maintain the optimal gas pressure, a dynamic gas pressure control system was developed, which continually feeds the lasers with new gas while pumping out the old gas. The Programmable logic controller (PLC) controlled gas system keeps the laser gas at the optimized pressure.

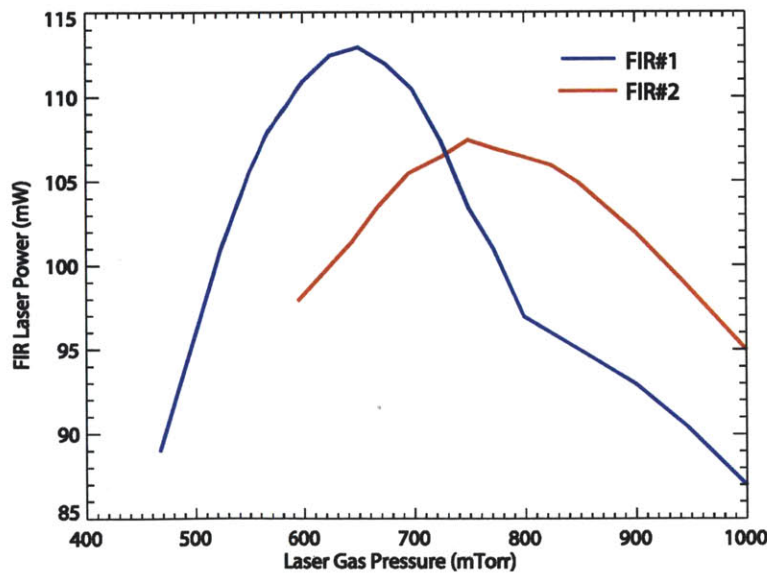
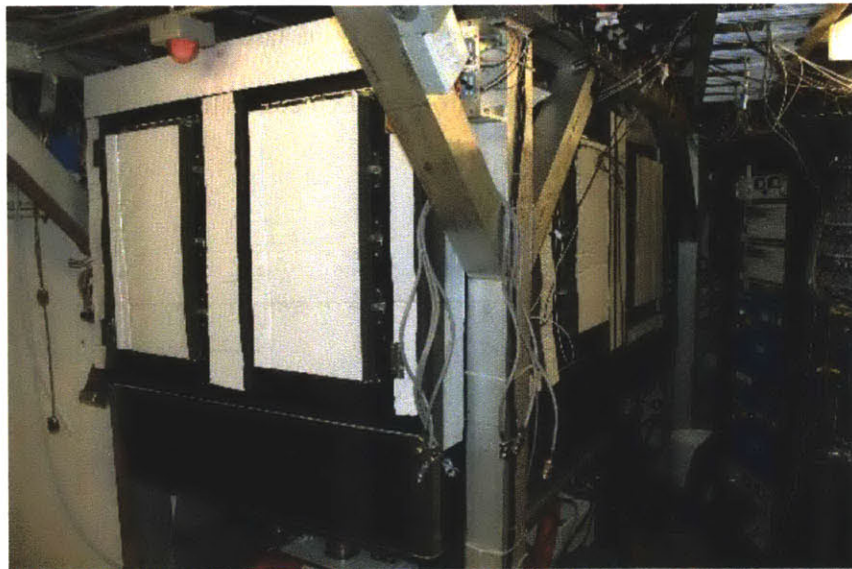
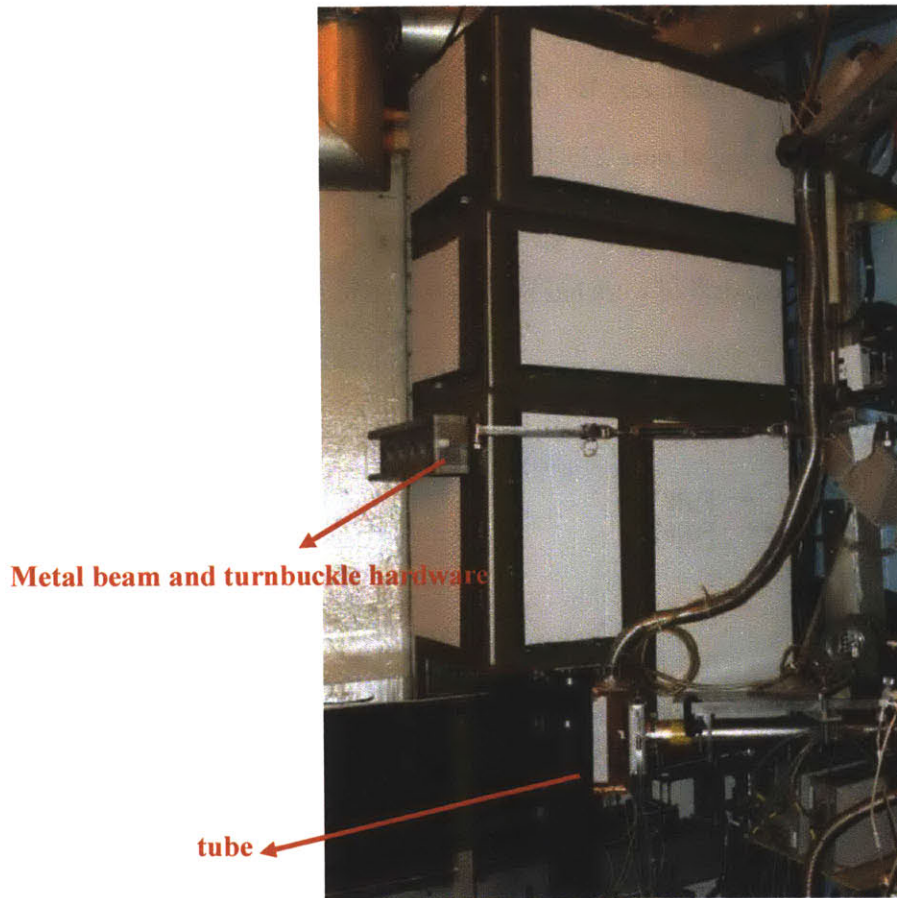


Figure 3-5: FIR#1 has a peak power for p~650 mTorr, while FIR#2 has a peak power for p~750 mTorr

The FIR laser beam at  $117.73\ \mu\text{m}$  is extremely sensitive to the water vapor absorption. FIR power would be significantly attenuated if the 14 m long beam path was exposed to room air. Air-tight enclosures (Figure 3-6 and Figure 3-7) were designed to seal the whole optical path, and the two enclosures are connected by a 12.5 cm aperture tube. By purging with dry air, the relative humidity in the enclosures is reduced from 50% to less than 2%, at which point the attenuation is less than 20 %. Panels in each enclosure provide feedthroughs for power, control, and signals. Easily removable side panels provide good accessibility for optical adjustments. The enclosure walls are covered with acoustic absorber material that will be discussed in more detail in chapter 4.



**Figure 3-6: Air tight enclosure for the lower table. Detachable side panels in the enclosures provide good accessibility for optical adjustments**



**Figure 3-7: Air tight enclosure for the upper table. The tube connecting the two enclosures is shown. Detachable side panels in the enclosures provide good accessibility for optical adjustments.**

The FIR laser power and frequency drift over time, especially while the laser is warming up. A PZT controlled rear mirror on the FIR laser cavity allows the operating frequency of the laser to be varied over a range of approximately  $\pm 5$  MHz around line center. The 100 Hz bandwidth of this PZT system allows the lasers to be frequency locked with a response time faster than most mechanical drifts and vibrations in the optical system. A frequency meter, as described in section 3.1, drives the PZT for one of the lasers and locks the IF. An FIR power peaking system to optimize each of the laser powers is also available, but it is usually not turned on, because the laser power is relatively stable after warming up about one hour and the phase measurements are not affected by small changes in laser power (the phase measurement

technique was discussed in chapter 2). One serious issue for the PZT system is that the mount for the FIR PZT has a mechanical resonance. By driving the PZT of either laser with a signal generator, we found a resonant signal near 235 Hz on FIR#1 (210 Hz on FIR#2), as shown in Figure 3-8. Noise around these frequencies is observed on IF and Faraday rotation signals during the plasma discharges and a great deal of work has been expended to reduce this effect.

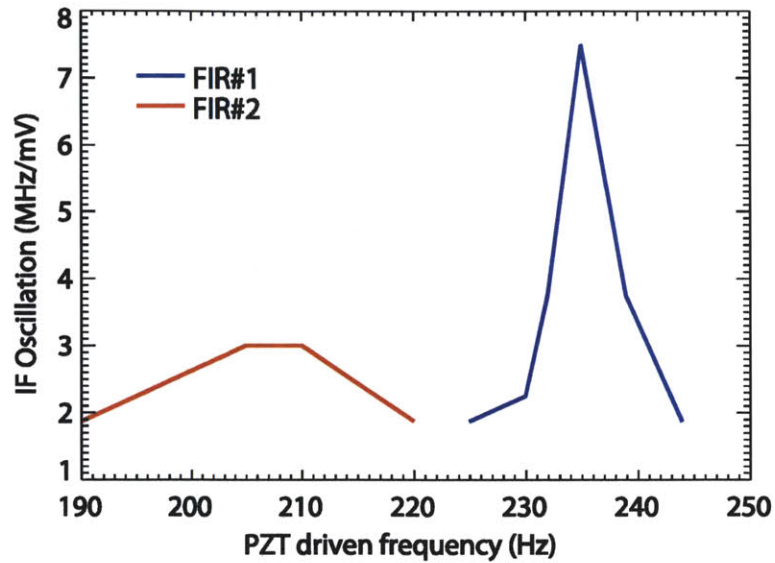


**Figure 3-8: Resonant peaks found on IF signal, when driving the PZT with input signals near 235 Hz (FIR#1) or 210 Hz (FIR#2). The Y axis is the change in the signal IF frequency for 1 mV of drive to the PZT.**

The lasers are located about 4 m from the tokamak, and experience time varying magnetic fields of up to 200 G during plasma discharges. This strong magnetic field affected the Invar<sup>®</sup> components inside the laser cavity during initial tests of the polarimeter on C-Mod. As shown in Figure 3-9(a), the IF frequency drifts dramatically, by more than 1 MHz, and the detector root-mean-square (RMS) voltage dropped to near zero during the plasma discharge. To shield the lasers from these stray magnetic fields, a steel enclosure (Figure 3-10) roughly 1.25 cm thick was built up from 0.625 mm thick plates as a laminate structure. This enclosure covered both lasers, with cutouts to allow for power, control, and cooling interfaces. The enclosure

successfully reduced the stray magnetic field to  $\sim 20$  G as measured by a Gauss-meter mounted close to the lasers inside the shield. From Figure 3-9(b), and the laser stability is greatly improved with the magnetic shielding installed. Although the residual stray field effects are still observable, the IF signal remains locked, and the drift of detector RMS voltage is less than 10% during the plasma discharge. The change in IF frequency was reduced to less than 80 kHz with the addition of the magnetic shielding.

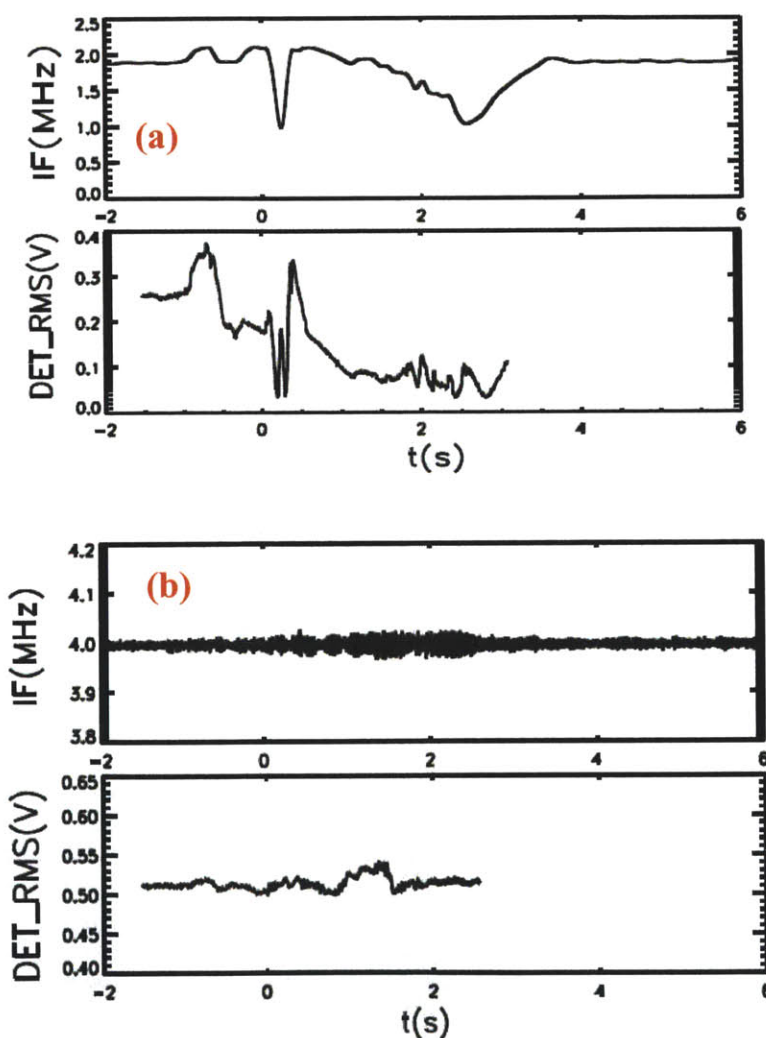


**Figure 3-9: (a) Significant drift on IF ( $>1$  MHz) and detector RMS voltage dropped to near zero without magnetic shielding (b) Minor drifts on IF ( $< 80$  kHz) and detector RMS voltage with magnetic shielding**

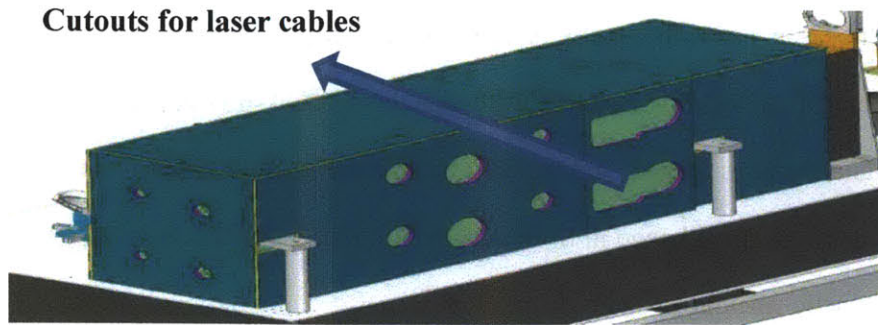


**Figure 3-10: Both lasers boxed in a steel enclosure to reduce the stray field effects**

### 3.2.3 Gaussian Beam Propagation

For lasers operating in the FIR range of wavelengths over path lengths similar to those needed for the C-Mod polarimeter, the geometric optics approximation can no longer be used to model the beam propagation. Gaussian beam theory must be applied to analyze the effects of diffraction on the laser beam radius ( $w$ ) along the beam path ( $z$ ). The beam radius at a distance  $z$  from a beam waist can be calculated as

$$w(z) = w_0 \sqrt{1 + \left(\frac{z}{z_R}\right)^2} \quad (3.1)$$

where  $z_R = \frac{\pi w_0^2}{\lambda}$  is the Rayleigh length, and  $w_0$  is the 1/e E-field waist radius.

In order to obtain a waist radius of 5 mm on the retro-reflector, the beam radius must be ~23 mm at a 3 m distance from the retro-reflector, which is the closest possible position for the TPX lens. Therefore, to capture 99% of the beam power, most of the optics on the upper table should have a clear aperture of ~10 cm. Some of the mirrors and beam-splitters are 15 cm in diameter, as they are installed at 45° relative to the incident beam.

To evaluate the beam size along the whole beam path, we need both the size and position of the beam waist for the FIR lasers. The laser beam size has been measured at a couple of

locations near the laser output window with a pyro-electrical detector. The beam waist is found near the laser beam output window and has a radius of  $\sim 5$  mm. The beam size along the whole beam path is calculated by the optics design program (OSLO), some results of which are shown in Figure 3-11. The beam radius freely expands to 23 mm before being collimated by a 3 m spherical mirror, and then propagates for  $\sim 5$  m with little change in size. The beam is then focused down by a 3 m focal length TPX lens to a 5 mm waist at the retro-reflectors. The beam radius on the vacuum window is  $\sim 7.8$  mm.

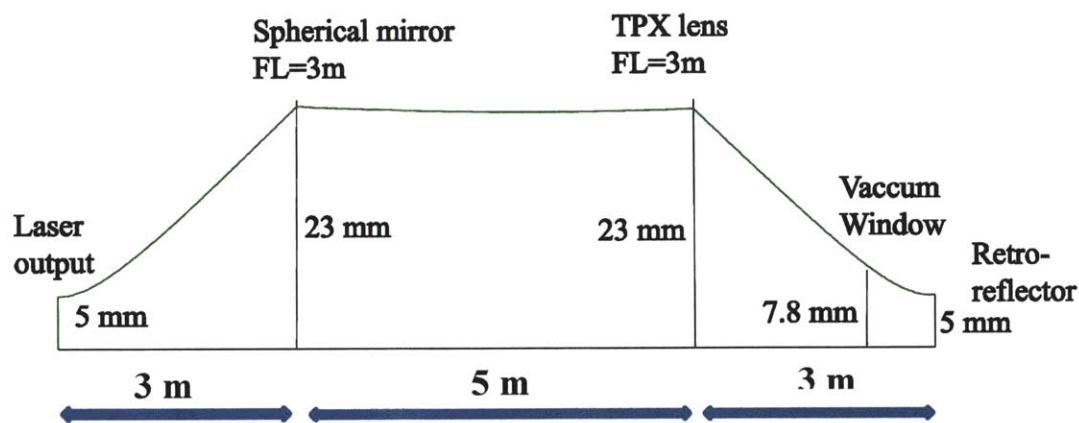


Figure 3-11: Gaussian Beam radius along the laser beam path.

### 3.2.4 Quartz Vacuum Window and Waveplates

Since quartz has a low absorption coefficient for FIR laser power and is also transparent for the visible alignment laser, it is a very good choice to be used for vacuum window and wave-plates for the C-Mod polarimeter. Quartz is anisotropic but its optical properties can be defined simply using an xyz rectangular coordinate system. A z-cut quartz plate is produced by cutting the quartz bar perpendicular to the z-axis (ordinary axis). The refractive index for the whole xy-plane is  $N_o$  (ordinary refractive index), thus the z-cut plate does not change the polarization of the incident beam, and can be used as a vacuum window. X-cut quartz plates are produced by cutting

the quartz bar perpendicular to the x-axis. In that case, the y and z axes have different refractive indexes, and can thus be designed as wave-plates to modify the incident beam state of polarization.

The vacuum window for the C-Mod polarimeter consists of a 10 cm diameter, 3.5 mm thick, z-cut quartz plate. Initial tests show the transmission rate of the laser power through the quartz plate was around 50%-70%, depending on the incident angle, because of the multiple reflections by the window surfaces (the red curve in Figure 3-12). Since the beams can enter the window off-normal by up to  $23^\circ$  for the poloidal viewing geometry, a smooth response with changing incident angle was of great importance for the vacuum window. The air side of the window was therefore anti-reflection (AR) coated with a 0.020 mm thick LDPE film. The transmission for the quartz plate with this coating is much more constant than for the uncoated window within a  $\pm 30^\circ$  incident angle (green curve in Figure 3-12). The 30% power loss comes from the absorption in the quartz and losses at the second window surface. The vacuum side of the window could not be coated, since no high-vacuum compatible material could be found for that coating.

Another reason to choose quartz as the vacuum window material is that it causes a negligible systematic error. With strong magnetic field, the vacuum window itself may change the laser polarization, leading to systematic errors in the polarimetry measurements. The Faraday rotation from the window is

$$\Delta\varphi = V_{\text{window}}B_pD \quad (3.2)$$

where  $V_{\text{window}}$  is the Verdet constant,  $B_p$  is the magnetic field parallel to the beam, and  $D$  is the window thickness. To eliminate this error, the vacuum window needed to be made of material with a small Verdet constant, such as quartz and diamond for FIR wavelength. Magnetic field-only test shots confirm the Faraday rotation from the quartz vacuum window is negligible.

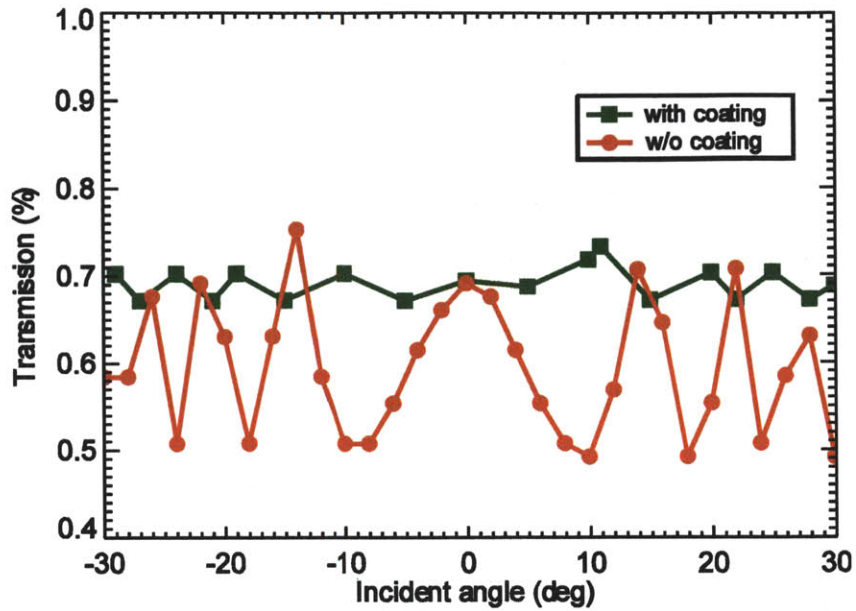


Figure 3-12 : Comparison of the transmission rate of the quartz window with and w/o AR coating.

Waveplates used in the polarimeter system are x-cut quartz plates with the thicknesses specifically designed for  $\lambda=117.73 \mu\text{m}$ , using the following formulas:

$$N_x = 2.16960, N_o = 2.12062$$

$$L_{\frac{1}{2}} = \frac{\lambda}{2(N_x - N_o)} = 1.202 \text{ mm} \quad (3.3)$$

$$L_{\frac{1}{4}} = \frac{\lambda}{4(N_x - N_o)} = 0.601 \text{ mm} \quad (3.4)$$

where  $N_x, N_o$  are refractive indices along the extraordinary (y) and ordinary (z) axes [57], and  $L_{\frac{1}{2}}, L_{\frac{1}{4}}$  are the design thicknesses for the half-waveplates and quarter-waveplates. A 5 cm diameter half-waveplate is used to rotate the horizontal linearly polarized beam to a vertically polarized beam. A 10 cm diameter quarter-waveplate converts the linear polarized beams to counter-rotating circularly polarized beams for each chord, with the polarization of the incident beams at  $45^\circ$  relative to the optics axes.

Without coating, the transmission for the half-waveplate and quarter-waveplate was only 55% and 70% respectively. The quarter-waveplates did not work well at converting linear-polarized beams into circularly-polarized beams because of multiple reflections between the waveplate surfaces. A linearly polarized beam was converted into a beam with large ellipticity ( $\sim 1.3$ ) after passing through a quarter-waveplate. After coating both sides of the waveplates with LDPE films, the transmission is improved to  $\sim 85\%$  for the half-waveplate and  $\sim 90\%$  for the quarter-waveplate. The ellipticity of the laser beam after going through the coated quarter-waveplate was reduced to  $\sim 1.1$ , which should contribute to a phase error of less than 10% in theory [47]. This phase error can be measured by the calibration process in section 4.2, and was confirmed to be less than 5% on C-Mod.

### **3.2.5 Copper Mesh Beam Splitter**

For a double pass polarimetry system, beam-splitters are required to pickoff the laser beam reflected back by the retro-reflectors, and also to split the beams into multiple chords. Since they are extensively used, it is critical to make sure that they do not alter the laser beam polarization, which would corrupt the Faraday rotation measurements.

The beam-splitters for the C-Mod system are made of self-supporting stretched copper mesh (electroformed meshes with orthogonal grids), which was successfully tested and implemented on RTP [55][58], TFTR, and MST [59]. The beam splitters are mounted at a  $45^\circ$  angle of incidence. In Figure 3-13, the transmissions through the beam-splitters with several line densities for both horizontal and vertical polarizations are plotted. The beam-splitter is rotated in its holder to sweep out the curves shown. A mesh spacing of 400 lines-per-inch (LPI) was finally chosen for most of the beam-splitters in the system since the response was a smoothly varying function of angle and provided a nearly even split in power (40% transmission, 60% reflection) at  $45^\circ$  mesh grid angle.

Because of the asymmetry of the mesh grids, the linearly polarized light may be altered to an elliptically polarized beam after reflection from, or transmission through the mesh. This effect depends on the wire-mesh density and mesh grid orientation with respect to the polarization direction of the incident light from our tests. We can quantify the beam polarization distortion by measuring the laser power component with an orthogonal polarization relative to the incident beam. Orthogonal components for horizontally-polarized or vertically-polarized incident light, when transmitted or reflected by a 400 LPI mesh, are shown in Figure 3-14. When the mesh grid angle is around 45°-50°, the orthogonal components for both the reflected and transmission beam are small. This measurement proves that mounting the beam-splitter around a 45° mesh grid angle is important to maintain the linear polarization of the incident light, which agrees with the calibration results in section 4.2.

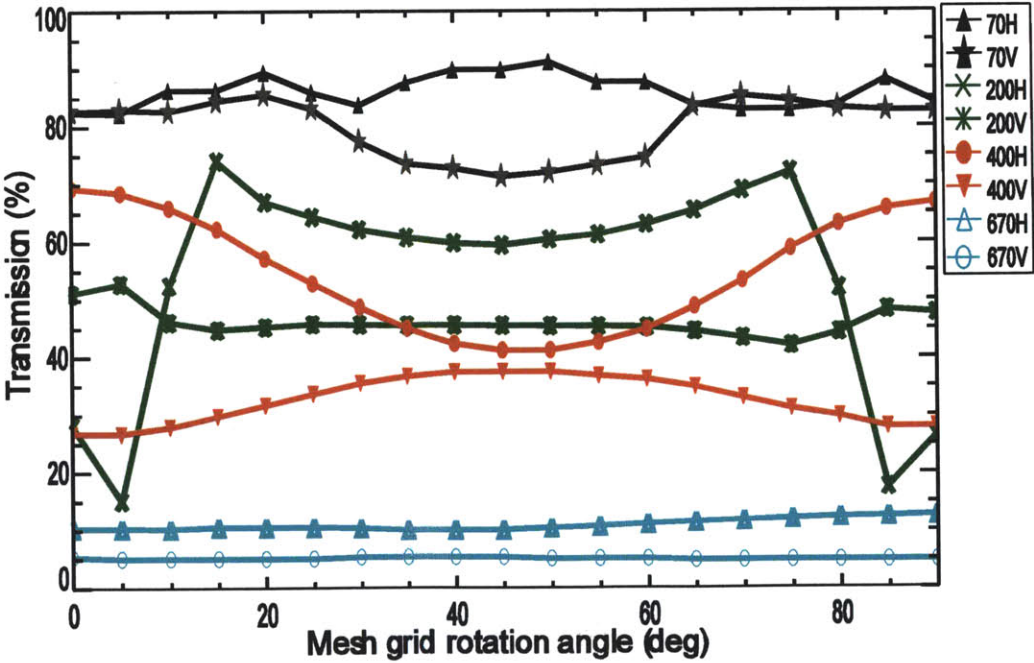


Figure 3-13: Mesh transmission for different mesh spacings and two linearly polarized incident beams (H: horizontal polarized incident beam, V: vertical polarized incident beam). The number, such as 70, specifies the lines-per-inch(LPI) for the mesh. The mesh is mounted at a 45° angle of incident, and is rotated over 90° in the holder to sweep out the curve.

Z-cut quartz plate is also a good choice for beam-splitters. They have been implemented on some other machines, such as JET [41] and RFX-mod [60]. It makes the beam alignment easier, because of its transparency to the visible alignment laser. The negative side is the beam power loss from quartz absorption, especially in a double pass system where beam-splitters are extensively used.

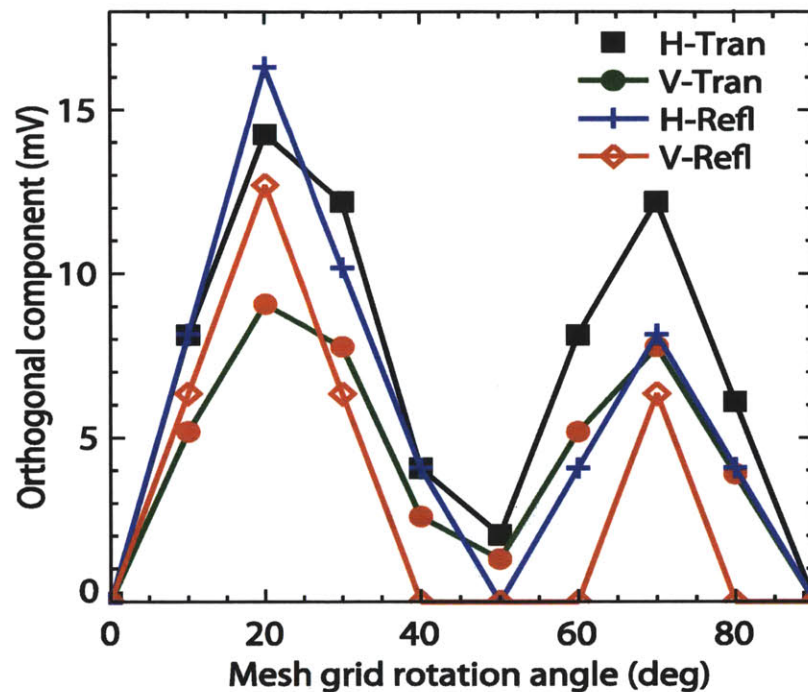


Figure 3-14: Transmitted orthogonal component for horizontal (square) and vertical (circle) polarized incident beam; reflected orthogonal component for horizontal (plus) and vertical (diamond) polarized incident beam.

High resistivity silicon is another potential material for a beam-splitter. It was tested on C-Mod, to combine the FIR and HeNe beam and picked off ~5% of FIR beam power as a reference at the same time. One problem for the thin (~100  $\mu\text{m}$ ) silicon plate we tested is that the beam transmission varies at different parts of the plate, because of thickness non-uniformity.

Higher quality silicon plates are needed to avoid this problem. Silicon beam-splitters have also been tested in the development of ITER poloidal polarimeter in Japan [61].

### **3.2.6 Focusing Elements**

The FIR laser beam needs to be focused down to a 13 mm diameter retro-reflector over a 3 m path for each chord. Some options for doing this operation include a spherical mirror, an off-axis parabolic mirror, or a TPX lens, all of which have pros and cons for the application.

The spherical mirror is cheap, and has negligible power loss comparing with lens. A major disadvantage is that it requires a small incident angle, which complicates the beam path design, and increases the path length and beam size.

Each off-axis parabolic mirror has a pre-defined off-axis incident angle, so there is no requirement for a small angle of incident. However, a big disadvantage is that they costs five to ten thousand dollars each and takes months to get a custom product with the required focal length and off-axis angle. Even worse is that a given mirror only works for a specific off-axis angle, which means we would need parabolic mirrors with various parameters for different chord geometries. This would significantly restrict options for future system upgrades.

With lenses for the focusing optics, the cost is much lower and it is easier to design a compact optical system, since they easily fit into the beamline. The main disadvantage is the power loss, which depends on the lens thickness. One lens is used for each polarimeter chord, which results in a ~20% power loss. The lenses are of a plano-convex design with a 3.0 m focal length, made of uncoated TPX. Each lens is tilted by a small angle to eliminate spurious reflections.

### **3.2.7 Retro-reflectors and Protecting Shutter**

The retro-reflectors used in C-Mod are commercially available, fabricated from a glass substrate, contained in a stainless steel cylindrical housing with a 13 mm clear aperture (Figure

3-15(a)). The mirror surfaces are coated with gold to enhance reflectivity in the FIR. The retro-reflector has been tested with no obvious reduction on reflectivity of FIR laser power during a whole run campaign in C-Mod. However, visible damage to the mirror surfaces has been observed on some of the retro-reflectors which would almost certainly affect reflectivity at shorter wavelengths (visible to IR). A molybdenum retro-reflector shown in Figure 3-15(b) is under development, but has yet to be tested during plasma operation. It is likely that a metal retro-reflector will be even more robust than glass against surface damage from plasma.

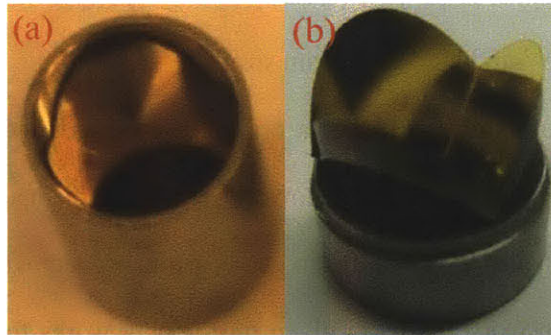


**Figure 3-15: (a) Glass retro-reflector with gold coating (b) Prototype molybdenum retro-reflector with gold coating**

The retro-reflectors are installed on the inner wall, where they can be exposed to high heat flux and possible plasma/neutral sputtering during plasma operation. To protect the retro-reflectors from this harsh environment, particularly during inner wall limited discharges and boronizations, a shutter assembly, shown in Figure 3-16, was designed to hold the retro-reflectors and can be closed to isolate the retro-reflectors when required. The shutter itself is mounted on the inner wall and protected by molybdenum tiles on either side and across the plasma facing surface. Two bellows that can be alternately pressurized with helium or evacuated, provide a push-pull mechanism that opens or closes the shutter. Plasma facing and inner wall facing views

of the shutter are shown in Figure 3-17. The protection tiles and bellows can be seen in these views.

In Figure 3-17, a picture of the inner wall is shown in which the openings for the retro-reflectors can be seen. The six retro-reflectors are spaced along the inner wall from 4 to 39 cm above the machine mid-plane. Each retro-reflector has a specific viewing angle, which correlates with the designed incident laser beam.

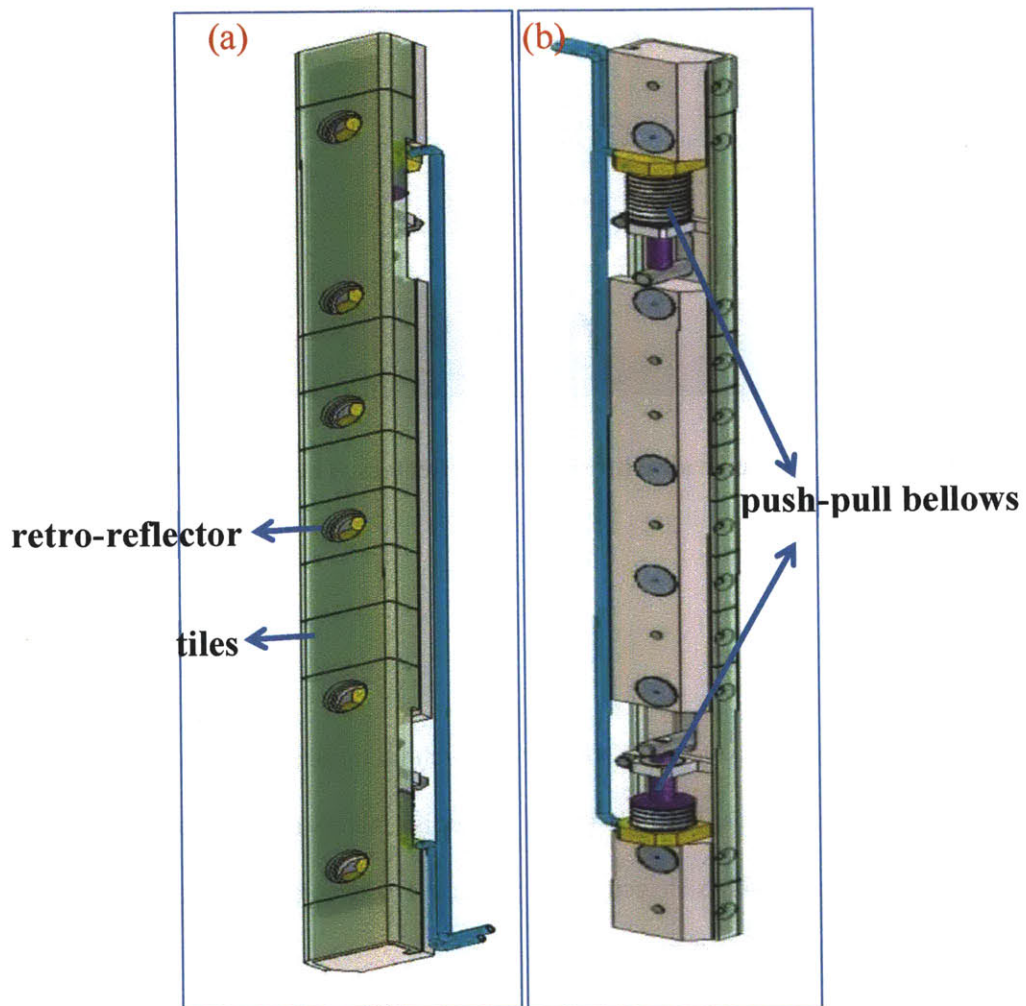


**Figure 3-16: (a) Plasma facing side of the shutter assembly showing protection tiles and location of the retro-reflectors (b) Inner wall side of the shutter assembly showing the push-pull bellows.**

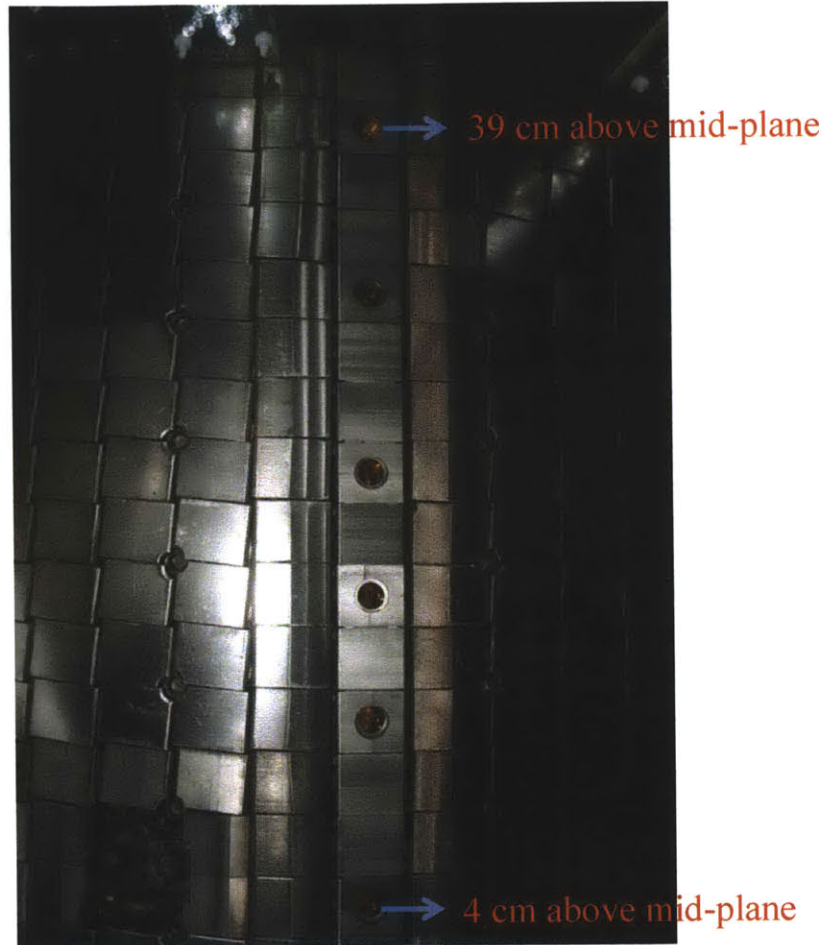


**Figure 3-17: C-Mod inner wall with six retro-reflectors. The shutter is open, and we can see all six retro-reflectors.**

### 3.2.8 Mixers

To achieve high signal-noise-ratio (SNR) for multi-chord measurements with a total of  $\sim 300$  mW power from FIR lasers, it is desirable to use low-noise mixers in the polarimetry system. Liquid helium cooled InSb or GaAs detectors, pyro-electric detectors or corner-cube Schottky diode detectors all can be used as mixers.

Liquid helium cooled InSb or GaAs mixers have low noise levels, and have been used on polarimetry systems of other machines, including TCV [62] and JT-60U [61]. However, these

mixers require large cryostats to keep them cool, and are not convenient for a multi-chord, compact system design.

Pyroelectric mixers were used for the first generation of the polarimetry system on TEXTOR using the amplitude measurement technique [33], as described in chapter 1. Pyroelectric mixers have a relatively poor noise-equivalent-power, especially at high IF frequencies. They are not suitable for use at high IF frequencies, needed for the fluctuation measurements in C-Mod. However, they are very useful in measuring the location of the laser beams and measuring the laser beam profile, since they have a large clear aperture and are not sensitive to the beam coupling angle or beam shape.

Schottky diode based mixers have been used on most of the FIR interferometry/polarimetry systems in the world, because of their good SNR, high frequency response, and compact size. Four different kinds of mixers have been tested in C-Mod, shown in Figure 3-18, including commercially available Farran Corner-cube mixers (optimal operation for 100-150  $\mu\text{m}$  wavelength) [63], corner-cube mixers on loan from UCLA (optimized for wavelength of 180  $\mu\text{m}$ ), a waveguide coupled mixer from Radiometer-Physics, and planar diode mixers, which were specifically developed for C-Mod polarimetry by Virginia Diode Inc (VDI). A main disadvantage for Schottky diode mixers is that it is extremely sensitive to electrostatic damage. A couple of Farran and UCLA mixers were actually damaged during the test process. A disadvantage of the corner-cube mixer is that it has high reflectivity for FIR laser beams, and thus could potentially cause cross-talk problem between different mixers. The corner-cube mixers also use very fragile, with whisker contacts that often fail and must be repaired. The new planar Schottky diode mixer is more robust than the corner-cube mixers, as it does not have whisker contacts, but instead the diode is part of the etched chips substrate, visible in Figure 3-19(a). FIR power is coupled to the diode through a pyramidal horn, shown in Figure 3-19(b), and a WR-0.4 waveguide. The optimal beam waist at the horn is 0.27 mm.

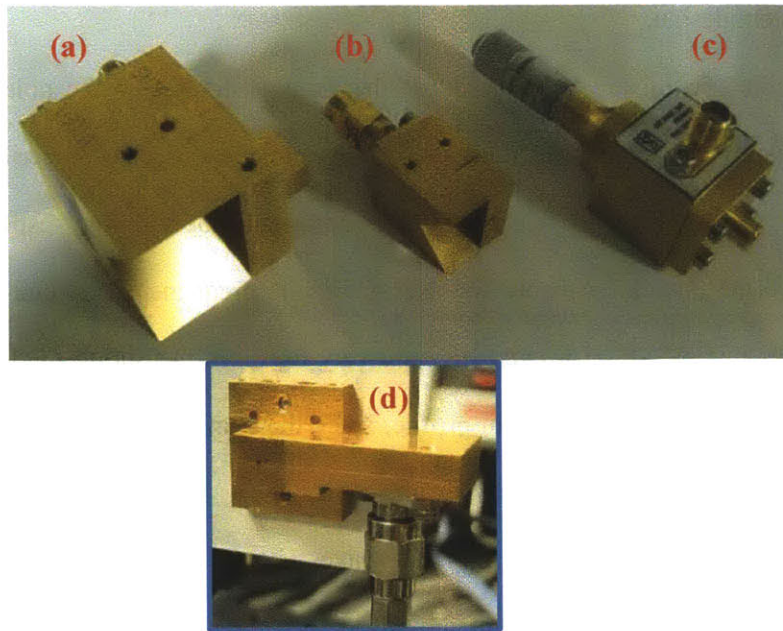


Figure 3-18: Figure 3-18: Four mixers tested. (a) Farran Corner-cube Mixer (optimal operation for 100-150  $\mu\text{m}$ ) (b) Corner-cube Mixer for 180  $\mu\text{m}$  (loan from UCLA) (c) Waveguide coupling mixer from Radiometer-Physics (d) Planar diode mixer (developed by VDI for our wavelength at 117.73  $\mu\text{m}$ )

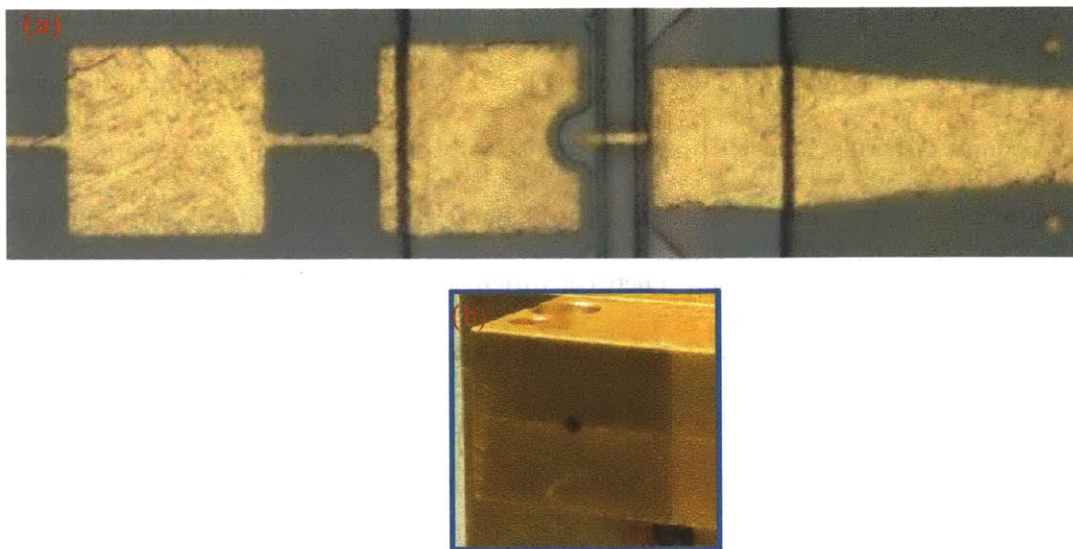


Figure 3-19: (a) Micrograph of the planar Schottky diode and a portion of the coupling structure (b) Pyramidal horn where FIR power couples through

The pros and cons for each mixer have been listed in Table 3-3 for convenient comparisons. The newly developed planar diode mixer is considered to be the best choice, and has been used for the experimental measurements on C-Mod.

The planar diode mixers are insensitive to the polarization of the incident beam: the responses of the two mixer axes are about 1:5. Polarizers are therefore necessary in front of the detectors, to improve the response of the pyramidal horns. The polarizers used are free-standing 10  $\mu\text{m}$  diameter tungsten wires spaced 25  $\mu\text{m}$  apart. They exhibit a very good extinction ratio (less than 0.1% leakage) and are used in front of all the mixers to select the polarization component desired for the measurement (i.e., polarization orientation parallel to the toroidal magnetic field). They are very low loss components.

The output signal levels from the mixers are in the mV range, and amplifiers with bandpass filters centered at 4 MHz, with a 1 or 2 MHz bandwidth, are used to filter the signals.

**Table 3-3: Comparisons of four Schottky diode mixers**

<b>Different FIR mixers</b>	<b>Size</b>	<b>Optimized for <math>\lambda=117.73 \mu\text{m}</math></b>	<b>Responsivity (V/W)</b>	<b>Easy to damage</b>	<b>Optical Feedback</b>
Corner-cube (Farran)	Large	Yes	15	Yes	Yes
Corner-cube (UCLA)	Small	No	NA	Yes	Yes
Waveguide coupling	Medium	No	NA	Yes	No
Planar diode (VDI)	Small	Yes	~400	No	No

### **3.3 Phase Analysis**

#### **3.3.1 Digital Phase Comparator**

The probe and reference signals are digitized at 20MHz, well above the bandpass Nyquist frequency, so that the needed phase information can be obtained using a fully digital process [64].

Digital phase difference analysis offers the advantage of fast time resolution without complex analog comparators and eliminates the errors introduced by amplitude variation in the signals. Both the reference and probe channels are sinusoidal signals oscillating at the IF, set and controlled with feedback to ~4 MHz. To obtain the phase difference between the probe signals and reference, all channels must be digitally preprocessed. The reference channel can be expressed in a discrete form as

$$r(n) = A(n) \cos[\omega_{IF}n\Delta t + \theta_r(n)], n=0,1,2,\dots,N-1 \quad (3.5)$$

where  $N$  is the data array length, and  $\Delta t$  is the sampling interval. Through Discrete Fourier transformed (DFT), Equation 3.5 is transferred into frequency space

$$R(\omega_{IF}) = \frac{1}{N} \sum_{n=0}^{N-1} r(n)e^{-i\omega n\Delta t} \quad (3.6)$$

It is then digitally filtered to remove the equilibrium component and negative frequencies ( $n \geq N/2$  terms),

$$R'(\omega_{IF}) = \frac{1}{N} \sum_{n=0}^{\frac{N}{2}-1} r(n)e^{-i\omega n\Delta t} \quad (3.7)$$

and is transformed back to the time domain

$$r'(n) = A'(n) \exp\{i[\omega_{IF}n\Delta t + \theta_r(n)]\} \quad (3.8)$$

Similarly, the probe signals can also be transformed to the complex time domain signal

$$s'(n) = B'(n) \exp\{i[\omega_{IF}n\Delta t + \theta_s(n)]\} \quad (3.9)$$

The conjugated reference and a probe signal are multiplied together, generating a complex signal,  $\psi$ .

$$\psi(n) = s'(n)r'^*(n) = C'(n) \exp i[\theta_s(n) - \theta_r(n)] \quad (3.10)$$

The phase difference between the probe and reference signal is then just  $\tan^{-1}[\text{Im}(\psi)/\text{Re}(\psi)]$ . Note that in this process the amplitude dependence is removed. Finally, the Faraday effect is 1/2 of the measured phase change when using the R-, L-wave technique, which was discussed in chapter 2.

### 3.3.2 Analog Phase Comparator

In order to do digital phase comparison, both the reference and probe signals have to be digitized and stored into the database before we can run our digital phase comparator to generate the phase difference. As the signals are digitized at a 20 MHz sampling rate for 2-3 seconds on C-Mod, it takes several minutes to store the data and calculate the Faraday rotation. Therefore, the analog phase comparator has an advantage, if we want to see the Faraday rotation immediately after a plasma discharge, or if we want to use Faraday rotation signal to feedback control the plasma current. The analog phase comparator is also used when we are diagnosing the system vibration noise level. We can observe the Faraday rotation error on the oscilloscope, while introducing vibration noise in the system by tapping the optical components or using a speaker to acoustically drive known resonant frequencies.

For the analog phase comparator, an XOR circuit was developed to compare the phase between two sinusoidal input signals. A comparator converts both signals into square waves, and then feeds the signals into an XOR gate. The XOR output, after filtering, is a voltage proportional to the phase difference between the two signals. By driving the circuit using two signal generators offset slightly in frequency, a plot of phase difference verses XOR output voltage can be produced, which is used to calibrate the XOR output with the phase difference between input signals.

To confirm that the phase from the XOR circuit is the same as the digital phase, the Faraday rotation for a plasma discharge from the XOR circuit (red curve in top trace) and the digital phase comparator (black curve in top trace) are plotted together in Figure 3-20. We can see

these two phase signals overlap during the whole plasma discharge as expected, and the difference is at the noise level of the measurement.

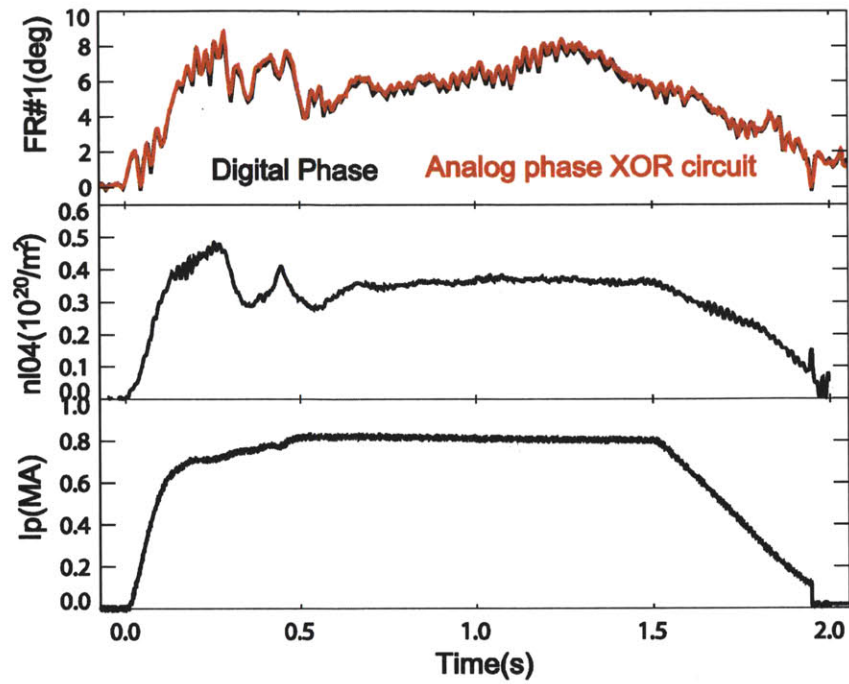


Figure 3-20: Faraday rotation from both digital and analog comparators for shot 1110113010. Analog phase from the XOR circuit agrees perfectly with the digital phase.

## 4. Polarimetry Noise Improvements and Performance Analysis

We need to reduce the noise level for the polarimetry system to an acceptable level ( $\sim 0.1^\circ$ ), and make sure the system is indeed sensitive to the plasma parameters we want to measure, in order to effectively measure the current density profile changes during LHCD experiments (chapter 5) and to measure fluctuations (chapter 6) ,

After successfully testing the polarimetry system in the lab with a long beam path and no plasma, the system was installed on C-Mod. A single chord polarimeter, serving as a proto-type of the multi-chord diagnostic system, was made operational during the 2010 C-Mod campaign. This system was upgraded to a 3-chord measurement during the 2012 C-Mod campaign. There was very good progress in understanding and improving the measurement noise during the system development. Several difficulties were encountered and resolved during the development process, as described in this chapter. These experiences have already contributed to the polarimetry development on J-TEXT [30] and EAST, both of which have picked the same FIR lasers (Coherent Inc.) and the detectors (VDI) as used in our system. Our experience on systematic error reduction for mesh beam-splitters contributes to similar experiments on DIII-D [31][36]. The experience on C-Mod should also be a valuable resource in developing a poloidally-viewing polarimetry system on ITER, as it is designed with the same wavelength (118  $\mu\text{m}$ ) and similar viewing geometry [65][66].

In section 4.1, we will review the noise induced by multiple factors in the Faraday rotation measurements, including vibrations, IF stability, co-linearity errors, spurious reflections, and stray magnetic fields. Various methods have been implemented to mitigate different source of noises.

In section 4.2, we will discuss the systematic error from the asymmetric mesh beam-splitters. This phase error is quantified and reduced with a calibration technique using a rotating half-waveplate.

The measured Faraday rotation is proportional to the integral of the electron density and magnetic field along the beam-path. To confirm the polarimeter sensitivity to these plasma parameters, we evaluate the Faraday rotation performance during density, current or plasma position scans, as described in section 4.3. Since the C-Mod polarimeter has a time resolution of  $\sim 1 \mu\text{s}$ , it is also fast enough to capture the dynamics of plasma parameter changes during sawtooth crashes. All three chords respond to the sawtooth crashes, and these measurements have the potential for measuring current density profile changes during the crash.

## **4.1 Noise Improvements**

### **4.1.1 Acoustic Noise**

Our FIR lasers are sensitive to acoustic noise, with major resonances around 220 Hz and 330 Hz, which also appear on the measured Faraday rotation signals. 10 cm of acoustic foam, which attenuates the sound wave passing through by approximately a factor of 100, are attached to the enclosure panels, at the top of the enclosures and around the laser magnetic shielding box, to damp the acoustic noise in the polarimetry system (white pieces in Figure 3-6 and Figure 3-7).

To evaluate the phase errors due to acoustic noise, we acquired Faraday rotation measurements without plasma (zero phase change in theory) for the single chord system. The phases were monitored for 20 seconds, as shown in Figure 4-1. About  $\pm 0.3^\circ$  Faraday rotation drift was observed, when a panel was taken off the enclosure (black curve). When the enclosure was fully closed (red curve), the Faraday rotation signal had less than  $0.1^\circ$  phase error. The sound damping also effectively reduces sound vibration induced high frequency phase noise, which could mask small amplitude phase changes due to plasma fluctuations. Therefore, to achieve low noise and low phase error for both the equilibrium and fluctuation measurements, it is important to get the polarimetry system well shielded from the very noisy acoustic environment in C-Mod cell.

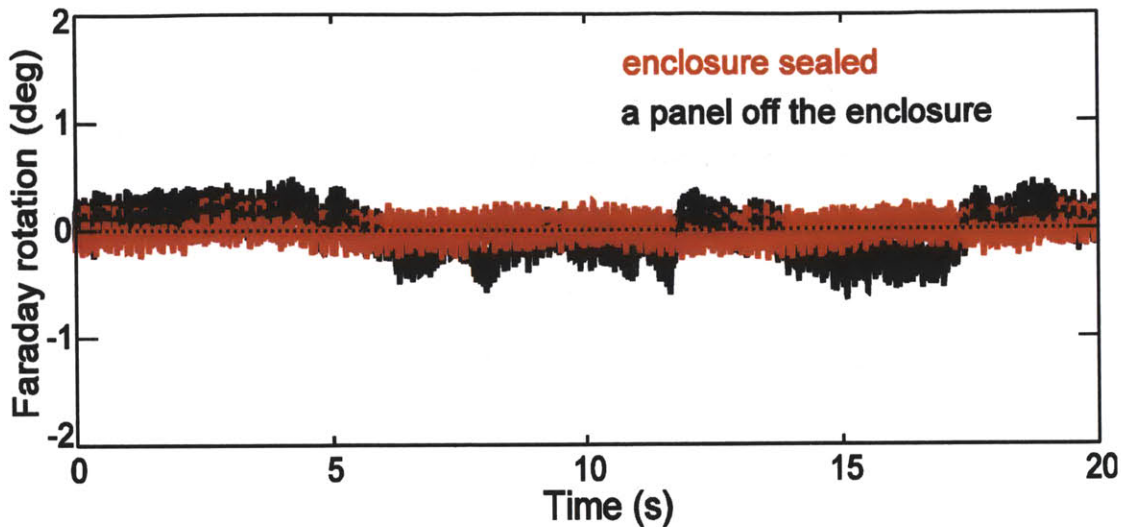


Figure 4-1:  $\pm 0.3^\circ$  Faraday rotation phase error when a panel is off the enclosure (black curve). Smaller phase error with the enclosure closed (red curve).

#### 4.1.2 Mechanical Vibration Noise

With the lower optical table sitting on the solid C-Mod cell floor ( $\pm 25 \mu\text{m}$  movement during discharges as determined by accelerometer measurements), and the upper optical table rigidly attached to the igloo (60 cm thick concrete blocks and very stable) that surrounds the tokamak, the vibrations of the optical tables can be reduced to a low level. However, the laser cavities have connections to the laser gas lines, RF cables and pumping lines, all of which may transfer vibrations to the lasers (our tests show that this is especially true for the pumping lines). To reduce the laser vibration, the pumping lines were changed from stainless steel bellows to Teflon lines, which are soft and effectively isolate the vibrations. Since the lasers, detectors and retro-reflectors are not located on a single table (Figure 3-2), the relative movement of the tables could cause extra measurement error. Therefore, it is important to make sure the optical tables themselves do not move during the plasma discharge. Three heavy metal beams and turnbuckle

hardware, connecting the upper table to the igloo, provide additional mechanical support (one of these components is shown in Figure 3-7).

Both longitudinal and transverse vibrations may cause phase error in measuring the Faraday rotation effect. The polarimeter is not as sensitive to longitudinal vibrations as is the interferometer. Since we are measuring the phase change of an envelope with a wavelength of 75 m ( $\lambda_{envelope} = c/IF$  where  $IF=4$  MHz), a parallel path-length change of about 1 cm would be required in a double pass system to cause a  $0.1^\circ$  change in phase. Independent interferometric measurements of the C-Mod inner wall, where the retro-reflectors are mounted, with a HeNe laser indicate longitudinal movement on the order of  $100 \mu\text{m}$  is to be expected. So the changes in longitudinal path-length will not cause detectable errors in the Faraday rotation signals.

Transverse vibration, which allows two laser beams to diverge from perfect co-axial alignment, can cause much bigger phase errors. In this case, the important length is the laser wavelength, and maintaining a phase measurement error below  $0.1^\circ$  requires that the angular deviation between two beams be less than

$$\theta = \frac{0.1^\circ \times \lambda_{laser}}{365^\circ \times L_{path}} \quad (4.1)$$

where  $\lambda_{laser} = 117.73 \mu\text{m}$  and the beam path-length  $L_{path} \approx 14\text{m}$ . Thus  $\theta \approx 3 \text{ nRad}$ . Since the beam is focused down into the mixer, the phase measurement might be less sensitivity to the vibration than found from this calculation.

Rigid mirror and laser mounts are essential to keep the vibration phase noise down to a reasonable range. To achieve a solid and compact design, custom optical mounts were designed for most of the optics on the upper vertical table, including the waveplates, TPX lenses, beam-splitters and polarizers. These mounts are constructed from half inch aluminum plate and are designed specifically for rigidity by incorporating gussets to keep the plane of the optical components fixed.

### 4.1.3 IF Stabilization

Since the frequency for each laser drifts with time, especially during a plasma discharge, the IF can shift in frequency. As discussed in section 3.2.2, the IF can be feedback controlled, so its frequency shift is normally less than  $\pm 10$  kHz, and may increase to  $\pm 40$  kHz during the plasma discharges. The stability of the IF also affects the Faraday rotation measurement. The phase noise caused by a change in IF,  $\Delta f$ , is

$$\Delta\alpha = 2\pi\frac{\Delta f}{c}(L_{pb} - L_{ref}) \quad (4.2)$$

where  $L_{pb}$  and  $L_{ref}$  are the path-length for the probe and reference detectors.  $\Delta L = L_{pb} - L_{ref}$  is  $\sim 6$  m in our three-chord system, leading to  $\Delta\alpha \approx \pm 0.05^\circ$  for an  $\pm 40$  kHz shift in  $\Delta f$  of our system. This noise level likely reflects the minimum attainable with the current optical path layout. In future system upgrade,  $\Delta L$  should be minimized to less than 1 m, to reduce even further the phase errors from the shifts in IF.

### 4.1.4 Laser Beam Co-linearity

To realize Faraday rotation measurement with the Dodel-Kunz method, the L- and R- circularly polarized beams need to be well co-aligned with each other. Small misalignment between the two beams may cause a big phase error, since each beam will see different vibrations along its beam-path. An even more serious problem is that two beams will see different parts of the plasma due to the beam offset. Perfectly collinear L- and R- beams see the same interferometric phase shift with a second order difference from the Faraday rotation effect, so the interferometric effects are cancelled out and the phase difference between the two beams will only show the much smaller Faraday rotation effect. When L- and R- beams are not collinear, their phase difference will show a significant systematic error from different interferometric phase shift. A 0.1 mm offset between two beams may result in  $0.1^\circ$  error for a single pass polarimetry system, as seen on other machines [67].

The phase error from the parallel offset between L- and R- beams may not be significant for C-Mod polarimetry, because of the double path geometry. Two beams will switch position after being reflected by the retro-reflector. Therefore, the double pass interferometric effects would be the same for L- and R- beams, even when there is some offset between them.

It is difficult to reduce the beam alignment error with methods that depend largely on by-eye observations. On C-Mod, two laser beams are carefully co-aligned to an accuracy of below 1 mm by measurements with a 2-D pyroelectric camera and thermal crystal sheets. A rotating dielectric wedge method has been developed for the MST polarimeter system, which increases the accuracy of the beam alignment [68]. This method could be used for the C-Mod polarimetry alignment in the future.

#### **4.1.5 Spurious Reflections**

Spurious reflections in the polarimetry system can cause a large phase error in the Faraday rotation measurements. Several sources of spurious reflections have been identified and then largely eliminated in the C-Mod polarimeter system.

One spurious reflection source is from the beam-splitters. Six beam-splitters are needed on the upper table to divide the beam and pick off the returning beam. In cases where only half of the beam power is used, the other half needs to be carefully dumped onto FIR absorption materials, so that it will not be reflected back into the system. The absorption materials are carefully aligned to minimize the phase noise on the detectors. Sawtooth structures are machined on their surface, which enhances the absorption efficiency.

A second source of spurious reflections is from the corner-cube retro-reflectors on the inner wall. The laser beam can be reflected all the way back into the laser source, which may affect the laser stability, and the reflected beam may get back into the polarimetry system again by reflection off the laser output coupler. This spurious reflection should have less than 1% the

power of the original beam, considering the power loss on the extra beam pass. This source of phase error has been found to be less than the error from other sources.

Corner-cube mixers (Figure 3-18 (a)) can also cause reflection problems, since the design naturally sends any undetected light back into the optical path. Detectors set up on opposite legs of a beam-splitter result in easily detectable phase error caused by this crosstalk. Therefore, a separate beam-splitter has been used to pick off a fraction of the beam to create a reference signal, rather than sharing a single beam-splitter with another detector. Also, the new planar diode detector (Figure 3-18 (b)) uses a horn coupling geometry instead of a corner-cube, which should greatly reduce beam reflection off the detector, if the detector is aligned with a small tilt angle.

Another spurious source is the reflection from the quartz vacuum window. If the incident beam is nearly perpendicular to the window, there would be a small fraction of the beam reflected back to the system and the false signal on the probe detector can be large even when the shutter to protect the retro-reflector is closed (no returning beam from the retro-reflector). For the six poloidal-viewing chords on C-Mod, we only observed reflections from the vacuum window on chord#3. Realignment by 2 cm of the turning mirror that directed the laser beam through the window eliminated this problem. In the planned upgrade to 6 chords, a separate window would be provided for each chord. In this case each vacuum window would be installed with a small tilt angle relative to the incident beams, to prevent window reflection issues. An added advantage to using separate windows is the ability to design the window as an etalon, with minimal losses and reflections.

One way to estimate the phase error from spurious reflection is to monitor the signal amplitude and noise level on the reference detector when the shutter to the retro-reflectors is alternatively opened and closed. Another way is to check if the signal on any chord changes while blocking any other chord. If no change of the detector signal results, this indicates that the phase error from spurious reflections is negligible compared with other noise sources.

#### 4.1.6 TF Ramp-Induced Error

A slow drift in phase, of about  $1^\circ\sim 2^\circ$ , can occur during toroidal magnetic field (TF) ramps, when there is no plasma, and the Faraday rotation should be zero. A series of no-plasma tests for each C-Mod magnet revealed that the Faraday rotation measurement is mainly affected by ramps in TF field, and not the poloidal fields. For a TF-only test shot, shown in Figure 4-2, the red curve shows the time history of the toroidal field, which ramps up to 5.4 T between -1s and 0 s, and then ramps back down between 1.1 and 2.7 s. The apparent Faraday rotation on chord#1 (black curve) shows a  $\sim 0.5^\circ$  slow drift during the TF ramps, but is close to zero during the TF flattop, indicating this error is sensitive to the magnetic field change (dB/dt) but not the magnetic field itself. The Faraday rotation phase error during the poloidal field coil tests is negligible.

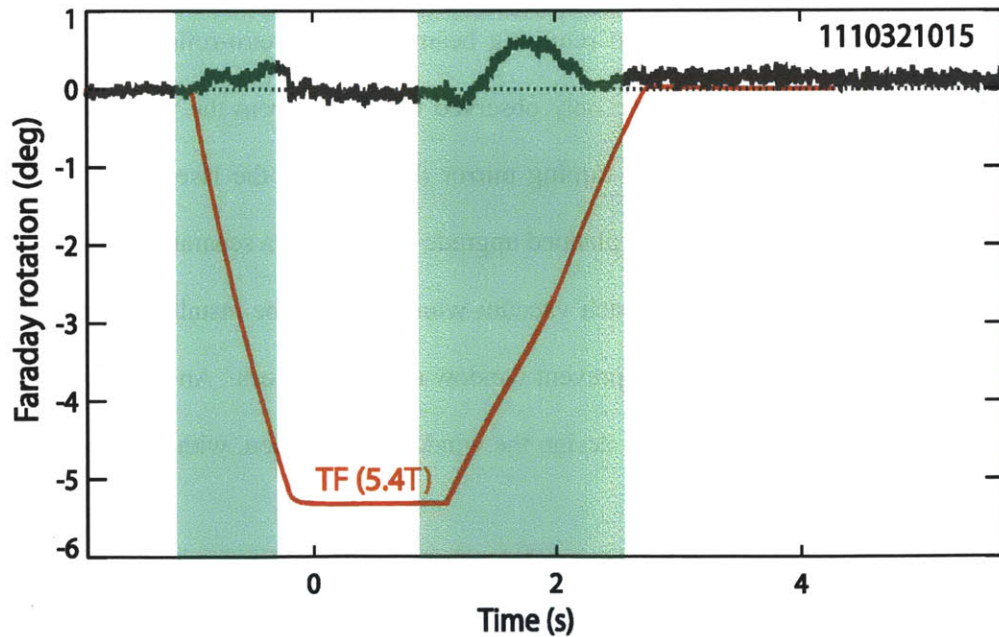


Figure 4-2: TF-only test shot. The Faraday rotation has a  $\sim 0.5^\circ$  slow drift during the TF ramps, but it is close to zero during the TF flattop, indicating the phase error is sensitive to the magnetic field change, but not the magnetic field itself.

With a phase drift right before the discharge caused by the TF ramp, it is difficult to define the zero baseline for the Faraday rotation measurement during a plasma discharge. However, to live with the TF ramp noise, we can obtain a short period of flat baseline right before the plasma, by adjusting the toroidal field starting time 0.1 s earlier than usual. In Figure 4-3, Faraday rotation signals (1120614012) for all three chords have flat baselines from -0.2 to 0 s. The shadow region has been expanded and shown as the blue curves in Figure 4-4. Baselines for another two discharges (1120612002, 1120626012) with different times to reach the TF flattop ( $t_{TF}$ ) are shown as black and red curves. Flat baselines are achieved when the  $t_{TF}$  is earlier than -0.2 s.

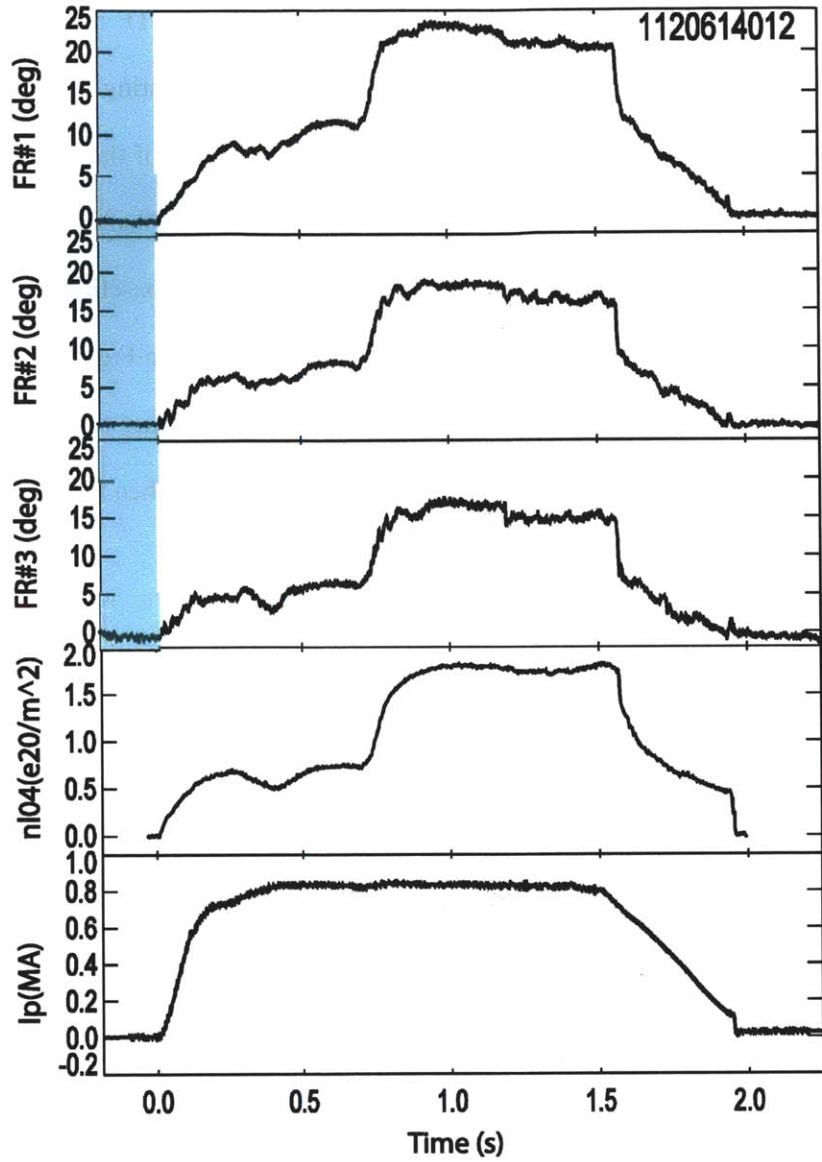


Figure 4-3: Three-chord measurements with improved baselines before the plasma (-0.2 to 0 s), by adjusting the TF ramp starting time 0.1 s earlier than usual. The shadowed area is expanded and compared with another shot with noisy baselines in Figure 4-4.

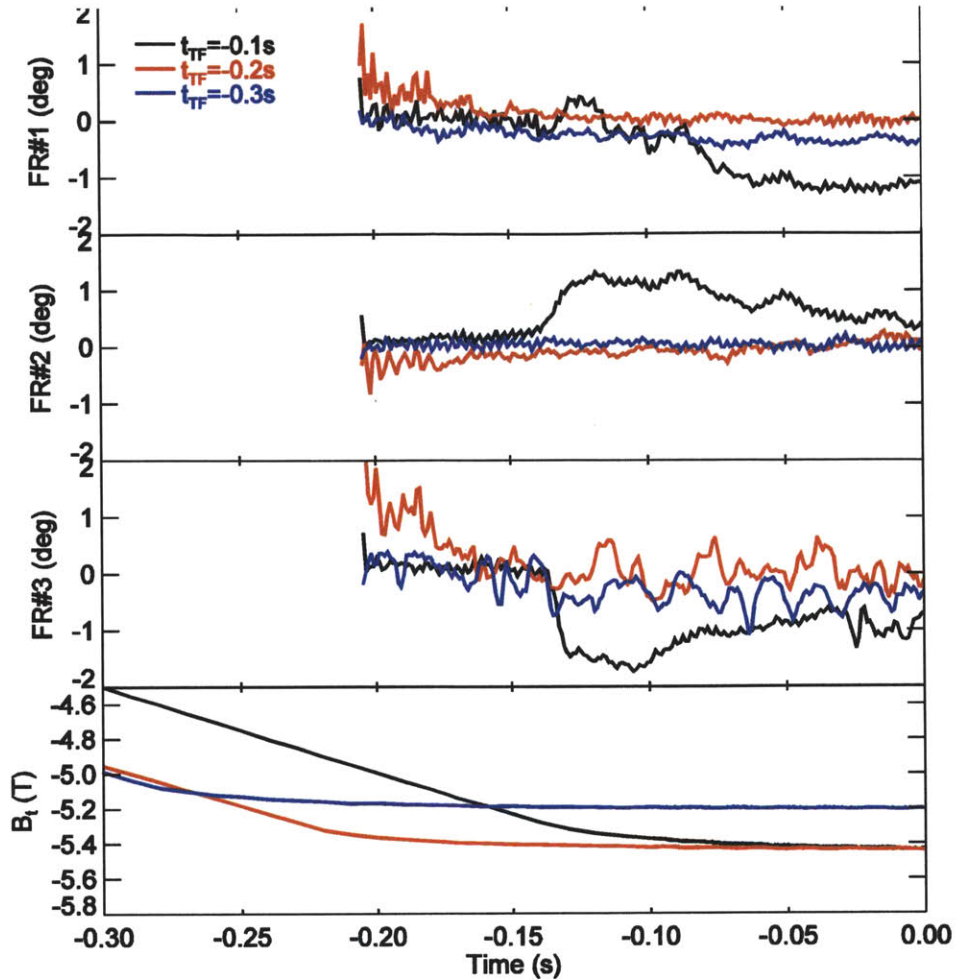


Figure 4-4: Baseline comparison for three discharges with normal TF ramp (black curve) and adjusted TF ramp (red and blue curves). For the adjusted cases, the TF ramp-up starts 0.1 seconds earlier than normal, so that flat-top is reached by  $t \approx -0.2$  s for the red shot and by  $t \approx -0.3$  s for the blue shot. (Polarimeter only records signals from -0.2 to 2.2 s at 20 MHz, due to the limitation of the digitizer memory)

#### 4.1.7 TF Effect

The high toroidal field of C-Mod carries with it two concerns. One concern is that if the laser beam-path differs from 90 degrees to the toroidal field direction by an angle  $\delta$ , the toroidal magnetic field will have a non-zero projection on the polarimetry beam-path, which will produce a Faraday rotation error. The measured Faraday effect is

$$\alpha = C_f \lambda^2 \int n_e \mathbf{B} \cdot d\mathbf{l} = C_f \lambda^2 \left( \int n_e B_p \cos\delta dl + \int n_e B_t \sin\delta dl \right) \quad (4.3)$$

where  $C_f \lambda^2 \int n_e B_t \sin\delta dl$  is the phase error from the toroidal field pick up. Assume the beam is off by  $1^\circ$  from the poloidal cross section, the resulting phase error could be a couple of degrees, which is  $\sim 20\%$  of the Faraday effect from the poloidal field we are measuring, as shown in simulations of C-Mod plasma discharges. The other concern is that the C-M effect may contaminate the Faraday rotation measurement with high toroidal field, as discussed in chapter 2.

To prove both errors are not significant on C-Mod Polarimetry, shots were taken with the same plasma current and density, while  $B_t$  was varied from 5.4 to 7.5 T, shown in Figure 4-5. For these two discharges, the measured Faraday effect (chord#1) was unchanged, indicating the beam misalignment in the toroidal direction is negligible (a  $1^\circ$  misalignment should introduce a  $\sim 10\%$  Faraday rotation disagreement between these two discharges), and the C-M effect is playing no big role in the Faraday rotation measurement in these two discharges.

## 4.2 Calibration

To measure the Faraday rotation effect with the Dodel-Kunz method, we need to launch two circularly-polarized beams into the plasma. However, optics in the polarimetry system may cause significant laser polarization changes, which may cause the circularly-polarized probe beams to become elliptically polarized, and the Faraday rotation measurements would then have large systematic errors. As shown in section 3.2.5, the mesh beam-splitters are a source of polarization distortion in our system.

To quantify and correct the systematic errors from polarization distortion, a 50 mm diameter half-wave plate, located between the off-axis parabolic focusing mirror and the probe detector is rotated by an automatic rotation stage to produce a calibrated phase shift. For circularly-polarized probe beams, the phase change should be twice that of the half-wave plate rotation angle. Measurements show that the systematic error depends on the orientation of the

mesh grid for the beam-splitters. In Figure 4-6, we rotate the beam-splitter which picks off the returning beam to the probe detector, and repeat the calibration process with different mesh grid angles. The calibration phase is almost a linear function of the half-waveplate rotation angle with an error of less than 5%, when the wires of the beam-splitter are set to 45°. The calibration phase could have a significant non-linear response, when the mesh grid of the beam-splitter is setup far away from 45°. Any deviation in linearity is then recorded and can be used to calibrate the measurements during a plasma discharge. This calibration must be checked whenever a new optical component is added to the system.

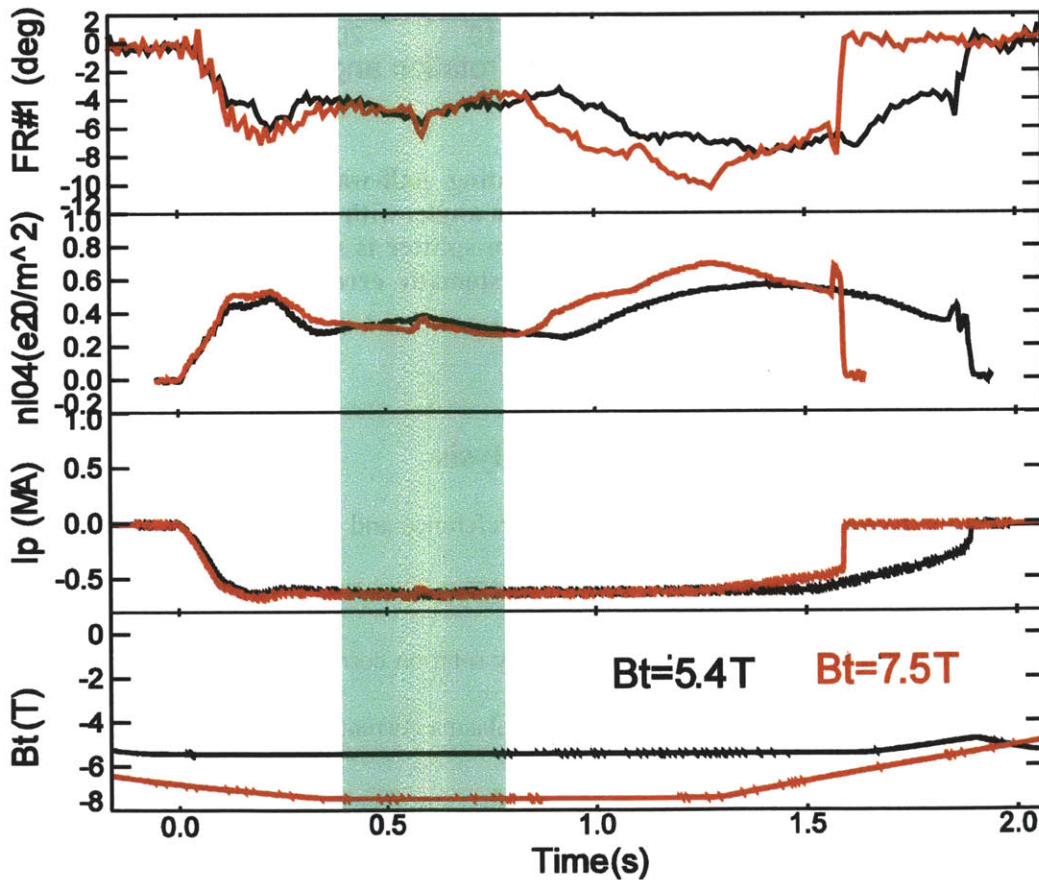


Figure 4-5: Faraday rotation signals are the same for two shots while the density and current are the same (shaded region).  $B_t=7.5$  T for the black curve, and  $B_t=5.4$  T for the red curve. No significant TF misalignment or C-M effect was observed.

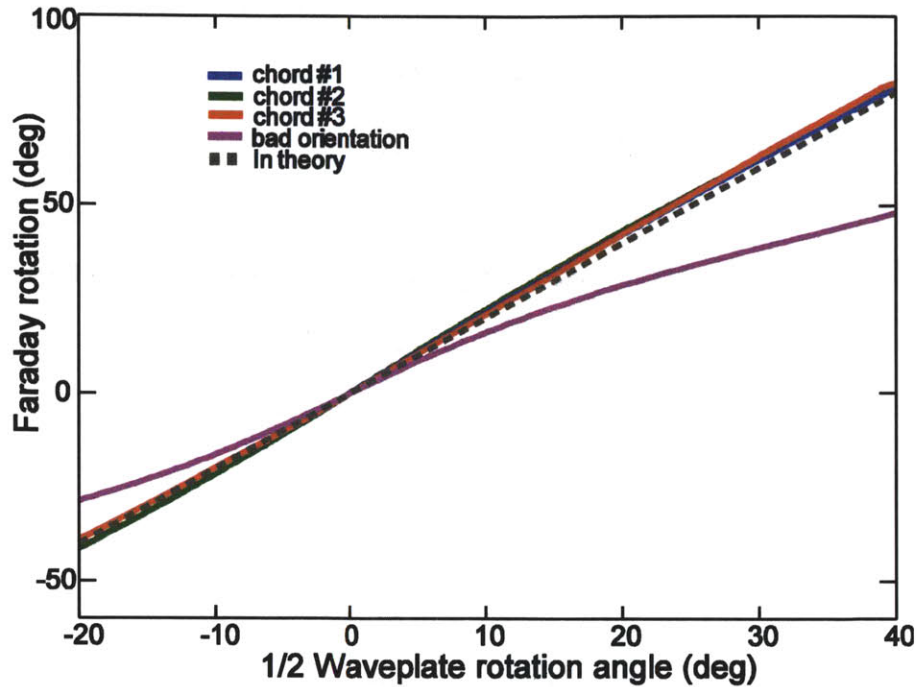


Figure 4-6: System calibration with a rotating half-waveplate. The measured phase responds linearly to the half-waveplate rotation angle, with an error of less than 5% for all three chords, when the mesh grid of the beam-splitter is set at  $45^\circ$ . The measured phase shows significant non-linearity, with large systematic error, when the mesh grid of the beam-splitter is far away from  $45^\circ$  (purple).

### 4.3 Measurement Performance Analysis

It was exciting to see the phase change between reference and probe detectors with a reasonable noise level, when the FIR polarimetry system was operational for the first time on C-Mod. Next we want to confirm we are measuring the Faraday rotation correctly, by analyzing how sensitive the Faraday effect is to electron density changes, plasma current changes, plasma position sweeps and sawtooth crashes.

#### 4.3.1 Density Sensitivity

Since Faraday rotation is proportional to the line integral of the electron density along the poloidal viewing beam path, weighted by the local magnetic field parallel to the beam-path, it

should have a strong correlation with the TCI signal, as both of them have line integrated density information. Among the three chords, the Faraday rotation for chord#1 is expected to have similar trends to the TCI density signal, since they are both heavily weighted near the core where the density is high.

In Figure 4-7, the Faraday rotation signal for chord#1 is plotted with the TCI density and plasma current for shot 1110405010. During the flat top of the plasma current, the Faraday rotation signal shows spikes, similar to density increases seen in the interferometer signal (shaded regions of the plots, between 0.6 and 0.9 s).

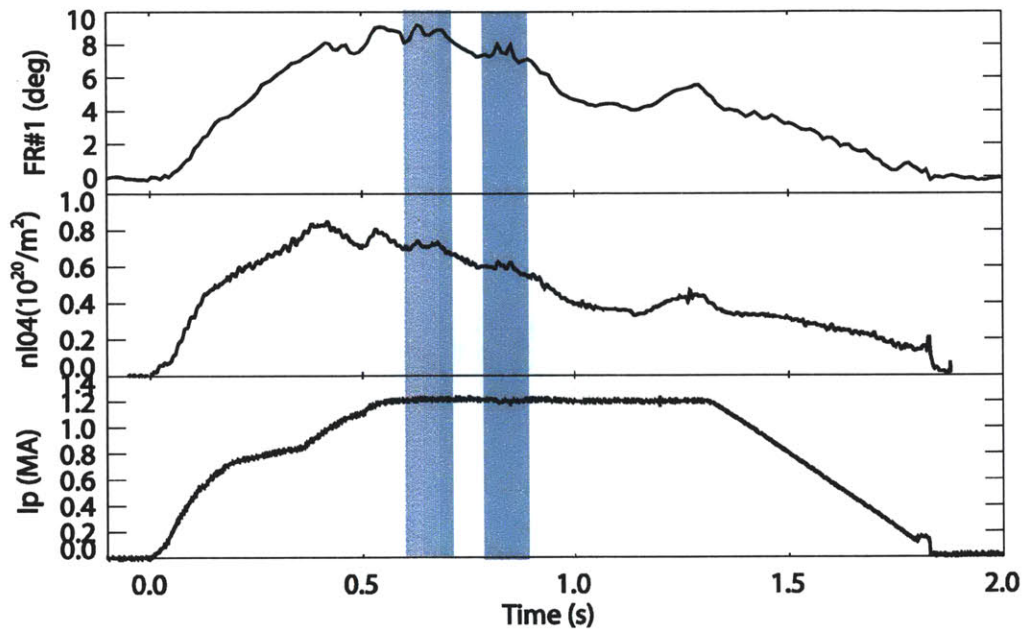


**Figure 4-7: Faraday rotation (chord#1) shows similar spikes as on the density trace, during the flat-top of the plasma current.**

For another H-mode discharge, shown in Figure 4-8, there are three H-modes that clearly show large density changes during the current flat-top. The Faraday signals from each of the three chords observe every H-mode transition with time histories similar to those seen in the line

integral density trace. FR#1 changes about 30% during the H-mode transitions, consistent with the density variation. FR#3 shows about 50% change, since it is weighted more over the edge density, which may have a different trend as  $n_{l04}$ .

From these discharges, we conclude the Faraday rotation measurements are sensitive to the electron density changes, and the FR#1 shows a similar percentage change as  $n_{l04}$ , as expected. To diagnose the current density profile change with the polarimeter, the density information from other diagnostics, such as TS or the interferometer, needs to be accurate, or else uncertainties in the density will mask any current induced change on the Faraday rotation signals.

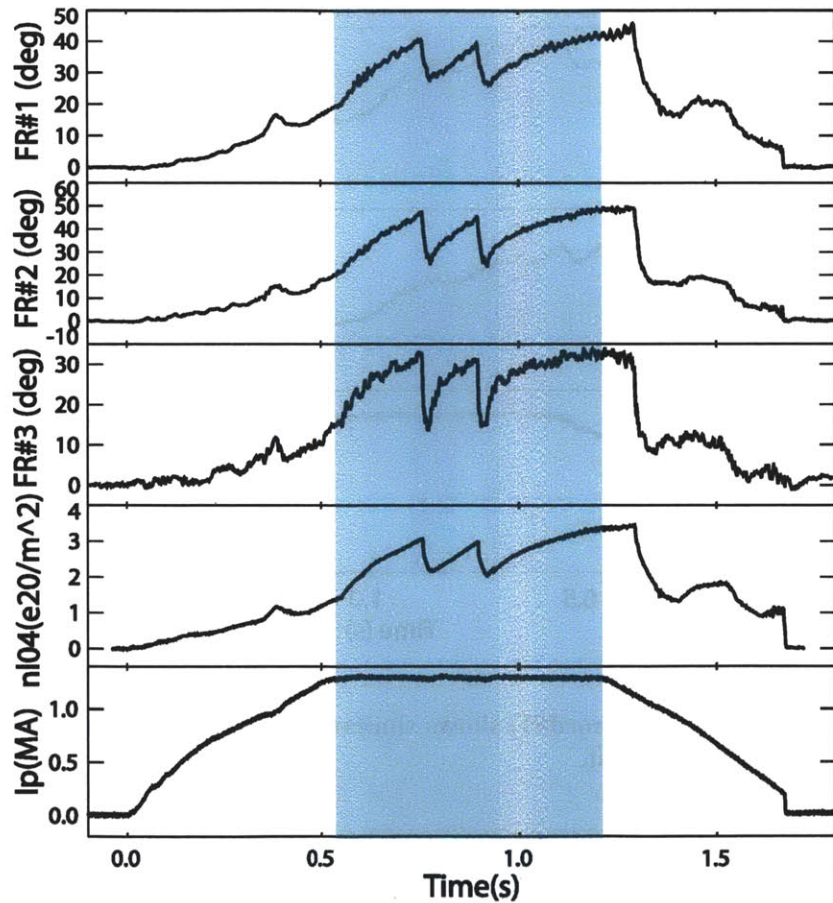


**Figure 4-8: H-modes observed on three-chord Faraday rotation signals, with a similar shape as the density trace during the current flat-top.**

### 4.3.2 Plasma Current Sensitivity

The Faraday rotation signal is proportional to the line integral of the magnetic field along the beam-path, so it does not measure the local plasma current, but approximately the total current inside the magnetic flux surface to which the beam-path is tangent, according to Ampere's law.

As a zeroth-order check on how the polarimeter responds to a change in the plasma current, we have compared the Faraday rotation measurements before and after changes were made in the C-Mod magnet configuration to reverse the direction of the magnetic fields and the plasma current. In Figure 4-9, for the discharge with the reverse plasma current, the Faraday rotation also reverses the sign.

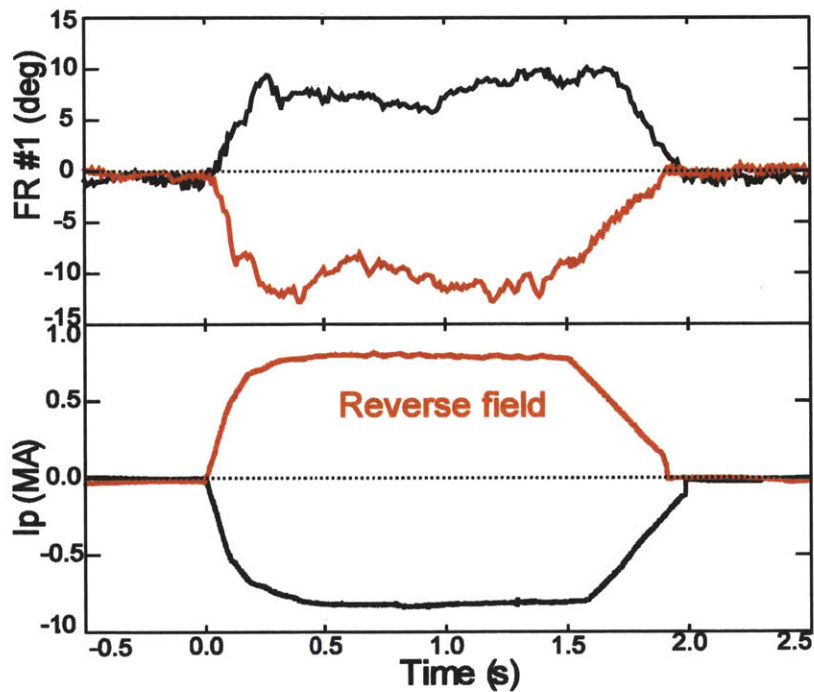


**Figure 4-9:** A zeroth-order check on polarimetry sensitivity to the changes in the plasma current. Discharges with reversed plasma current show the Faraday rotation reverses sign.

To more accurately evaluate the polarimetry sensitivity to the plasma current change, we ramp the plasma current, while keeping the density constant, and see how the Faraday rotation

responds. In Figure 4-10, when the plasma current ramps down from 1.51 to 1.7 s, the electron density ( $n_{l04}$ ) and  $B_t$  are constant, so that there should be no significant Faraday rotation change caused by the line-averaged density change or  $B_t$  ramp. The major radius of the LCFS reduces  $\sim 2$  cm and the minor radius of the plasma reduces  $\sim 1.1$  cm (5%), from 1.51 to 1.7 s (the plasma is inner wall limited after  $t=1.78$  s). The Faraday rotation signals for three chords drop  $\sim 15\%$  (#1),  $30\%$  (#2) and  $45\%$  (#3), respectively, which disagrees with the 35% decrease for the plasma current. Therefore, the Faraday rotation measurements not only respond to the plasma current change, but also indicate a change of the plasma shape during the current ramp.

As will be discussed in chapter 5, polarimetry has proved to be a useful supplement to other current profile diagnostics for LHCD experiments on C-Mod, particularly because of its high temporal resolution.

### 4.3.3 Plasma Position Sweep

When the plasma moves around or shrinks, the density and magnetic field along the polarimeter path can change, and the Faraday effect will change accordingly.

We have made piggy-back measurements on some plasma sweep discharges designed for MSE calibrations. During the MSE plasma sweep calibrations [69], the plasma edge is swept past multiple MSE channels, and the MSE-measured pitch angle is calibrated by comparison with the results computed by EFIT. Normally for these discharges, the plasma minor radius shrinks continually for  $\sim 1$ s, while maintaining the electron density and current density in the plasma core. The poloidal magnetic flux surfaces for two time-slices, one before the start of the sweep ( $t=0.6$  s), and the other near the end of the sweep ( $t=1.6$  s), are shown in Figure 4-11 for discharge 1120516020. The red curve is the LCFS, and the green lines represent the polarimetry chords. All three chords reach inside of the LCFS at  $t=0.6$  s. However, the edge chord is well outside the

LCFS at  $t=1.6$  s, by which time the major radius of the LCFS has been reduced from the initial 88 cm to about 77 cm, as shown in Figure 4-11c.

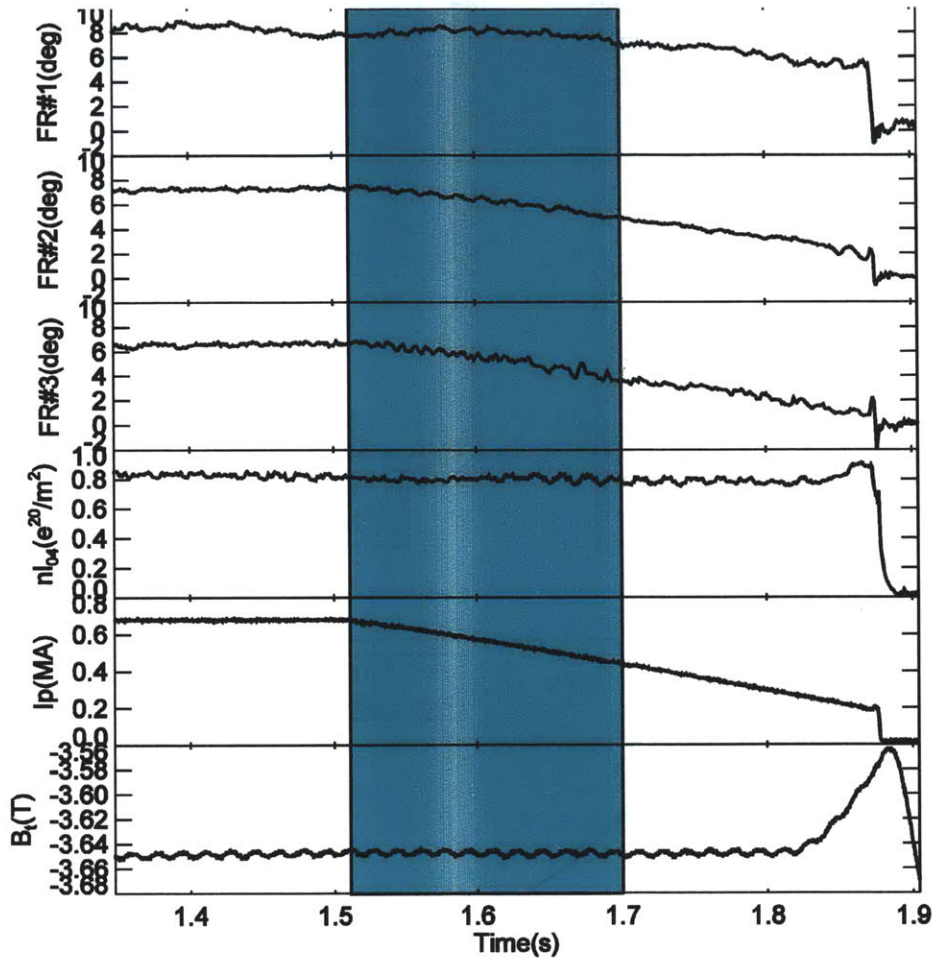
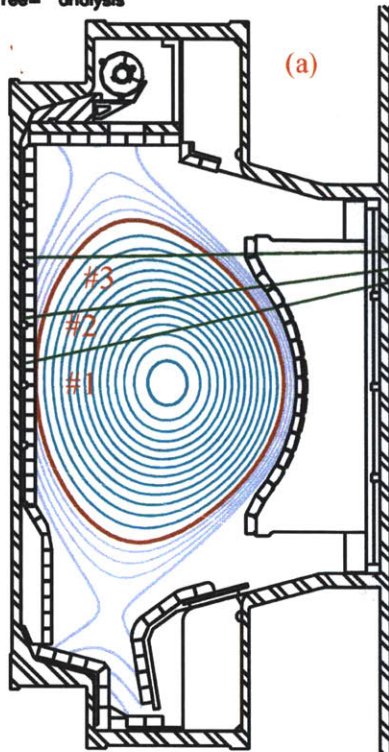


Figure 4-10: Plasma current ramps down from 680 to 440 kA (1.51 to 1.7 s), with relatively constant line averaged electron density. The plasma minor radius reduces  $\sim 1.1$  cm (5%). This process is during the flat-top for  $B_t$ , so there is no phase error due to a  $B_t$  ramp.

Shot= 1120516020 Time= 0.600 Ip = 0.79  
Tree= analysis



Shot= 1120516020 Time= 1.600 Ip = 0.45  
Tree= analysis

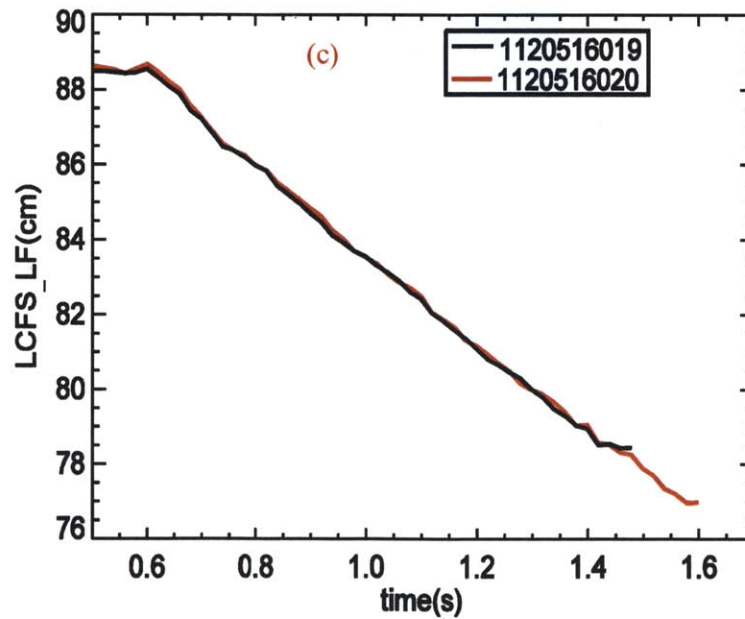
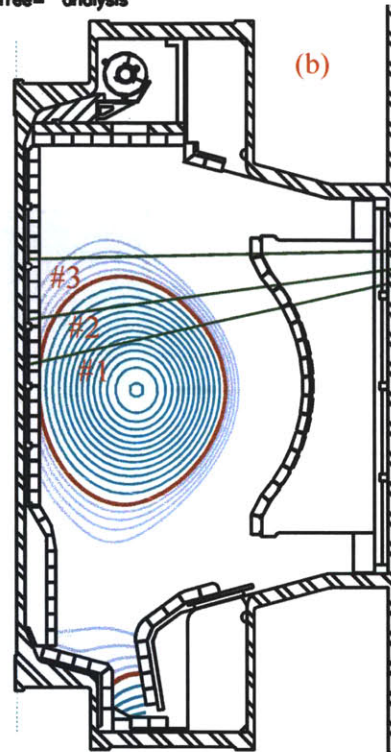


Figure 4-11: (a) C-Mod poloidal magnetic flux at  $t = 0.6$  s for shot 1120516020. The red contour indicates the LCFS, and the green lines are the three polarimetry chords. (b) C-Mod poloidal magnetic flux at  $t = 1.6$  s for shot 1120516020. (c) Major radius of the LCFS reduces  $\sim 10$  cm during plasma sweeping for 1120516019 (black) & 1120516020 (red)

The Faraday rotation measurements for two similar plasma sweep discharges are shown in Figure 4-12. For shot 1120616020 (red), the Faraday rotation angle for the edge chord (third frame) drops continually, when the plasma current decrease from 800 to ~500 kA. The Faraday effect for this chord is zero at ~1.6 s as expected, because the beam-path for the edge chord is well outside the LCFS from Figure 4-11(b), and thus the density is expected to be very low along this chord. The Faraday rotation is almost constant for the inner-most chord (first frame), and drops only slightly for the middle chord (second frame) as the minor radius is reduced, since major contributions for each of these chords is from the high density plasma core. Similar results have been observed for shot 1120516019 (black).

We can infer what happens to the plasma from the different dynamics of the three-chord Faraday rotation time traces. The Faraday rotation of the edge chord drops to zero, indicating the plasma is shrinking, so that the edge chord is outside the LCFS, and the small change of the Faraday effect for the inner chords indicates the plasma density and current are maintained in the core during the sweep.

#### **4.3.4 Sawtooth Crashes**

Sawtooth oscillations are the result of a periodic relaxation process in the center of the plasma. The core temperature rises during the sawtooth ramp phase, and crashes due to MHD instability ( $m=n=1$  mode, where  $m$  is the poloidal mode number and  $n$  is the toroidal mode number) which is associated with central safety factor  $q_0 < 1$  [70]. During the crash,  $q_0$  rapidly increases and the current density profile flattens. The central current density decreases ~20% during a sawtooth crash on MST, by polarimetry and interferometric measurements [71]. Normally, we use the core electron temperature, measured by Electron Cyclotron Emission (ECE) [10], to diagnose the sawtooth oscillations and measure the sawtooth inversion radius (SIR) [72].

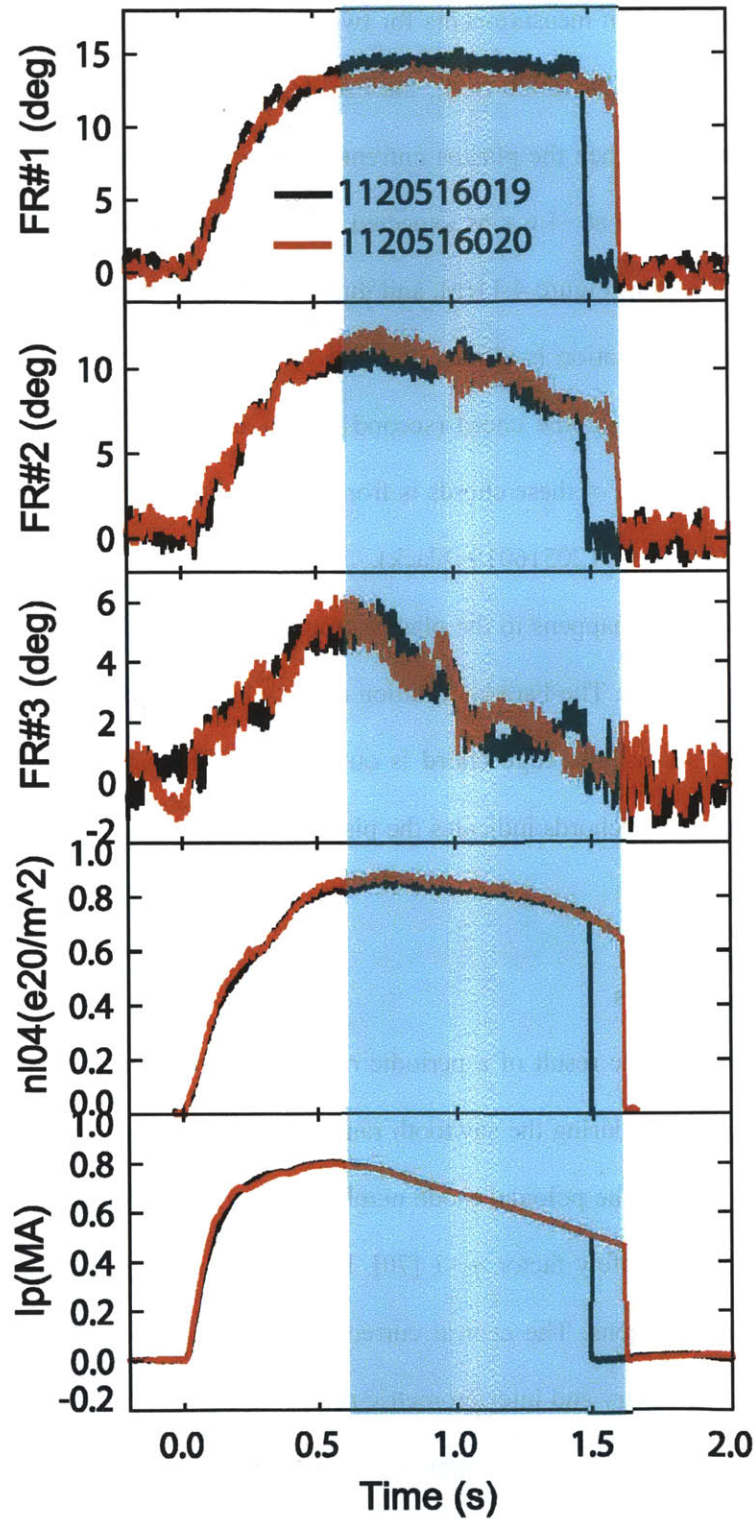
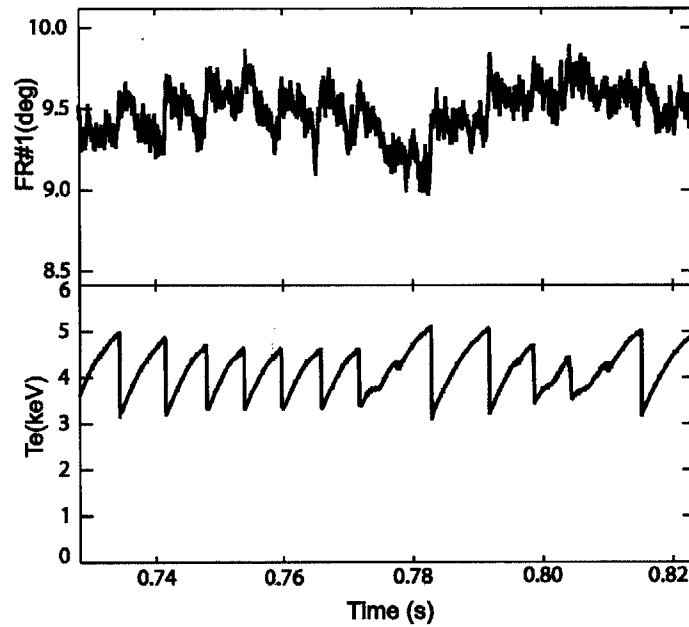


Figure 4-12: Three-chord Faraday rotation measurements for two plasma sweep discharges, 1120516019 (black) & 1120516020 (red). Plasma is shrinking while maintaining density and current in the core, as implied by the polarimetry and TCI measurements.

On C-Mod, the sawtooth cycle has a frequency around 100 Hz, and the crash time is  $\sim 100 \mu\text{s}$ , which can be easily captured by the polarimetry. If the current density profile flattens during the sawtooth crash, we expect to see the Faraday rotation signals drop, assuming the density is relatively constant. However, we found the Faraday rotation signals for most of the discharges actually jump up during the crashes. In Figure 4-13, the lower trace is the core electron temperature from ECE, and it sharply decreases from  $\sim 5$  to 3 keV in a crash and climbs back in a cycle in 5 to 10 ms. The top trace is the Faraday rotation signal for chord#1, which increases  $\sim 0.5^\circ$  ( $\sim 5\%$  of the total Faraday rotation) and perfectly aligns with the timing of crashes seen on the electron temperature. This phenomenon has been regularly observed on all three polarimetry chords. We do observe that the polarimetry signal on the inner most chord (#1) drops during sawtooth crashes for some plasma discharges. In Figure 4-14, the core temperature decreases from  $\sim 3$  to 1.5 keV during the sawtooth crashes, and the FR #1 drops  $\sim 1^\circ$  ( $\sim 3\%$ ), while FR#2 increases  $\sim 1^\circ$  ( $\sim 3\%$ ).

From ECE data, the SIR is similar for these two shots, as shown in Figure 4-13 and Figure 4-14. However, the normalized poloidal flux (from EFIT) at the polarimetry chord tangency points ( $\psi_1 \approx 0.18$ ,  $\psi_2 \approx 0.40$  and  $\psi_3 \approx 0.56$ ) for the high density ( $n_{104} \approx 2 \times 10^{20}/\text{m}^3$ ) high current (1.3 MA) shot in Figure 4-14 are significantly different from those of typical C-Mod discharges, which are  $\psi_1 \approx 0.25$ ,  $\psi_2 \approx 0.5$  and  $\psi_3 \approx 0.7$ . By mapping the poloidal flux to the mid-plane, we found the two edge polarimetry chords are always well outside of the SIR, thus they should see minor density increments over the whole beam path in the plasma. The density increment may dominate the effect of the magnetic field decrement from the current profile flattening, and thus we have seen the Faraday rotation signal for the two edge channels always increases during the sawtooth crashes. For chord#1 in Figure 4-13,  $\psi_1 \approx 0.25$  which is around the SIR, and density effect may still dominate the effect of the current flattening. However in Figure 4-14,  $\psi_1 \approx 0.18$  for chord #1, which is inside the SIR, and therefore this chord should see a

relatively large effect from the current flattening, with minor density decrement along the beam path inside the SIR, which might dominate the slight density increment over the other parts the beam path outside the SIR, consistent with the Faraday rotation increase seen on this chord across the sawtooth crash. We will be able to capture more details on sawtooth crashes, if the polarimetry system is upgraded to more chords and able to reach the magnetic axis (this upgrade was scheduled in one or two years term with funding).



**Figure 4-13: Effects of sawtooth crashes on the polarimeter Faraday rotation angle. The angle on chord#1 increases during each crash.**

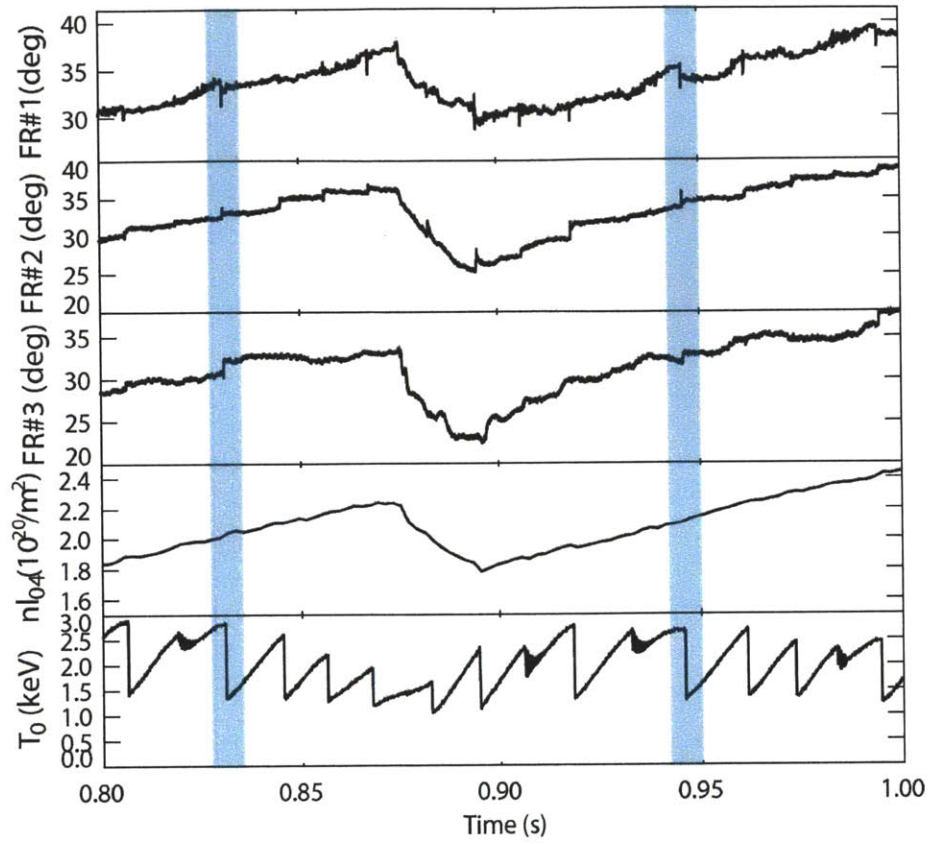


**Figure 4-14: Sawtooth crash effect seen on all three polarimetry chords (1120621019). For this shot, the Faraday rotation drops for chord#1, and increases for other two chords during each crash.**



## 5. LHCD Experimental Results

As first discussed in chapter 4, the three-chord polarimetry system was found to be sensitive to the plasma current and thus can be used to diagnose changes in the current density profile. In this chapter, we will present the polarimetry measurement results for LHCD experiments performed during the 2012 C-Mod campaign, and show how polarimetry is used to constrain EFIT reconstructions.

Section 5.1 introduces a typical LHCD discharge with a significant current density profile change during the LH. What we expect the polarimeter to see during LHCD will also be discussed.

In section 5.2, LHCD experiments with a LH power scan, an LH pulse scan, a plasma density scan, a current scan and an LH phase scan are presented. The polarimetry results not only confirm the LHCD results from previous numerical simulation and experimental observation, including density limit results and off-axis current drive, but also led to the discoveries of the dependences of the current drive efficiency on plasma current and LH phasing.

In section 5.3, a synthetic polarimetry signal has been built, using density profiles from TS and the magnetic field profile from EFIT. The polarimetry measurement agrees well with the prediction from normal EFIT (no internal constraints from pressure or MSE,  $q_0$  is constrained to 0.95, as defined in chapter 1) for sawtooth discharges, without LHCD. A significant discrepancy between the measurement and the EFIT prediction appears with LH. Polarimetry measurements are also compared with Kinetic-EFIT prediction, and the agreement is found to be much better than the normal EFIT prediction during LH. The polarimeter can be easily converted to measure the Cotton-Mouton effect (C-M), which agrees with the normal EFIT prediction for a non LH discharge.

In section 5.4, we present the first attempt to incorporate the polarimetry measurements into EFIT by optimizing the constraint of the central safety factor  $q_0$ . The result shows a significantly flattened current density profile during LHCD.

## 5.1 A Typical LHCD Discharge

In order to overcome the tokamak pulse length limitations of the plasma discharge with Ohmic current drive, lower hybrid current drive (LHCD), an efficient non-inductive current drive method, has been studied on C-Mod and elsewhere [73][74][75][76]. A typical C-Mod discharge with LHCD is shown in Figure 5-1. The fourth trace is the toroidal loop voltage ( $V_{loop}$ ) measured on the plasma surface, and in steady state should be the same as the loop voltage in the plasma.  $V_{loop}$  is usually around 1 V depending on the plasma parameters. In this shot, it drops in magnitude to around 0.3 V with 800 kW LH pulse (0.9 -1.4 s), which indicates that the LH is driving part of the current. The total plasma current is constant (second trace), so some of the Ohmic current is replaced by the LH driven current (For these low density, low beta-p plasmas, the bootstrap effect is negligible.).

Kinetic-EFIT (defined in chapter 1) shows the off-axis current drive for LH, and the current profile is flattened during the LHCD. The current density and safety factor ( $q$ ) profiles at three different time-slices from Kinetic-EFIT are shown in Figure 5-2. The current density profiles are fit well by Gaussian functions, and the central safety factor  $q_0$ , is less than 1 before ( $t=0.72$  s, black traces) and after ( $t=1.72$  s, blue traces) the LH pulse. During the LH pulse ( $t=1.32$  s, red traces), the current profile is much flatter and the core current density drops by about 35%. The sawtooth oscillations from soft x-ray measurements [10] (bottom trace in Figure 5-1) are suppressed at  $t \approx 1.32$  s, consistent with  $q_0 > 1$ .

With the evolution of the current density profile from Kinetic-EFIT, we can estimate how the polarimetry signals should respond to the current drive, assuming the plasma density is

relatively unchanged. When the current profile is flattened during the LHCD, the core poloidal magnetic field becomes weaker according to Ampere's law (less core current), and FR#1 (Faraday rotation measurement for the inner-most chord) should drop. Since the edge poloidal magnetic field will not change much with a nearly constant total plasma current, FR#3 (edge-most chord) should not be significantly affected by the current profile change. FR#2 may modestly decrease, as it is located between the other two chords.

After the LH is turned off, as the current density profile relaxes back to the Ohmic current profile (peaked), FR#1 should significantly increase. The polarimetry measurements confirm these expectations, and will be discussed in detail in the following sections.

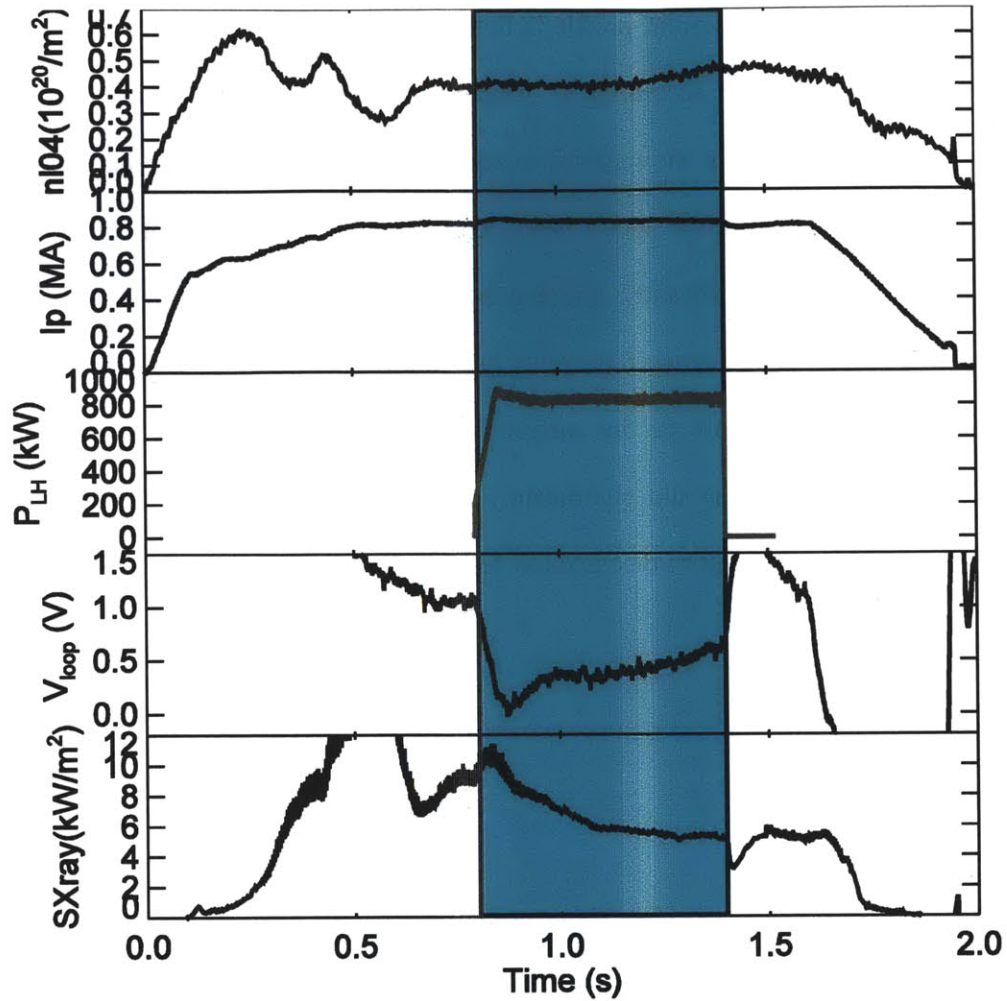


Figure 5-1: A typical LHCD discharge (shot 1120612027). Loop voltage drops in magnitude during LHCD, since some of the Ohmically driven current is replaced by LH driven current. Sawtooth oscillations, as measured with soft x-rays, are seen to disappear after the LH turn-on.

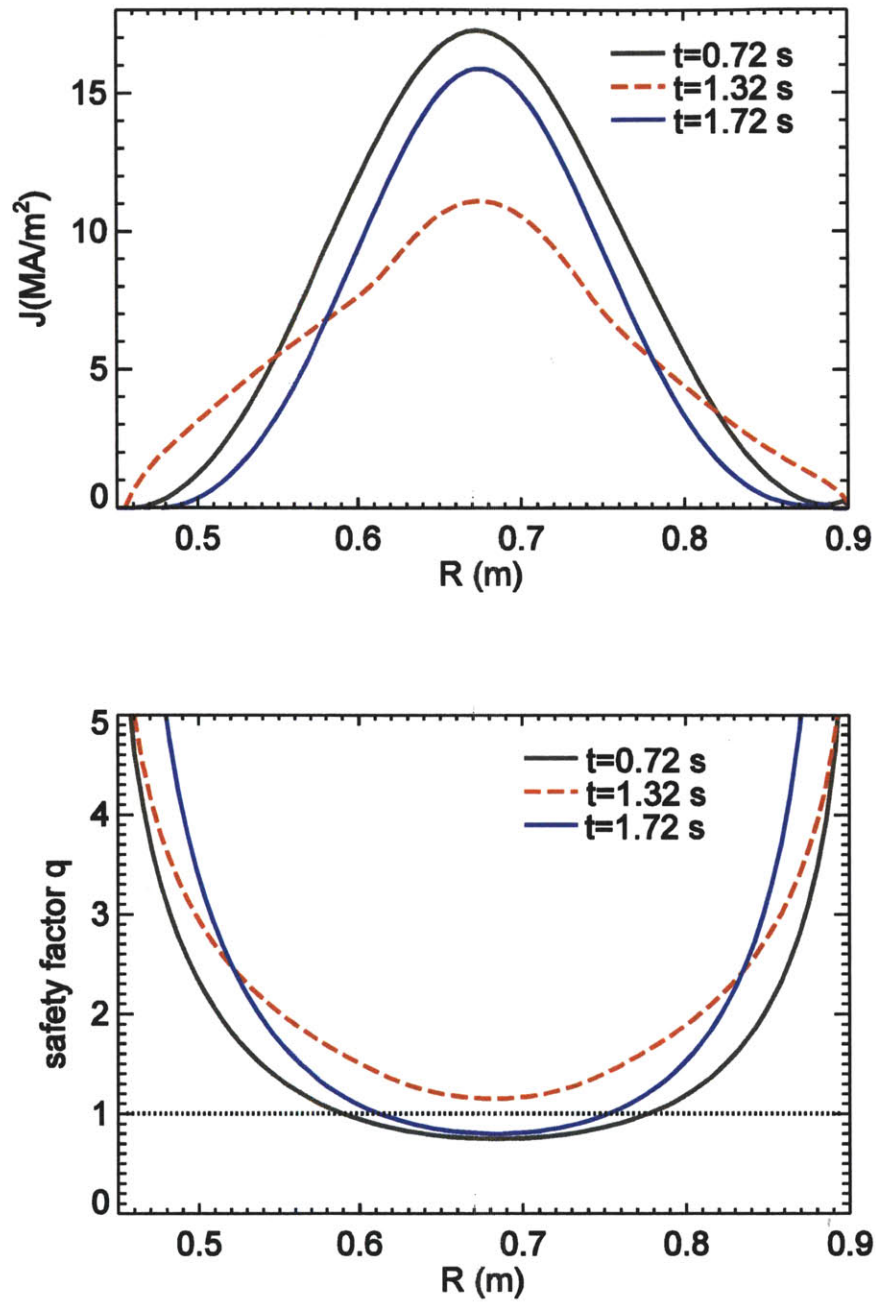


Figure 5-2: Current density and safety factor ( $q$ ) profiles at three time-slices from Kinetic-EFIT: before the LH ( $t= 0.72$  s, black traces), during the LH ( $t=1.32$  s, red traces) and after the LH ( $t= 1.72$  s, blue traces). The LH pulse is from 0.8-1.4 s.

## 5.2 LHCD Experiments

The Faraday rotation change during the LHCD can be affected both by electron density and current density profile changes. To diagnose the current density profile change on the polarimeter signals, we have tried to keep the density as flat as possible for the following experiments, since the Faraday rotation measurements are sensitive to the density change, as clearly shown in section 4.3. It is still typical to see 10% to 20% density variation during the LHCD. However, the polarimeter signal changes up to ~50% for non-inductive LHCD discharges, so that we can clearly see the current drive effect in the following polarimeter data, even with some contributions from changes in density.

### 5.2.1 LH Power and Pulse Scan

In the first LH experiment, we want to observe that the polarimeter is indeed sensitive to the off-axis current drive on C-Mod. Since FR#1 is expected to show the largest phase change during the LHCD among the three chords, we will use it to show the current drive effect. Three LH discharges with similar parameters are shown in Figure 5-3. When LH turns on at  $t \approx 0.7$  s, FR#1 (top trace) drops 30-50% for all three discharges. The total current is nearly constant, and the line averaged density only varies about 10% during that time period, suggesting that the Faraday rotation decrease comes mainly from the current profile change. A flattened current density profile can explain the drop of FR#1 from 0.7-0.9 s, as analyzed in section 5.1. There is no significant change in Faraday rotation from 0.9 s to the end of the LH pulses, showing the driven current is well sustained. Immediately after turning off the LH, the Faraday rotation signal starts to increase, indicating that the current is peaking. Both the processes of decrement and increment for FR#1 last for ~0.2 s, matching the current relaxation time on C-Mod. Current relaxation time can be approximated as [77]

$$\tau_{CR} \approx 1.4 a^2 \kappa T_e^{1.5} (\text{keV}) / Z_{eff} \quad (5.1)$$

where  $Z_{eff}$  is the resistivity enhancement due to impurities, and  $\kappa$  is the plasma elongation. Assuming  $Z_{eff} = 1.5$ ,  $\kappa = 1.6$  and  $T_e \approx 2$  keV,  $\tau_{CR} \approx 200$  ms. At the end of the shot, FR#1 starts to drop due to the density change.

The three discharges have slightly different turn-off time for the LH pulse. For all discharges, the Faraday rotations immediately increase after LH turns off, whether the density is increasing (red and green traces) or dropping (black trace). Therefore, the response of the Faraday rotation signal comes from the current profile change, which dominates over the density change effect and random phase noise.

LH power was also scanned to measure the correlation of the Faraday rotation changes with current drive power. The Faraday rotation is calculated by averaging the phase during the later part of the LH pulse when the driven current is steady, such as 1-1.3 s. For the Faraday rotation before the LH, we pick a 10 ms period where the average plasma density is the same as the average density during the LH. In this way, the derived Faraday rotation change mainly comes from the current profile difference, and is not affected by a density variation, assuming the density profile is relatively constant during the current flat top for these LHCD discharges. The Faraday rotation changes with the LHCD for all three chords are shown in Figure 5-4.

The error bars are estimated to be  $\pm 0.1^\circ$  for chord #1,  $\pm 0.2^\circ$  for chord #2 and  $\pm 0.5^\circ$  for chord #3. These estimates are determined by observing the phase error during magnetic field only test shots. The different noise level for each chord is still under investigation. One of the possible reasons for higher noise levels of chord #2 and chord #3 is that these two chords have considerably lower signal levels and more optical components. Another possible reason is that the reference beam is split from and shares the chord #1 beam. Therefore, some vibrational noise shared by the reference and chord #1 might be better cancelled out in the chord #1 signal.

There is a clearly a systematic increase of rotation for chord #1 as a function of LH power. The amount of FR#2 change also slightly increases with the LH power, but not clearly outside of the error bars. FR#3 is usually too noisy for useful measurements for low density LHCD discharges, but it does show a different trend from the other two channels in this plot. FR#3 change might be dominated by the variation of the edge plasma density.

The dynamics of the Faraday rotation signals confirm that the current density profile is flattened during current drive, and then re-peaks after the LH is turned off, and the time scales are consistent with expected current relaxation time.

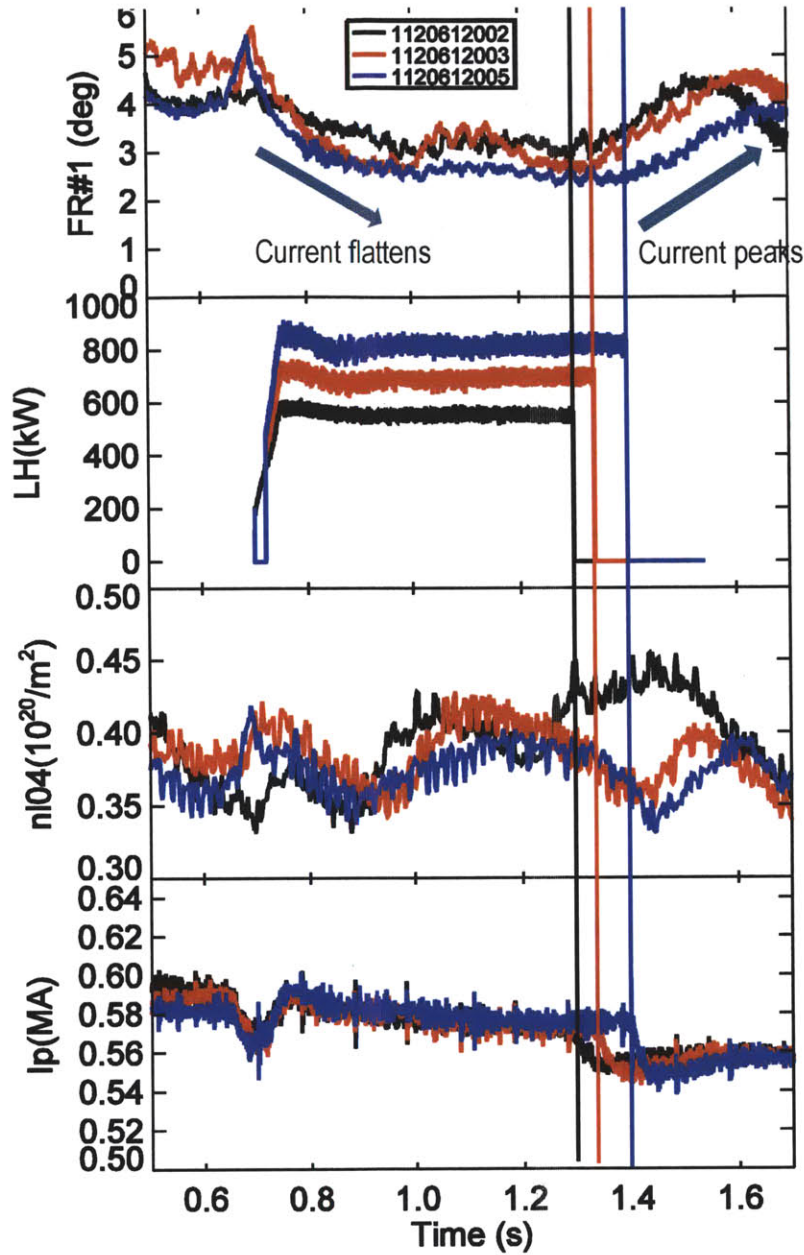


Figure 5-3: Faraday rotation time traces (FR#1) for shots 1120612002, 1120612003 and 1120612005 with LH pulse scan. The LH power is 600 kW, 700 kW and 800 kW respectively, and the LH turns off at different times. The Faraday rotation immediately starts to responds to the changes in LH power.

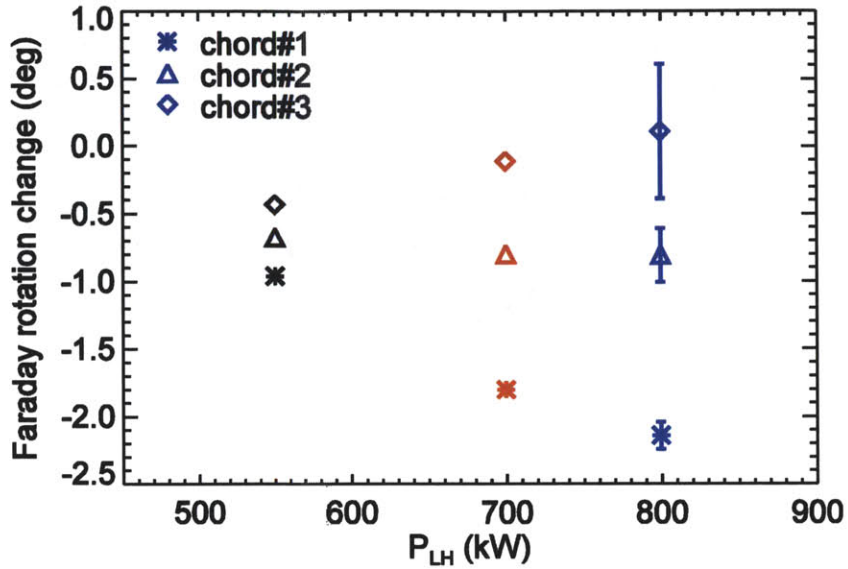


Figure 5-4: Faraday rotation changes for all three chords with shot-by-shot LH power scans. The systematic increase of rotation angle is clearest for the innermost chord (#1).

### 5.2.2 Plasma Density Scan

Previous LHCD experiments demonstrated the dependence of the current drive efficiency on the electron density in C-Mod [25][78][79]. Hard x-ray (HXR) bremsstrahlung from lower hybrid driven fast electrons is used as a proxy to compare the current driven efficiency for different plasma discharges. The HXR diagnostic has 32 poloidally-viewing channels that span the whole cross section of the plasma, with a spatial resolution of 2 cm. It detects photons at energies of 20-200 keV, with 1 keV energy resolution [10][80].

Figure 5-5 shows that the HXR count rates (green circles), which have been normalized to the LH power, decrease exponentially as the line averaged density increases. Above a line averaged density of  $1.0 \times 10^{20} / \text{m}^3$  ( $n_{l04} \approx 0.6 \times 10^{20} / \text{m}^2$ ) the LHCD efficiency becomes poor. The density limit cannot be explained by bad lower hybrid wave accessibility, since it is lower than the inaccessible density region (pink region). A synthetic HXR diagnostic has been applied to simulations using ray-tracing/Fokker-Planck codes (GENRAY/CQL3D), and compared with the

experimental data. The X-ray count rates expected from the simulations (black curve in Figure 5-5) are much higher than the experimental data, with most dramatic shortfall occurring at the highest densities.

The interaction of LH waves with the Scrape-off layer (SOL) plasma could be an important effect contributing to the reduction of current drive efficiency in high density plasmas. The newly developed SOL-reflectometer found that the density profile in the SOL region changes significantly during LH for high density plasmas [78][79]. A SOL model including the electron-ion collisions was therefore developed in CQL3D. The simulated HXR rate with this model shows better agreement with the experimental observations, especially when the SOL model with high collision frequency is included, but is still a factor of about 10 too high.

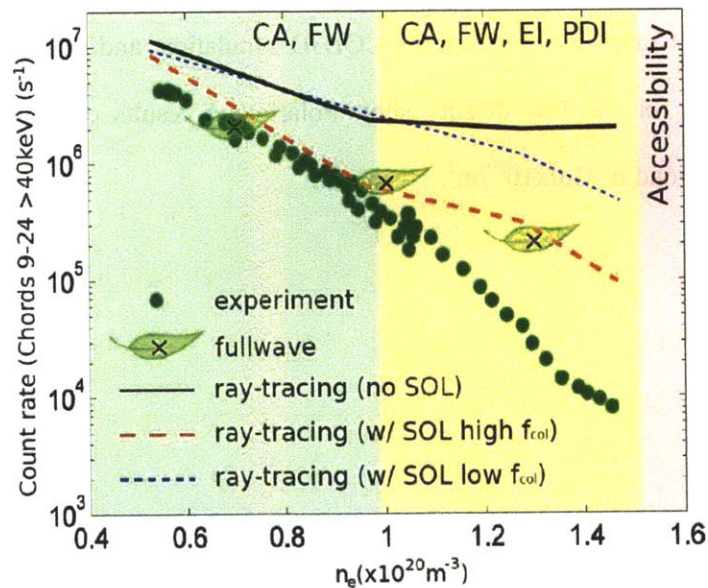


**Figure 5-5: For LHCD discharges with densities below about  $1 \times 10^{20} \text{ m}^{-3}$ , HXR count rates drop at approximately the expected exponential rate as a function of line average density. At higher densities, the fall-off becomes unexpectedly rapid, and LHCD efficiency on C-Mod is weak above this density threshold. (Figure from [81])**

A simulation code (LHEAF [27]) was developed to incorporate full-wave effects, such as diffraction and scattering, which are not included in GENRAY. LHEAF indicates the LH waves are mainly absorbed just inside of the LCFS ( $0.8 < r/a < 1$ ), which also potentially explains the low current drive efficiency at high density, as shown in Figure 5-5.

The polarimeter was used to examine this LHCD density limit with a shot-by-shot density scan. Time traces of four consecutive LHCD discharges (1120612005, 6, 7, 9) with the same plasma current (580 kA) and line averaged density  $n_e$  from  $\sim 0.6$  to  $1.05 \times 10^{20}/\text{m}^3$  are plotted in Figure 5-6. Similar to the analysis in section 5.2.1, we average the Faraday rotation angle during the LHCD, and then calculate its difference with the Faraday rotation angle before the LH where there is a similar density, to quantify the Faraday rotation change. The results are shown in Figure 5-7. Both the change of FR#1 and FR#2 decrease with higher density, which demonstrates the LHCD efficiency decreases with higher density. The green shot ( $\sim 1.05 \times 10^{20}/\text{m}^3$ ) is the point where the HXR count rates diverge from the CQL3D simulation, and FR#1 drops less than  $0.5^\circ$  comparing with  $\sim 2^\circ$  for the low density shot. Polarimeter results confirm the current drive efficiency is poor beyond  $n_e = 1.0 \times 10^{20}/\text{m}^3$ .

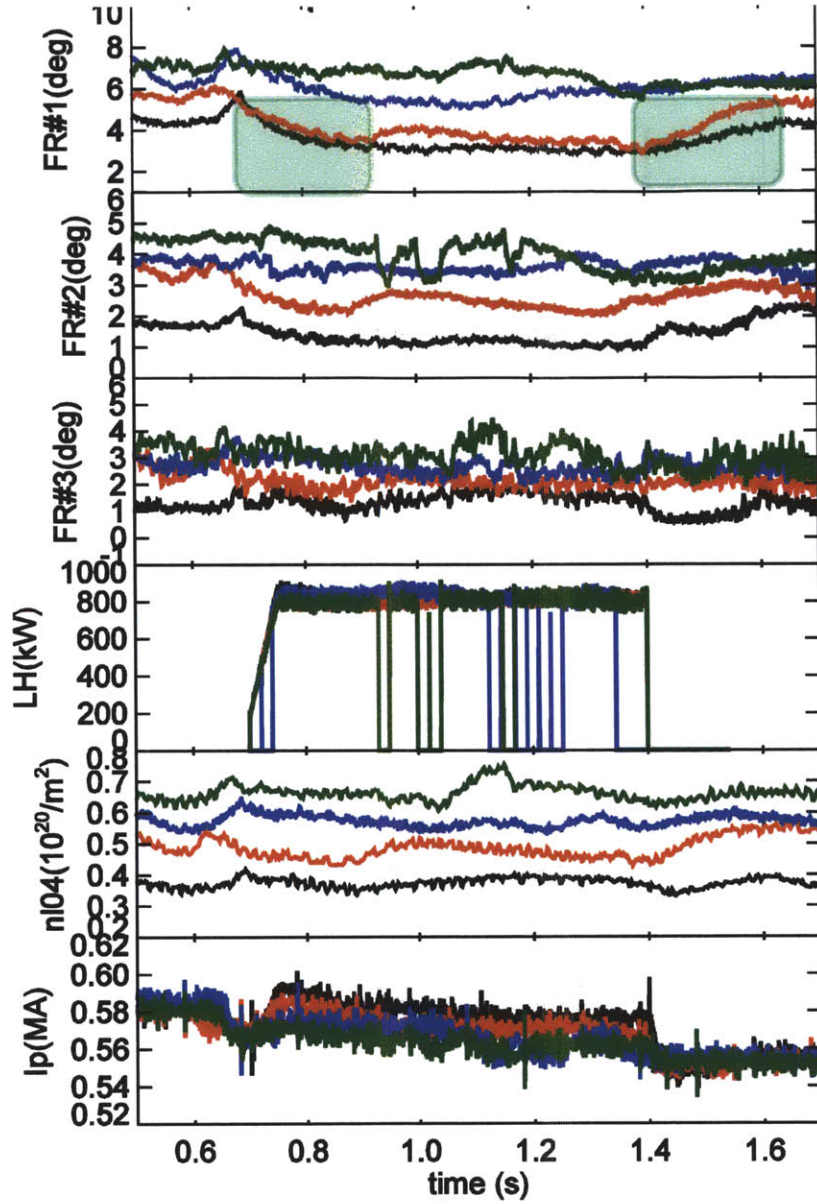
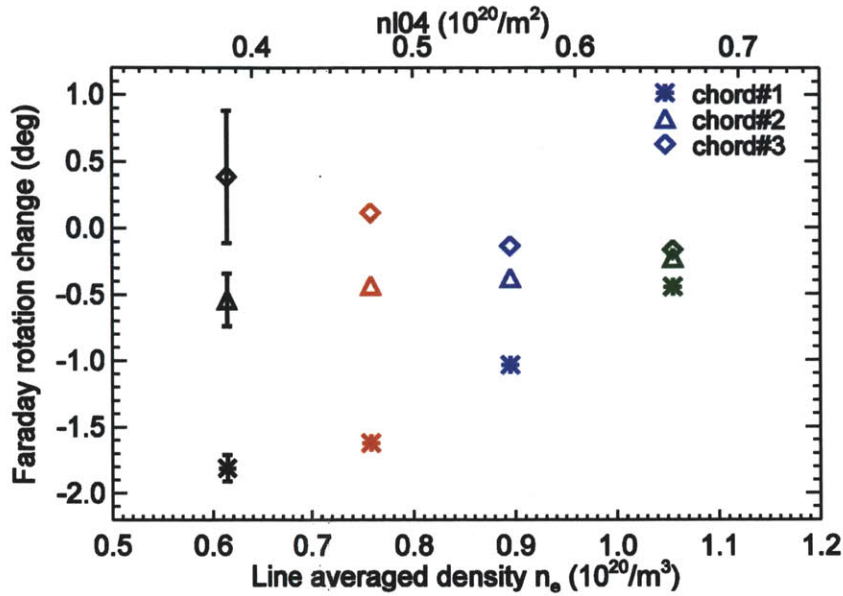


Figure 5-6: Four consecutive discharges with a shot-by-shot density scan ( $0.4$  to  $0.7 \times 10^{20}/\text{m}^2$ ).  $I_p=580$  kA,  $LH=800$  kW. Strong LHCD effect observed on FR#1, for low density shots (black and red), very weak LHCD effect observed for shot over the density limit (green shot).



**Figure 5-7: Faraday rotation change during the LHCD for a shot-by-shot density scan. Both the change of FR#1 and FR#2 decrease with higher density**

It has also been found that the HXR count rates do not drop as dramatically during inner wall limited discharges as compared to diverted discharges, so polarimeter results during limited discharges should also be of interest. HXR count rates for diverted discharges with large or small (3-5 mm) gaps and fully limited discharges are shown in Figure 5-8. The inner-wall limited discharges (blue stars) have much higher count rates than the diverted discharges.

The polarimeter observed some weak current drive for a limited discharge in the 2012 run campaign. In Figure 5-9, 1120612009 (black trace) is a diverted discharge and 1120612015 (red trace) is a limited discharge, both of which have the same density, and total current and LH power. FR#1 shows a slightly larger decrease in rotation for the limited discharge during the LH, and a larger increase after LH is turned off. The FR#1 signal changes  $\sim 15\%$  during LH, compared with  $\sim 40\%$  for the low density LHCD discharges. Therefore, some weak current drive is indicated by the polarimetry measurement, which is qualitatively consistent with non-thermal ECE (GPC2) observation (third frame). Although the LH trips for the diverted discharge, non-thermal ECE

measurement already shows some discrepancy between the two shots before the LH trips, so the trips cannot explain different current driven efficiency.

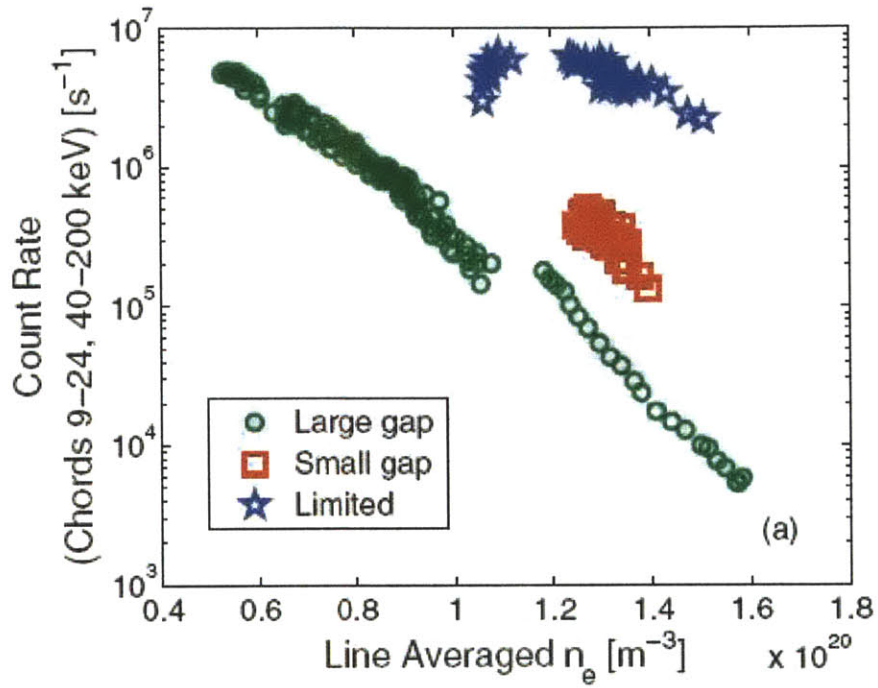


Figure 5-8: HXR count rate as a function of the line averaged density. Inner wall limited discharges (blue stars) has higher count rate than the diverted discharges with large and small (3-5 mm) inner gaps. (Figure from [79])

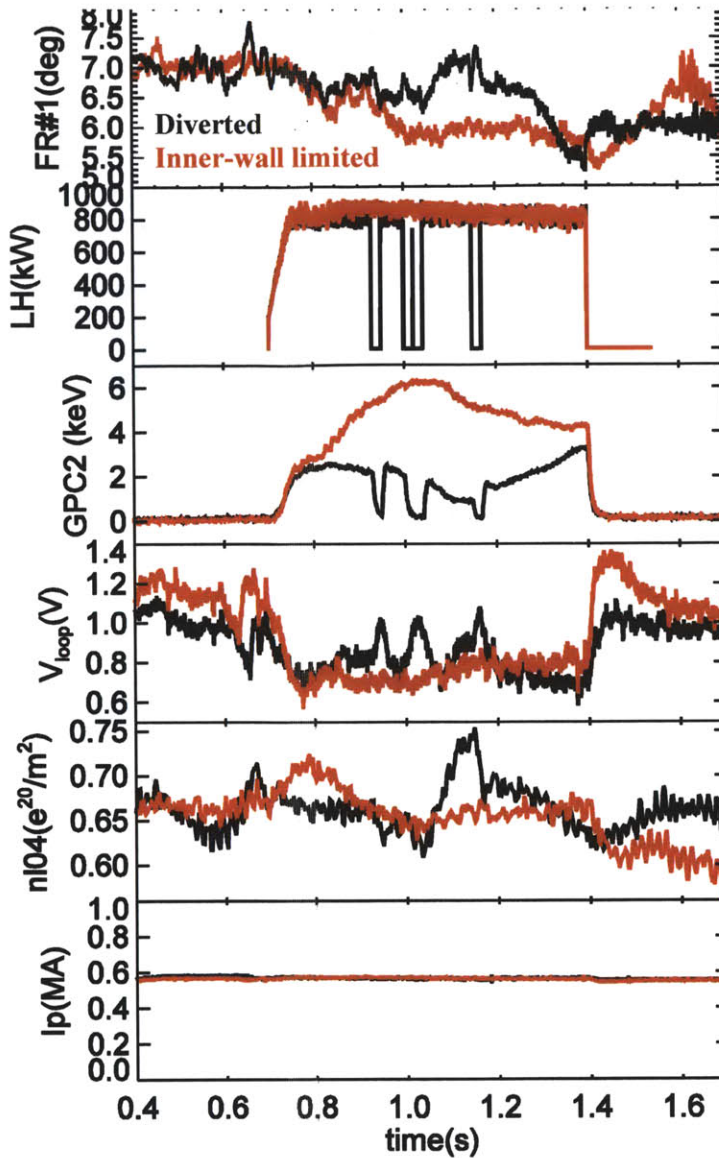
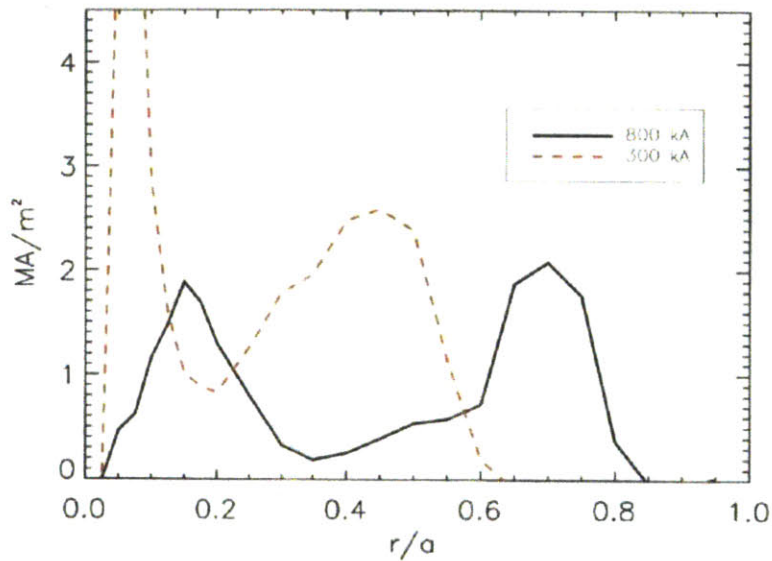


Figure 5-9: Time traces of a high density limited discharge (red) are compared with a diverted discharge (black). Some weak LHCD for the limited discharge is observed by the polarimeter, which is qualitatively consistent with non-thermal ECE measurements.

### 5.2.3 Plasma Current Scan

Although according to theory (Equation 1.22) the LHCD efficiency is independent of the plasma current, GENRAY/CQL3D simulations show the position of the LH power deposition depends on the plasma current [82]. In Figure 5-10, two LHCD discharges with different plasma current and

the same plasma density were simulated by GENRAY/CQL3D. The power mainly deposits inside of  $r/a=0.6$  for the shot with  $I_p=300$  kA (red), but with a significant component for  $r/a$  between 0.6 and 0.8 for the 800 kA shot (black). This simulation predicts that LH deposits more power close to the edge for high current shot. We believe this result is a consequence of toroidal wave propagation and upshifts in the launched  $n_{||}$  spectrum.



**Figure 5-10: LHCD power deposition for 300 kA (red) and 800 kA (black) discharges, simulated by GENRAY/CQL3D. LH deposits more power close to the edge for high current shot. (Figure from [82])**

The three-chord polarimeter can be used to infer the location of the driven current, since each chord has different sensitivities for the current driven at different locations. In Figure 4-11, the magnetic flux surfaces for the three polarimetry beam-paths tangent to  $\psi_1 \approx 0.25$ ,  $\psi_2 \approx 0.5$  and  $\psi_3 \approx 0.7$  for a typical C-Mod discharge are shown. The three chords approximately respond to the core plasma current decrements inside of  $\psi_1$ ,  $\psi_2$  and  $\psi_3$ , which should be equal to the driven current outside of  $\psi_1$ ,  $\psi_2$  and  $\psi_3$  respectively. By observing the LHCD effect on different chords, we may infer what the current density profile looks like and where the current is dominantly driven.

Figure 5-11 shows time traces for four LHCD discharges, with  $I_p=580$  kA for 1120612005 (black) and 1120612017 (red), and  $I_p=800$  kA for 1120612027 (blue) and 1120612028 (green). With a density of  $n_{l04}\approx 4 \text{ e}^{19}/\text{m}^2$  and LH power at 800 kW, strong LHCD was achieved for all four discharges, since the loop voltage drops dramatically and significant levels of non-thermal electrons are detected by ECE.

The Faraday rotation changes during the LH pulses are shown in Figure 5-12. FR#1 decreases significantly for both the low and high current shots, thus the driven current has major components outside of  $\psi_1\sim 0.25$ . FR#2 decreases about three times more for 800 kA ( $\sim 1.5^\circ$ ) than 580 kA ( $\sim 0.5^\circ$ ) shots, implying there is more current driven outside of  $\psi_2\sim 0.5$  for  $I_p\approx 820$  kA than for  $I_p\approx 580$  kA. FR#3 drops  $\sim 1^\circ$  for the green shot, which is outside the error bar of  $\sim 0.5^\circ$ , and its Faraday rotation time trace in

Figure 5-11 follows similar trends to those of the other two chords. These observations indicate some current is driven outside of  $\psi_3\sim 0.7$  for the high current case. Polarimetry responses for the three chords suggest that there is more driven current close to the edge for the high current discharges, and these experimental results agree with previous CQL3D simulations.

The polarimetry measurements have shown an ability to infer the current driven location with only three line-integrated signals. With potentially more chords in operation in the future, the location of the driven current could be much more accurately measured. With enough measurement chords, the current profile can be parametrically fitted with the free parameters in the current profile models, as discussed in chapter 2.

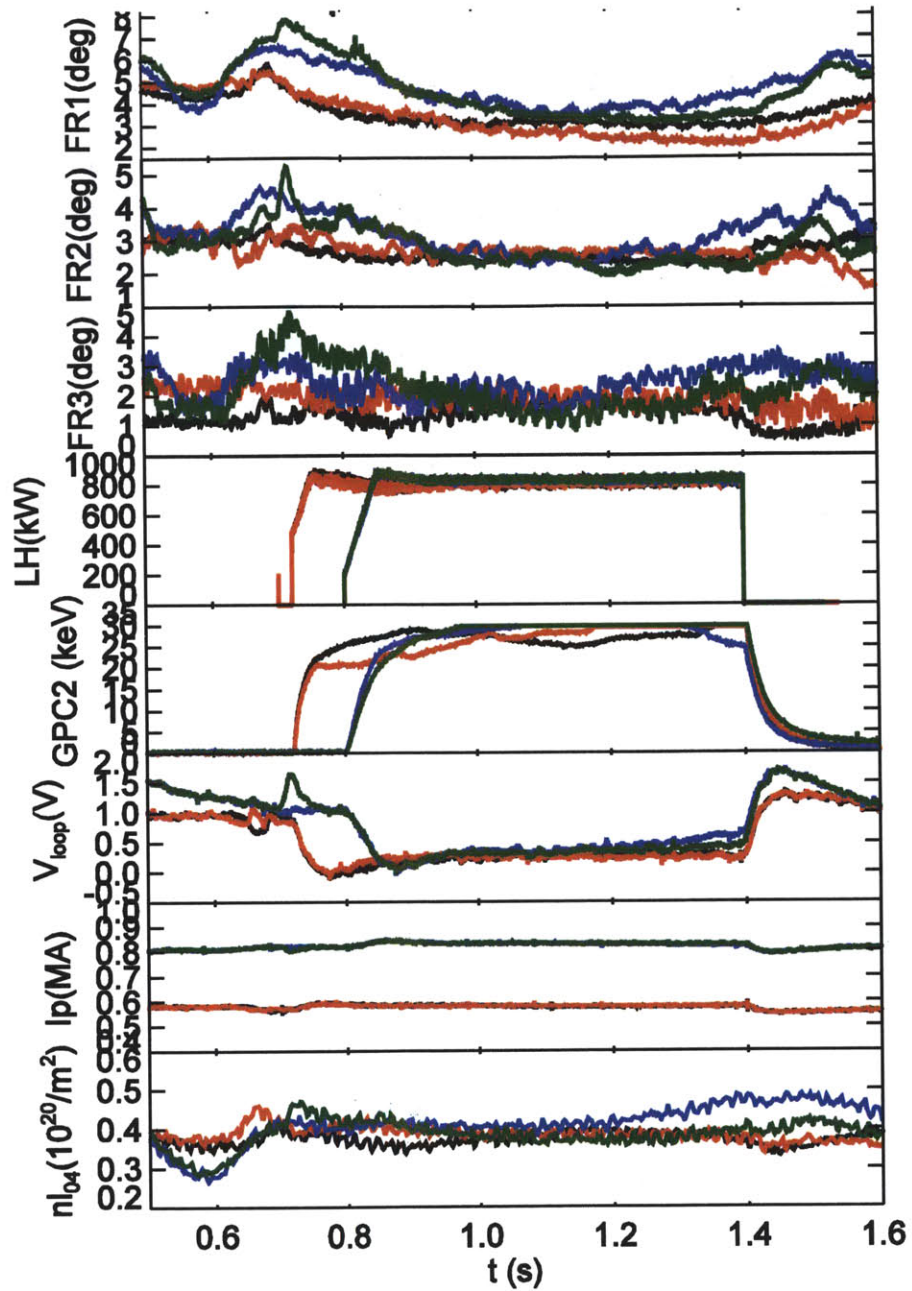


Figure 5-11: Different LHCD effects are observed by the polarimeter for shots with  $I_p= 580$  kA (black, red) and  $I_p= 800$  kA (blue, green)

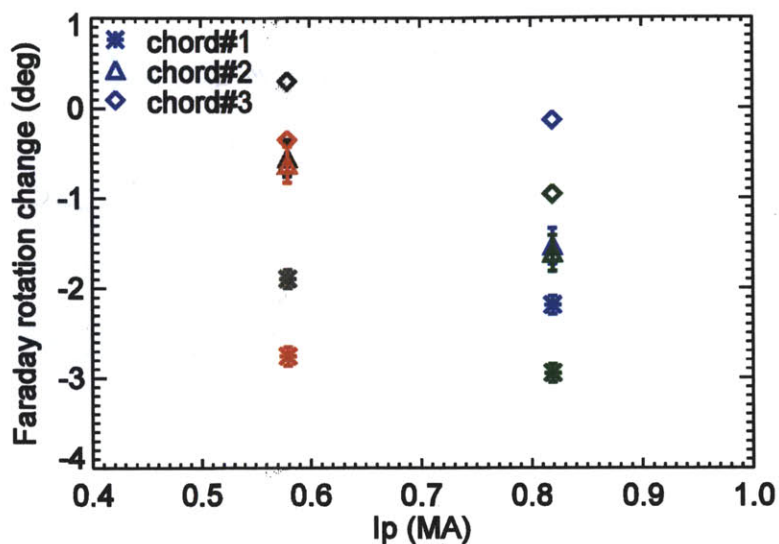


Figure 5-12: Faraday rotation changes for the four discharges in Figure 5-11. FR #1 has a significant change for both the low and high current shots, while FR #2 sees a big drop only for the high current shots ( $I_p=820$  kA).

The Faraday rotation change shows a better sensitivity to current profile changes than the loop voltage during the LHCD. Two discharges in Figure 5-13 are similar to each other with the same total current and only a small variation in density.  $V_{loop}$  looks exactly the same throughout the LH pulse. However, FR#1 drops  $\sim 1^\circ$  more for the red shot, which might be consistent with the slightly larger non-thermal ECE observations during the second half of the LH pulse.

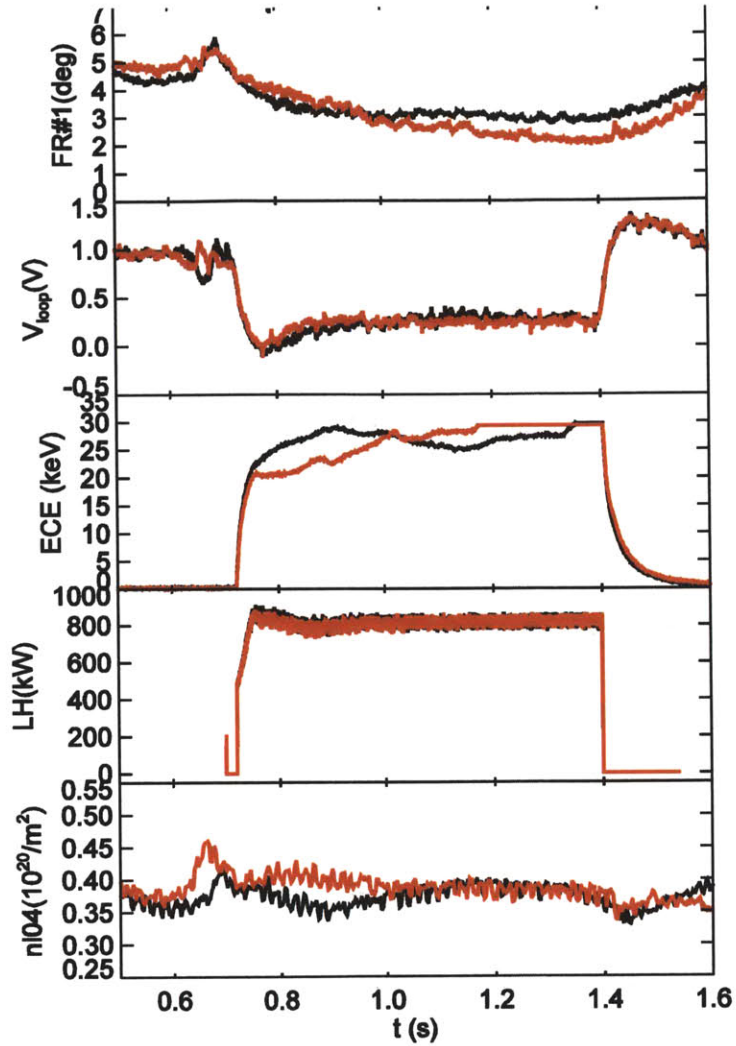


Figure 5-13: Two similar LHCD discharges. FR#1 shows a better sensitivity to the current profile changes than  $V_{loop}$ .

### 5.2.4 LH Launcher Phase Scan

In theory, LHCD efficiency is inversely proportional to  $N_{||}^2$  (Equation 1.22), so that LHCD with lower  $N_{||}$  (lower phasing) should be more efficient in driving plasma current.

Numerical simulations with GENRAY/CQL3D show LH with higher antenna phasing should drive less non-inductive current, and the power deposition should be closer to the edge[80]. Simulation results for three discharges with  $75^\circ$ ,  $90^\circ$  and  $105^\circ$  phasing (corresponding to launched  $N_{||}$  of 1.60, 1.92 and 2.24) are shown in Figure 5-14. Clearly, more LH power is

deposited close to the edge ( $r/a \sim 0.7$ ) for the shot with  $105^\circ$  phasing, and the driven current is also closer to the plasma edge.

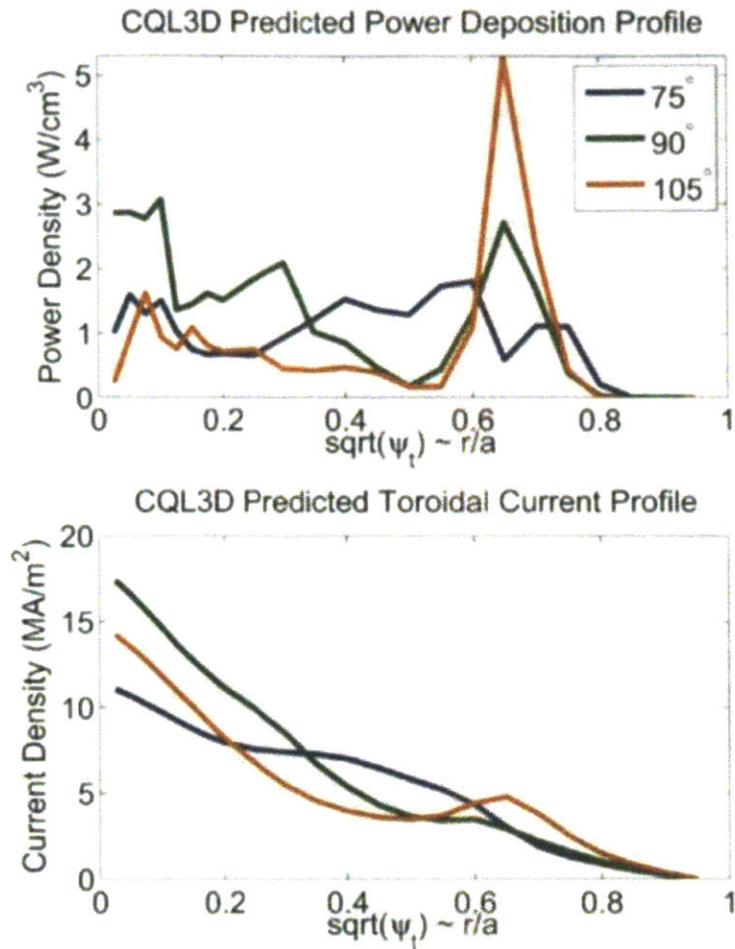


**Figure 5-14: GENRAY/CQL3D simulation shows LH deposits more power and thus more driven current close to the edge for lower antenna phasing. (Figure from [80])**

With MSE as a constraint, Kinetic-EFIT shows that the current density profiles for the discharges with lower phase LHCD were flatter than those with higher launched phase during the 2008 C-Mod campaign, as shown in Figure 5-15 [69]. However, MSE measurements did not show significant differences of the magnetic pitch angle change with shot-by-shot LH phase

scans from preliminary analysis in the 2012 C-Mod run campaign (more detailed analysis is still ongoing). One difference for the new LH phase scan results is that the plasma current was ~600 kA in 2012 compared with ~800 kA in 2008, which may contribute to different driven current density profiles as was just described.

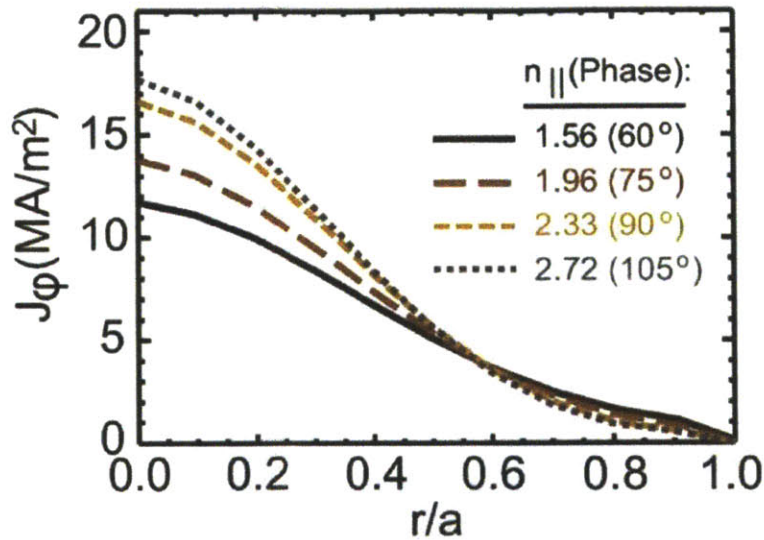


**Figure 5-15: The current density profiles flatten with decreased launched phase, as inferred from Kinetic-EFIT reconstructions with MSE constraints (Figure from [69])**

The polarimeter measurements have also been used to help understand the dependence of current drive efficiency on LH phasing. The time traces of the polarimetry measurements with shot-by-shot LH phase scans are shown in Figure 5-16. The key is to keep all the other plasma and LH parameters the same, and compare the change of FR#1 for discharges with different LH phasing (75° - black, 90° - red, 105° - blue, and 115° - green).

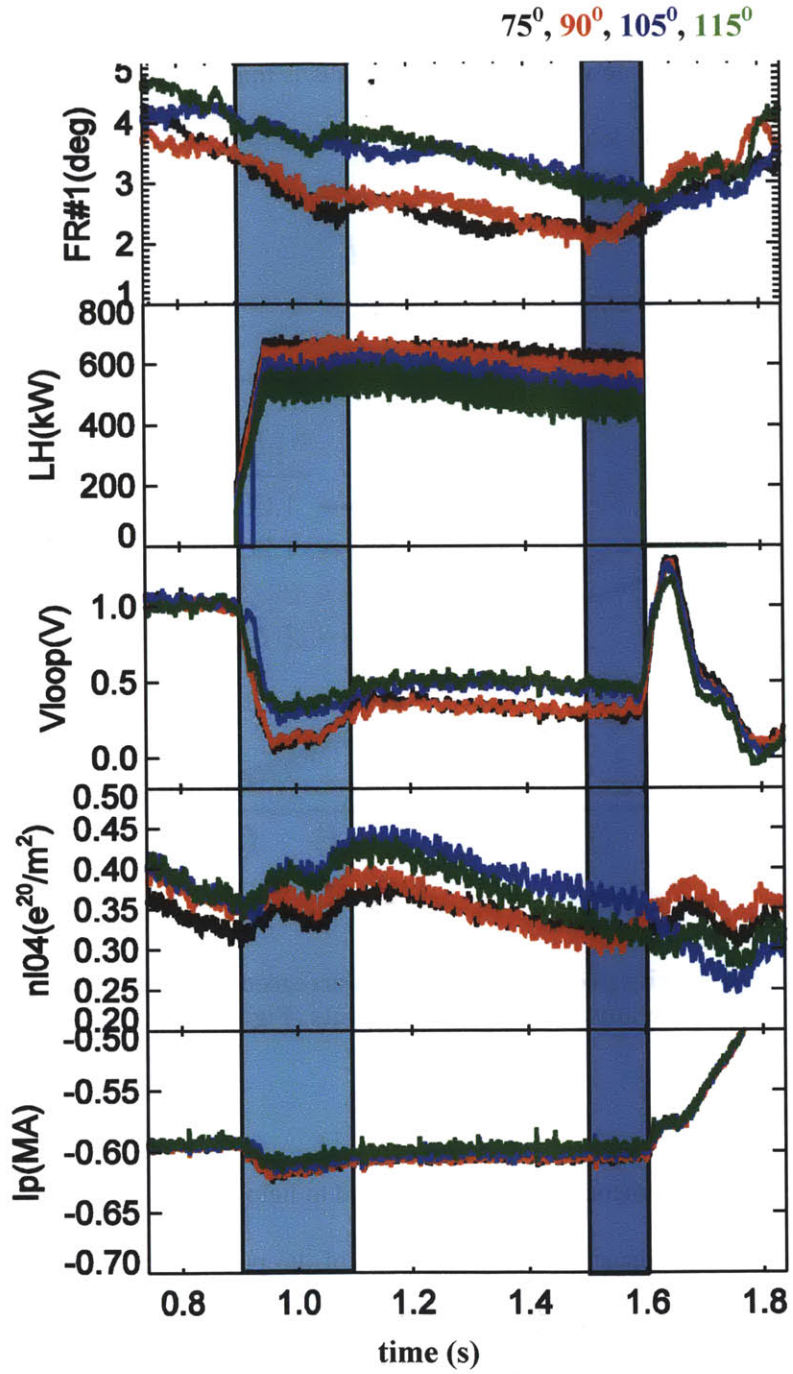
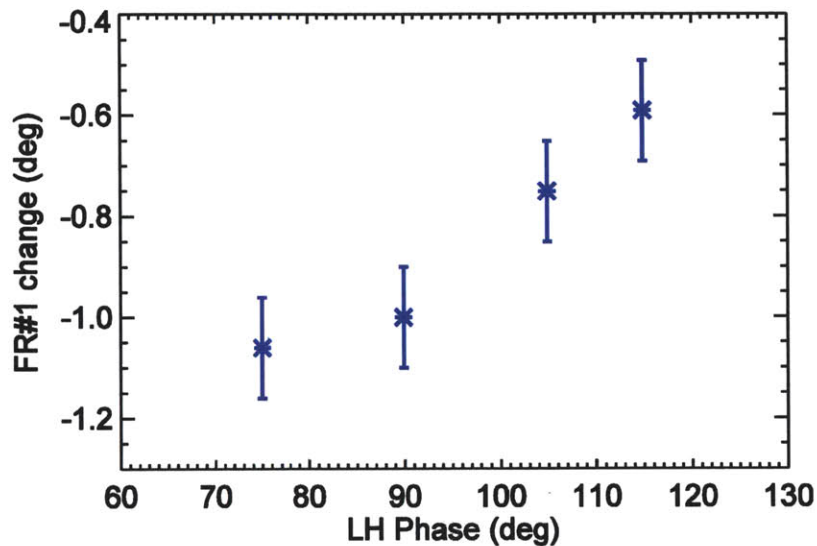


Figure 5-16: Faraday rotation on chord#1 with a shot-by-shot LH phasing scan ( 1120912017, 1120912012, 1120912021, 1120912024 with 75°, 90°, 105° and 115° phasing respectively).  $n_{104} \approx 4 \times 10^{19}/\text{m}^2$ ,  $I_p \approx 600$  kA, and LH  $\approx 600$  kW.

The FR#1 change caused by the LHCD is shown in Figure 5-17. The FR#1 change decreases with higher phasing, which agrees with the LH theory prediction. Unfortunately, we cannot simply conclude that this Faraday rotation change difference originates from LH phasing, since the density is slightly lower for two lower phasing discharges (black and red), which contributes to better current drive efficiency. To isolate the density effect, a time window of 1.5-1.6s was chosen in Figure 5-16, where density for the 115° phasing shot is similar to the 75° and 90° phasing shots. The 115° phasing shot has a higher Faraday rotation angle, which represents worse current drive efficiency.



**Figure 5-17: FR#1 change decreases with higher LH phasing, which agrees with LH theory.**

To make the comparison of LHCD efficiency with different LH phasing more robust, a phase scan was performed within a single shot, which avoids shot-by-shot differences in plasma, LH and diagnostic performance, was carried out, and the results are shown in Figure 5-18. FR#1 jumps to a sharper slope (larger time derivative) when the LH phasing decreases, even though the density slope becomes flatter throughout the LH pulse (no jump on the density slope). The linear

regression slopes of FR#1 for different LH phases are shown in Figure 5-19 (slope for phase=115° is calculated near t=1.2 s). The FR#1 slope is larger for lower phasing discharges, indicating higher current drive efficiency, consistent with the loop voltage change in Figure 5-18. Linear least squares fitting of the FR#1 slope with  $\frac{1}{n_{\parallel}^2}$  is shown in Figure 5-20. The implied current drive efficiency from FR#1 approximately linearly increases with  $\frac{1}{n_{\parallel}^2}$ , as we would expect from LH theory.

The polarimeter measurements confirm that low LH phasing (75°) is preferred for high current drive efficiency, from both the shot-by-shot and within-shot phase scans on C-Mod. These results also agree qualitatively with GENRAY/CQL3D simulations and the MSE analysis from the 2008 run campaign.

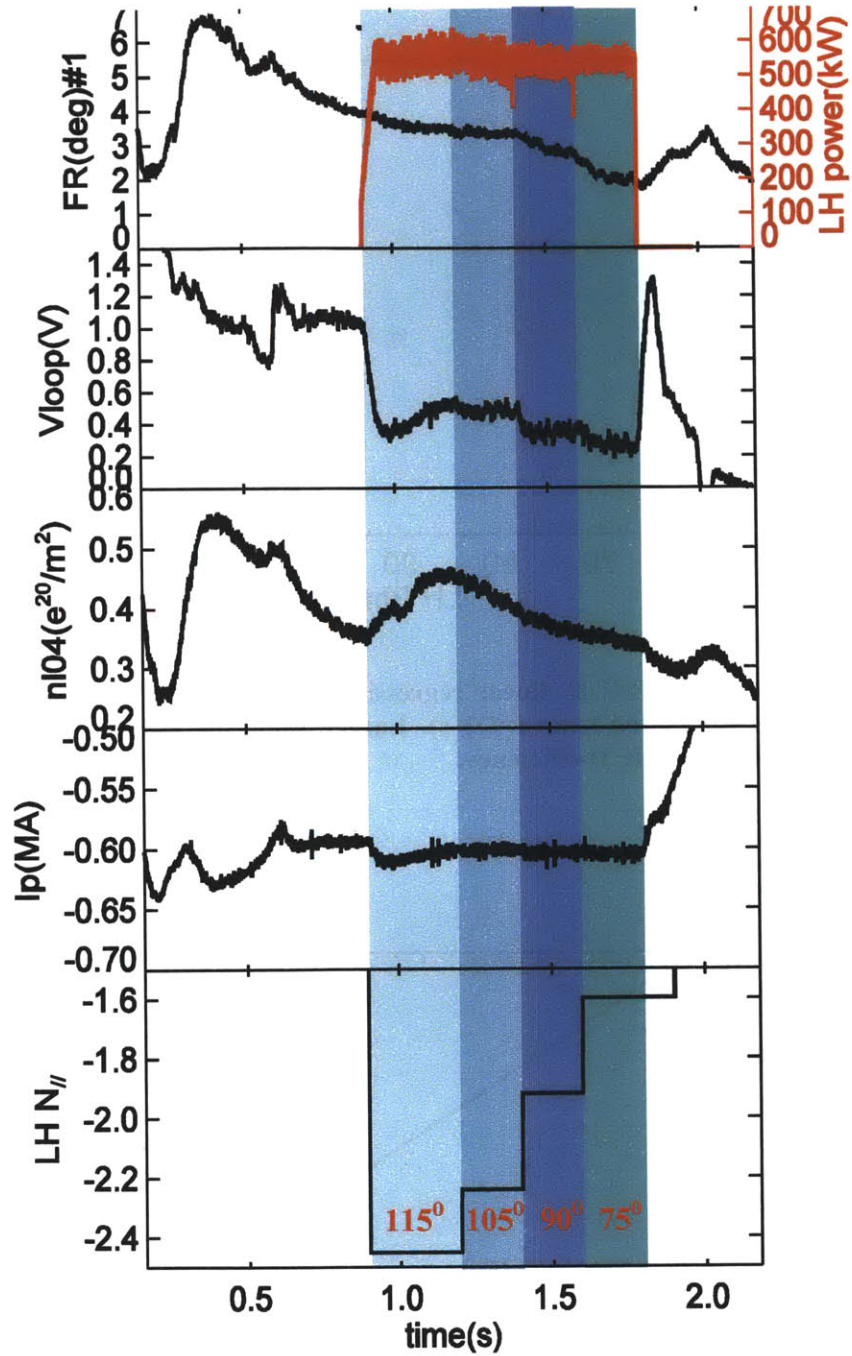


Figure 5-18: LH phase scan within one shot: 115°, 105°, 90°, 75°. The magnitude of the time derivative of FR#1 becomes larger when the LH phasing decreases.

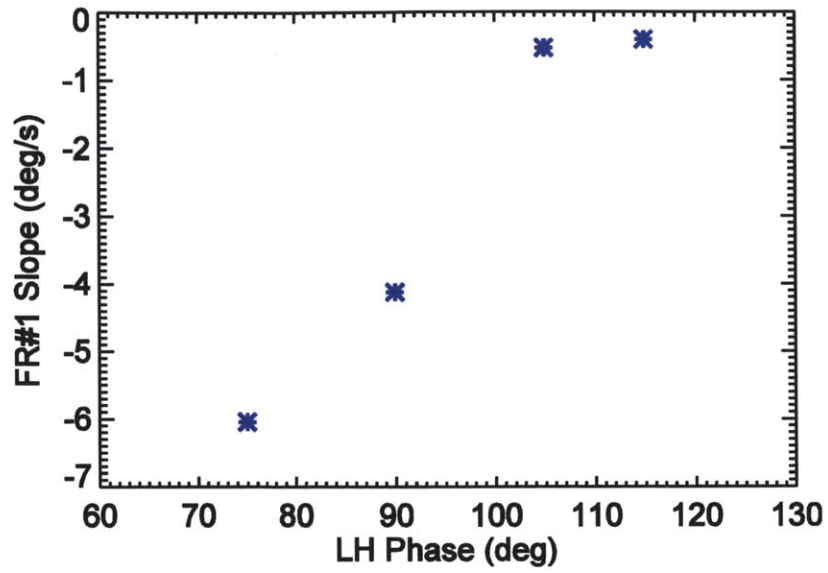


Figure 5-19: The slope of FR#1 by linear regression for different LH phases (the slope for 115° LH phasing is calculated near  $t=1.2$  s). Larger slope for lower phasing shows that lower phase yields higher LHCD efficiency.

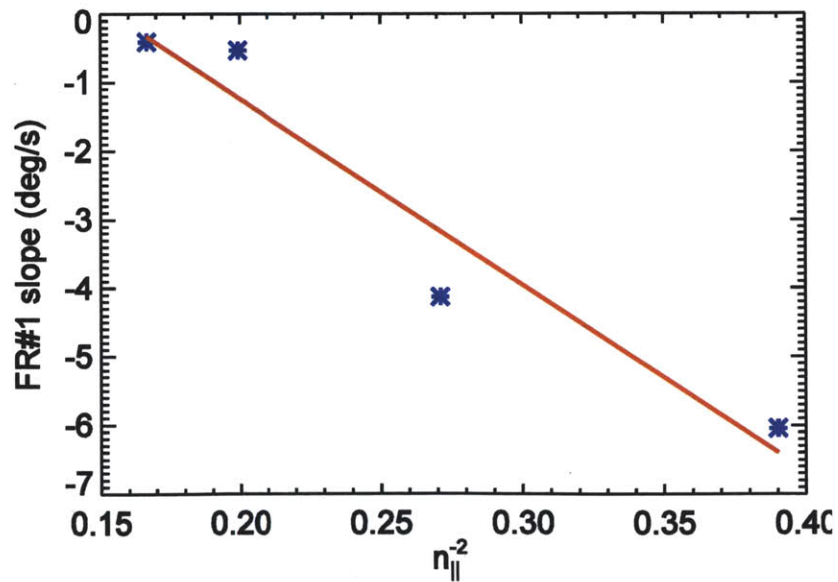


Figure 5-20: Linear least squares fitting between the FR#1 slope and  $\frac{1}{n_{\parallel}^2}$ .

## 5.3 Validate Kinetic-EFIT

### 5.3.1 Synthetic Polarimeter Signals from EFIT and TS

A synthetic polarimetry signal can be calculated by integrating the poloidal magnetic field and the electron density along the beam-paths (Equation 2.30). The poloidal magnetic field is extracted from EFIT.

There are various diagnostics that could provide electron density profile measurements. One is the interferometer, which measures the line integrated density with a fast time resolution and could be inverted to the density profile, if there are enough chords spanning over the plasma cross section. On C-Mod, TCI (introduced in chapter 1) has ten vertical chords, but focuses on the middle region of the plasma. The accuracy of the inverted density profile is not very good without edge density coverage [15]. With the addition of a third FIR laser, interferometry measurement capability could be added to the polarimeter in the future, so that we could get a direct density measurement along the polarimeter beam-path. With both FIR interferometry and TCI measurements from two different viewing directions, it might then be possible to obtain good inverted density profiles.

Very good density profiles are already provided by the Thomson scattering (TS) diagnostic (introduced in chapter 1), which is cross-calibrated with TCI. The density profile from TS is mapped to the polarimetry beam-paths using EFIT magnetic flux surface reconstructions. With a time resolution of 10 ms for TS, the synthetic polarimetry signal will have a 10 ms time resolution as well.

All of the contributions to the FIR interferometry phase changes, including the Faraday effect, the C-M effect and systematic errors due to toroidal misalignment of the beam-paths, can be estimated by integrating the density and/or related magnetic field components along the beam-paths. Detail comparisons between the EFIT predicted signals and the experimental measurements will be presented in the following section.

### 5.3.2 Faraday Rotation Measurements Compared with EFIT Prediction

Figure 5-21 and Figure 5-22 compare three-chord Faraday rotation measurements (black traces) with the synthetic polarimetry signals (red traces) generated by using normal EFIT (no internal constraints from pressure or MSE, and  $q_0$  is constrained to 0.95), for two discharges, 1120216017 and 1120216003. The EFIT predictions agree well with polarimeter measurements, especially for the first two chords. Chord#3 has the worst noise level, but within those uncertainties, shows a good match to the EFIT predictions.

A challenge for the comparisons is that the Faraday rotation measurement has a phase drift during the TF ramp, making it difficult to define a baseline, as was discussed in chapter 4. By picking the wrong baseline, for example using the flat phase before TF ramp (before -1s), we may find an offset between the measurement and the synthetic signal, estimated to be up to  $1^\circ$  for chords #1 and #2, and up to  $2^\circ$  for chord#3.

One way to mitigate the baseline drift problem is to start the TF ramp 100 ms earlier than usual, which results in a quiet baseline right before the plasma discharge is obtained (Figure 4-3). However, this method requires reprogramming the plasma control system for the discharges loaded from previous runs, and is not implemented for the discharges in this thesis.

Instead the measurement and EFIT prediction are aligned at one time-slice at an early time in the discharge. The measurement signals are typically shifted by a small phase angle, which is less than the baseline drift error. This method was not applied until phase comparisons with quiet baselines were obtained and we were confident in the accuracy of our measured Faraday rotation signals.

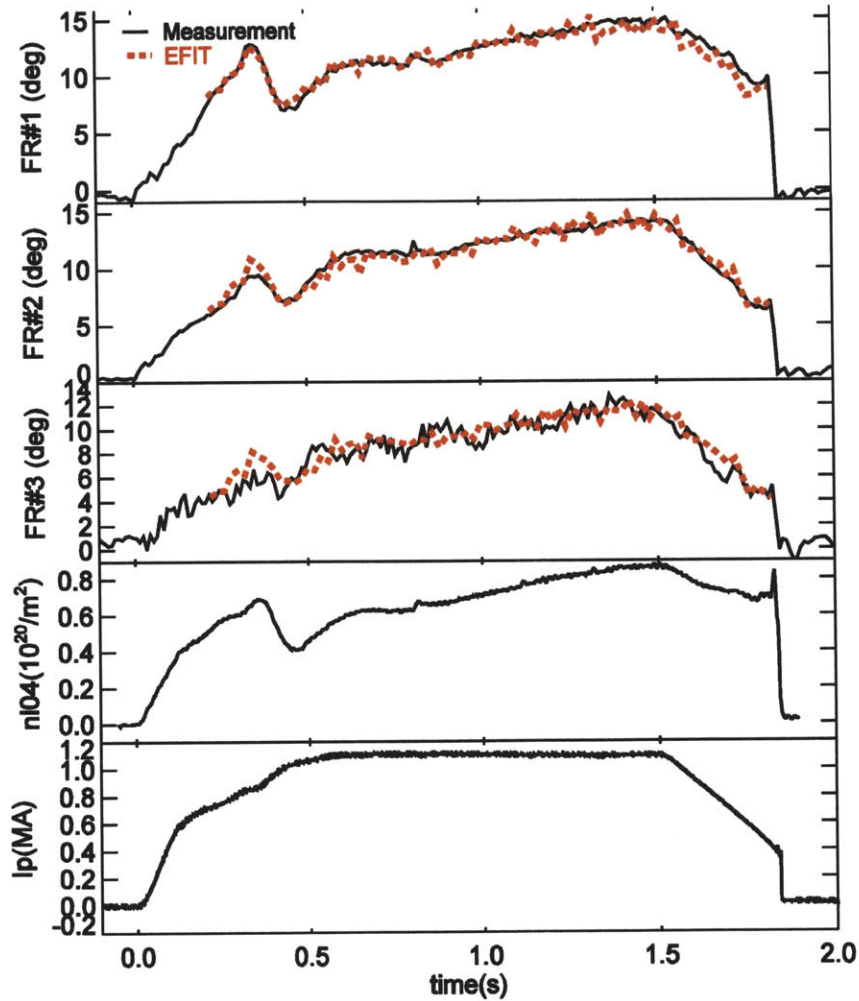


Figure 5-21: Faraday rotation measurements agree well with the synthetic signals calculated by EFIT and TS density, for all three chords. Shot 1120216017,  $I_p=1.1$  MA,  $nI04$  ramps from  $0.4$  to  $0.9 \times 10^{20}/m^2$  during the current flat top.

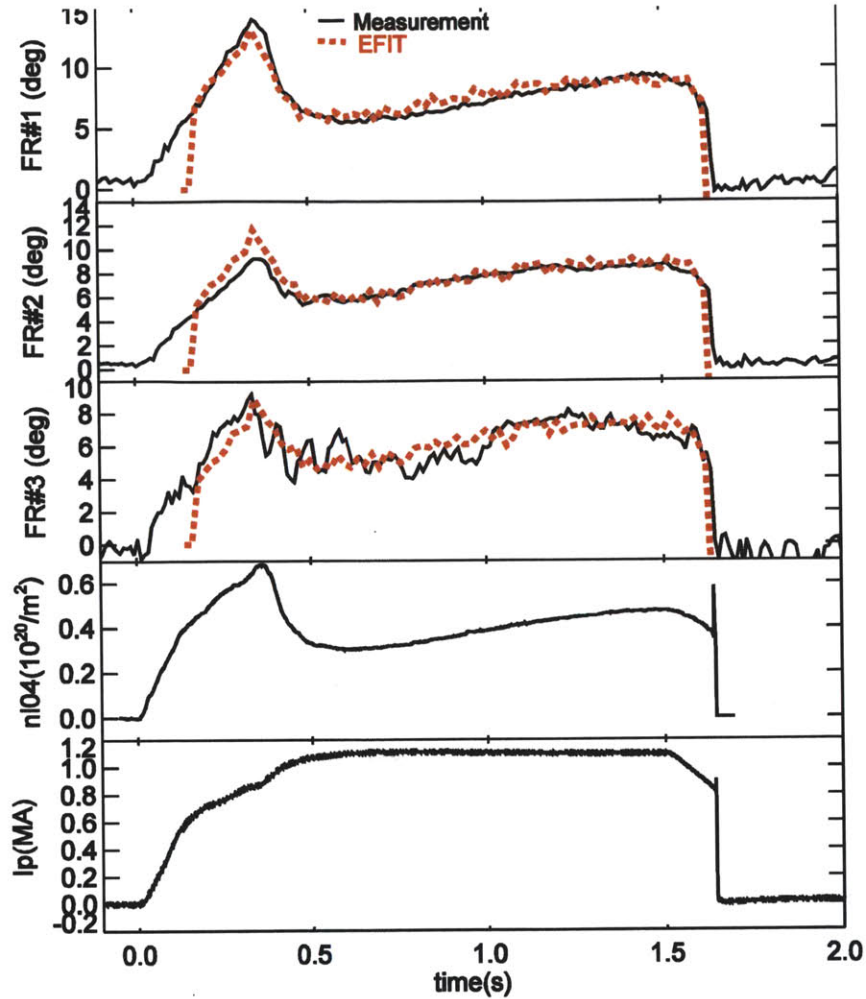


Figure 5-22: Faraday rotation measurements agree well with the synthetic signals calculated by EFIT and TS density, for all three chords. Shot 1120216003,  $I_p=1.1$  MA,  $n_{l04}$  ramps from  $0.3$  to  $0.5 \times 10^{20}/m^2$  during the current flat top.

The synthetic Faraday rotation signal is inaccurate during LHCD because of large errors in the derived internal magnetic field from normal EFIT for the non-inductive plasma. Therefore, we expect to see the measurement signals disagree with the EFIT predictions during LHCD, especially for FR#1, since it is most sensitive to the LHCD.

The time traces of a low density ( $n_{l04} \approx 0.4 \times 10^{20}/m^2$ ) LHCD discharge, with 800 kW LH power from 0.8-1.4 s, are plotted in Figure 5-23. To define a baseline for each chord, the Faraday

rotation measurements (black traces) are aligned with the synthetic signals (red traces), right before the LH pulse ( $t=0.8$  s). Then, the EFIT predictions are overlaid with the measurements for the time period before the LH pulse for all three chords. When LH turns on, the measurement and EFIT prediction for chord#1 start to separate from each other with an increasing discrepancy, evolving over the current relaxation time ( $\sim 200$  ms). This effect is sustained until the end of the LH pulse. The discrepancy decreases to zero in another current relaxation time after the LH power is turned off. A similar trend is observed on chord#2, while there is no obvious LH effect on chord#3. The observed discrepancy between measurements and synthetic signals confirms that the reconstructed internal poloidal magnetic field from the normal EFIT is not accurate during LHCD, which should be improved by incorporating the polarimetry data into EFIT as an internal constraint. Similar results have been observed on dozens of other discharges with good LHCD. One more discharge is shown in Figure 5-24, with  $n_{l04} \approx 0.45 \times 10^{20}/\text{m}^2$  and  $I_p \approx 600$  kA.

In Figure 5-25, another synthetic polarimetry signal is produced by Kinetic-EFIT (blue squares), which includes internal constraints provided by the plasma pressure and MSE pitch angles. Its time resolution is 100 ms, since the MSE data are averaged to improve the SNR. The Faraday rotation measurement agrees well with the prediction from Kinetic-EFIT for all three chords, and the discrepancy is much smaller than that from the normal EFIT. Therefore, the polarimeter confirms that the Kinetic-EFIT captures a more accurate representation of the current profile than normal EFIT during the LHCD.

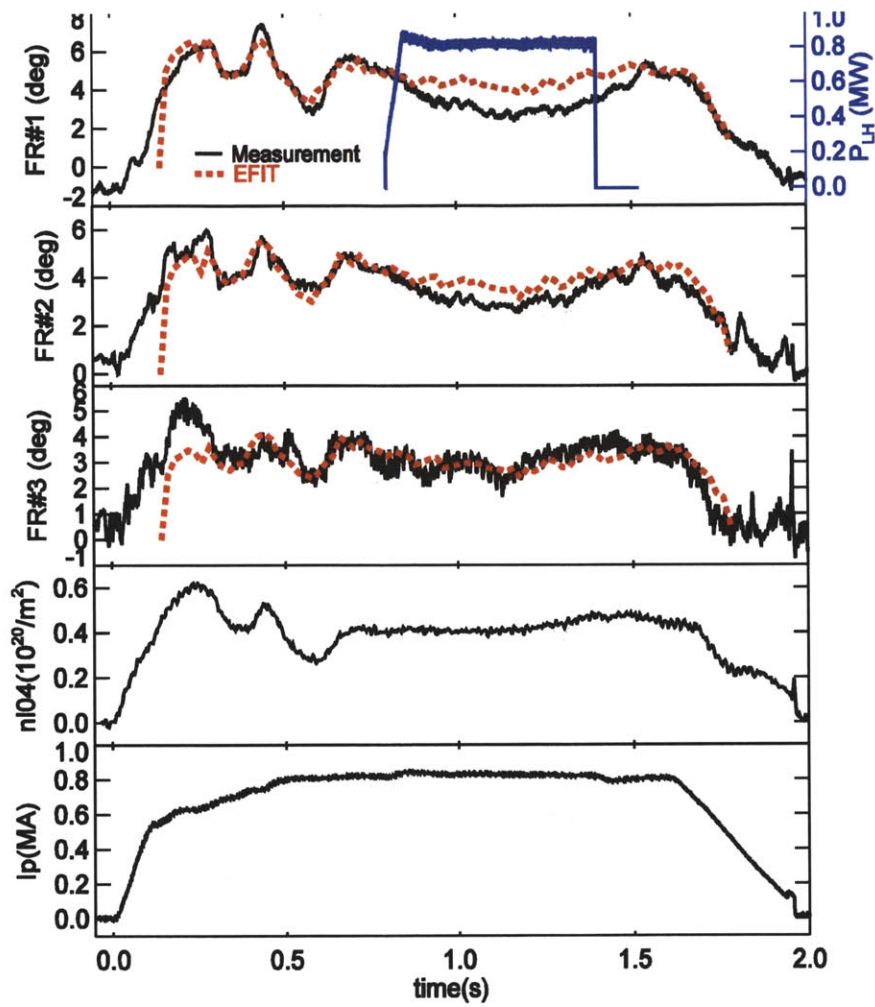


Figure 5-23: Comparison between the measurements and the EFIT predictions for a LHCD discharge. FR#1 shows a big discrepancy between two traces, which confirms the poloidal magnetic field from normal EFIT is inaccurate during LHCD .

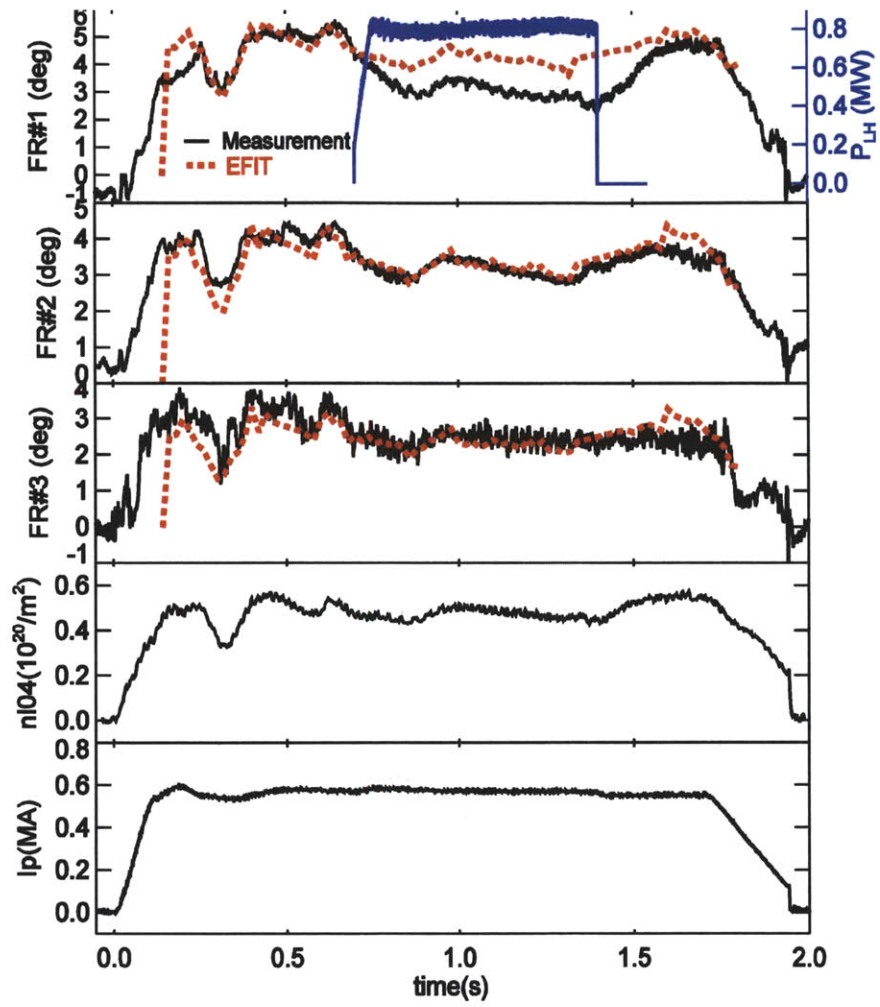


Figure 5-24: Comparison between the measurements and the EFIT predictions for a LHCD discharge. The FR#1 shows a big discrepancy between two traces.

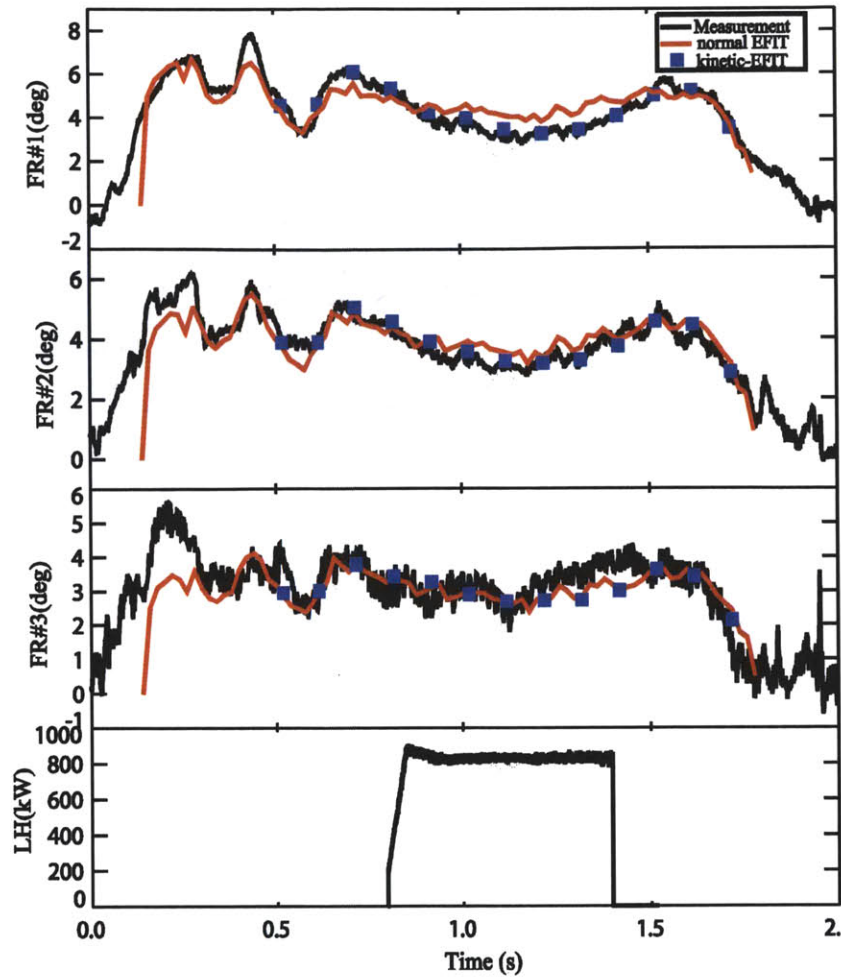


Figure 5-25: Faraday rotation agrees with the prediction from Kinetic-EFIT (blue squares, 100 ms resolution). The discrepancy between measurement and Kinetic-EFIT prediction is much smaller than that from the normal EFIT during the LH pulse.

### 5.3.3 C-M Measurements Compared with EFIT Predictions

Most polarimetry systems are operating in parameter regimes with negligible Cotton-Mouton (C-M) effect. However, on machines with high TF, such as ITER and C-Mod, there is a concern that the C-M effect can be significant in the poloidal measurement geometry and may affect the Faraday measurements, which might make it difficult to measure either of the effects. This concern need to be addressed, if we would like to implement a poloidal viewing polarimetry system on ITER or other high field, high density tokomaks. One method that has been tried is to

use linearly polarized beams to measure the Faraday and C-M effect simultaneously, such as has been implemented on JET [83]. The other way is to mitigate the C-M effect on the Faraday rotation measurements by using the Dodel-Kunz method [35]. Alcator C-Mod, with toroidal magnetic field up to 8 T, provides an excellent platform to assess if the C-M effect on the Faraday rotation can be eliminated down to an acceptable level by using the Dodel-Kunz method. Shot-by-shot TF scans, while keeping other parameters unchanged, were carried out on C-Mod. Section 4.2 presents discharges with different TF, and the Faraday Effects are similar, which means the C-M effect does not contaminate our measurements at the current noise levels.

On C-Mod, the Faraday rotation measurements can be easily converted to C-M measurements by removing the quarter-wave plate. In this way, the probe detector measures the phase difference between two orthogonal linear polarized beams, which represents the phase delay between O-mode and X-mode, which is precisely the C-M effect. In Figure 5-26, chord#1 was set up to measure the C-M effect. Although the C-M measurement (black curve in the first frame) is noisier than the polarimetry measurement, it agrees reasonably well with the EFIT projection (red curve). Chord#2 still measures the Faraday effect (second frame), which agrees with the EFIT projection as well. A combined polarimetry/C-M system could be an alternative option to a polarimetry/interferometry system to realize simultaneous density/current profile measurements, since the C-M has the advantage of having no fringe jump issues, which can be an issue for interferometry. Such a system would require only two FIR lasers, rather than the three required for a polarimetry/interferometry system.

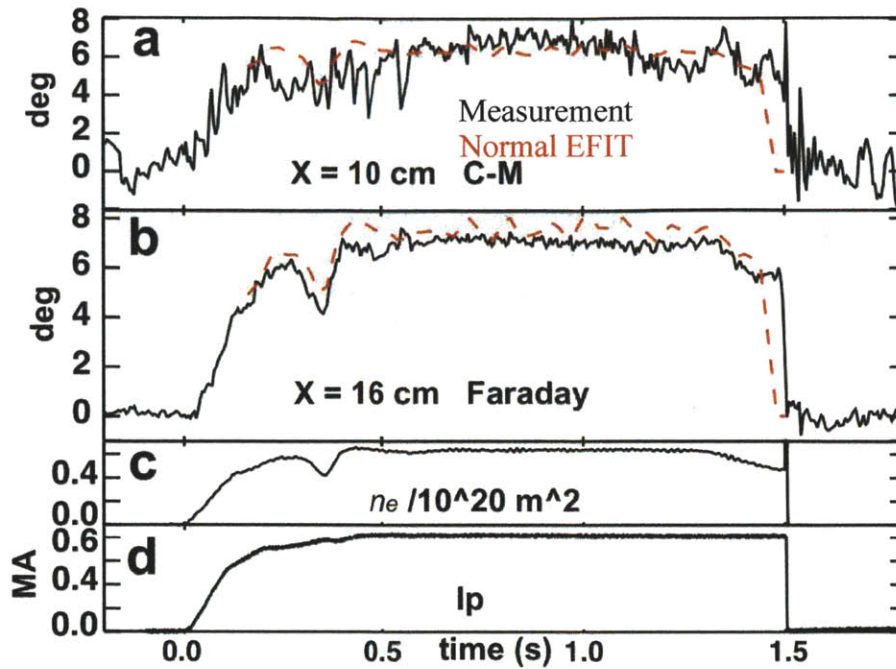


Figure 5-26: a) C-M effect measurement (black) with the EFIT prediction (red); b) Faraday effect measurement (black) with the EFIT prediction (red). Agreement is reasonably good for both C-M and Faraday effects.

## 5.4 Incorporating Polarimeter Data into EFIT to Constrain $q_0$

Since the MSE constrained kinetic-EFIT only has a time resolution of 100 ms, developing a polarimetry constrained EFIT with a much faster time resolution is critical for diagnosing the evolution of the current density profile and controlling the  $q$ -profile in real time, as successfully tested on JET [84][85][86].

Incorporating the polarimeter data into the EFIT equilibrium reconstruction is complicated, since the polarimetry signals are line integrations and they depend on both the density and magnetic field along the beam path. Our first attempts to incorporate the polarimetry measurements into equilibrium reconstruction focused on optimizing the  $q_0$  constraint. Reproducing  $q_0$  with a good accuracy is very difficult in EFIT without internal constraints. Thus,

normal EFIT is usually run assuming that  $q_0$  is about 0.95. Although this is probably a reasonable assumption for many sawtoothed C-Mod discharges, it is certainly not correct with strong off-axis LHCD. In Figure 5-27, there is a  $\sim 1.5^0$  discrepancy between the polarimeter measurement (black curve in 3rd frame) and the normal EFIT prediction (blue curve) for FR#1 during LH. By allowing  $q_0$  to become a free parameter, the synthetic Faraday rotation from the modified EFIT comes into good agreement with measurement (green curve).

The methodology is to scan the  $q_0$  and minimize the following equation

$$S_{err} = \sum_{i=1}^3 \left( \frac{\alpha_i - \alpha_i^*}{\Delta\alpha_i} \right)^2 \quad (5.2)$$

where  $\alpha_i$  is the Faraday rotation for chord#i,  $\alpha_i^*$  is the EFIT predicted Faraday rotation after tuning  $q_0$ , and  $\Delta\alpha_i$  is the typical RMS error associated with the measurement of  $\alpha_i$ . The optimized  $q_0$  is found to be  $\sim 2$  with the single chord polarimetry constraint (FR#1).

The plasma stored energy, obtained in three different ways, is compared in the bottom frame of Figure 5-27. The green trace is calculated using the polarimetry-constrained EFIT, the blue trace is from normal EFIT, and the red trace is based on the total kinetic energies of the plasma electrons and ions. We use the electron density and temperature from TS measurements. The ion temperature is assumed to be same as the electron temperature. The ion density profile is calculated with effective ion charge ( $Z_{eff}$ ) by assuming the same profile as the electrons. The stored energy drops to zero using normal EFIT, which is clearly incorrect. Polarimetry EFIT shows larger stored energy during the LHCD, and is closer to the kinetic energy than the normal EFIT.

Three time-slices of the current density and q profiles from polarimetry-constraint EFIT are shown in Figure 5-28. The red curves are profiles before the LH ( $t=0.6$  s), when  $q_0 < 1$ . With the LHCD, the current is significantly flattened and  $q_0 > 1$  at  $t=1.2$  s (blue), which are consistent with the off-axis current drive and the time at which the sawteeth disappear. After turning off the LH at 1.4 s, the current profile slowly peaks and  $q_0$  drops at  $t=1.5$  s (green curves).

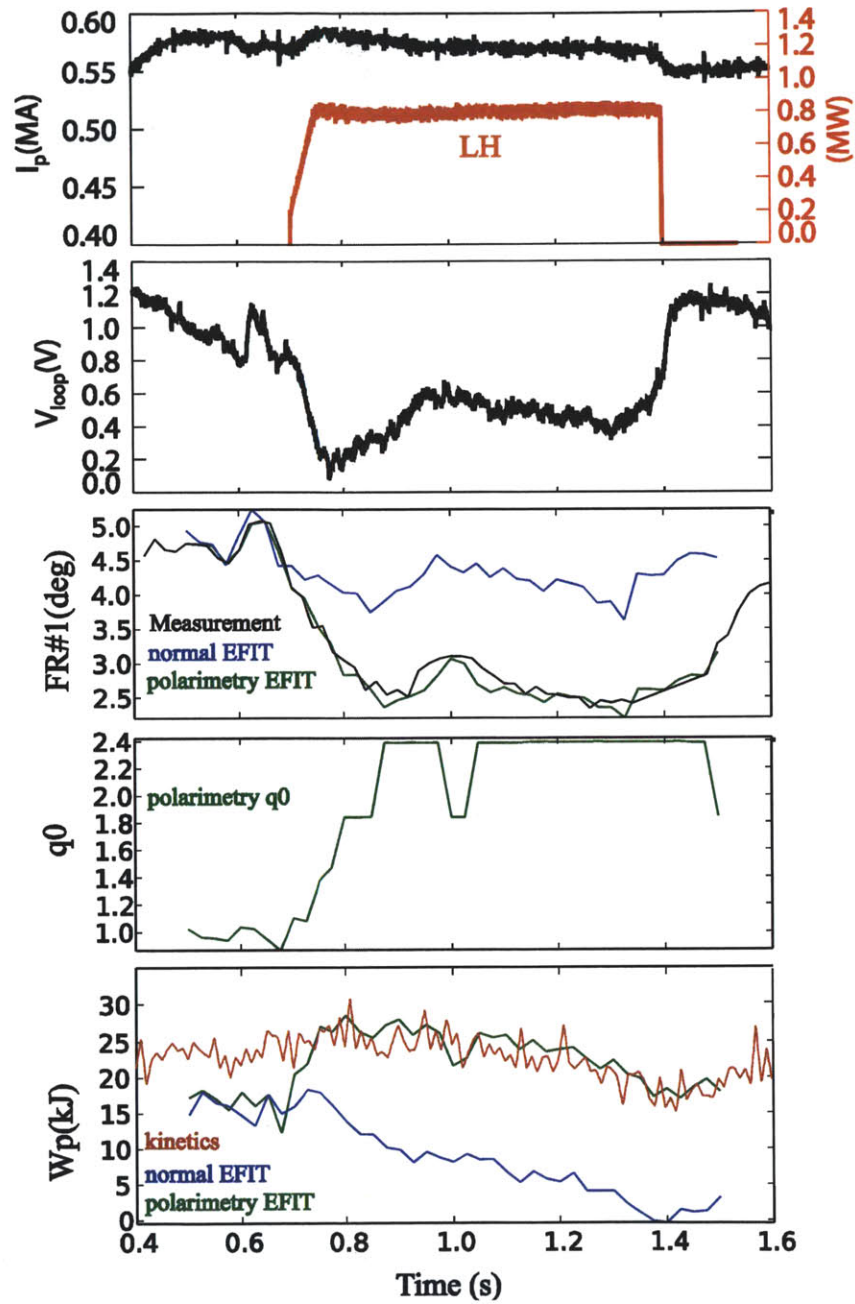


Figure 5-27: Large differences are observed between measurement (black curve in 3<sup>rd</sup> frame) and normal EFIT prediction (blue curve) for  $FR\#1$  during LHCD.  $q_0$  was chosen to minimize the difference between the measurements and EFIT predictions (green curve).

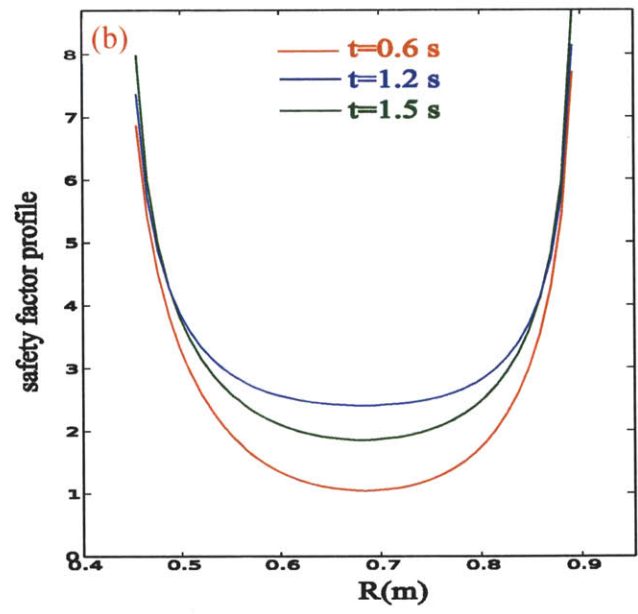
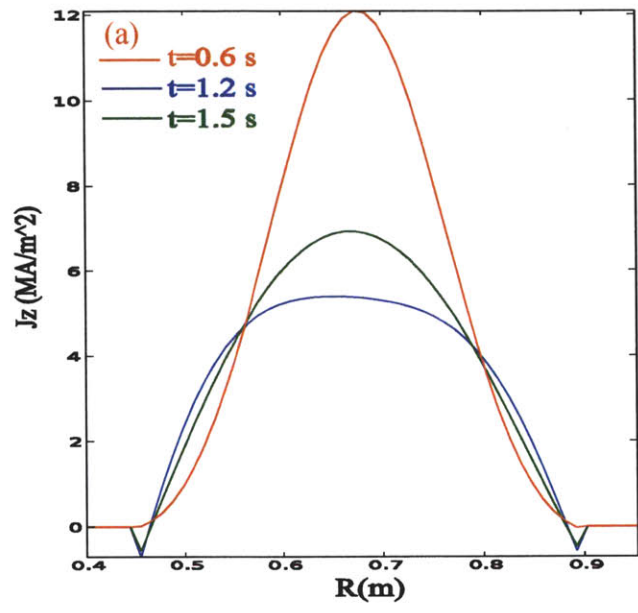


Figure 5-28: Current density (a) and safety factor (b) profiles for three time-slices, before the LH at  $t=0.6$  s (red), during the LH at  $t=1.2$  s (blue) and after the LH at  $t=1.5$  s (green).



## 6. Polarimetry Measured Fluctuations

Measuring the internal magnetic fluctuations is essential for understanding plasma transport and improving plasma confinement. The newly developed polarimetry system with a relatively wide bandwidth (2MHz) compared to polarimetry systems on most of the other machines in the world is capable of measuring broadband internal magnetic fluctuations, which are not measurable by other existing fluctuation diagnostics on C-Mod.

The measured Faraday rotation signal depends on both the plasma density and magnetic field, and we can rewrite each variable as a sum of the equilibrium and fluctuating components:  $\alpha = \alpha_0 + \delta\alpha$ ,  $n = n_0 + \delta n$ , and  $B = B_0 + \delta B$ . Therefore, the fluctuating Faraday rotation signal includes three terms,

$$\delta\alpha = c_f \lambda^2 (\int \delta n B_0 \cdot dl + \int n \delta B \cdot dl + \int \delta n \delta B \cdot dl) \quad (6.1)$$

where the first term is the density fluctuation weighted by the equilibrium magnetic field along the beam-path, the second term is the magnetic fluctuation along the beam-path weighted by the equilibrium density, and the third term is a negligible higher order quantity (both  $\delta n$  and  $\delta B$  are small). Since the polarimeter measures the integral of the product of the density and magnetic field, it is nontrivial to extract either type of fluctuation or locate the position of the fluctuations with only three-chord measurements of available in the current system.

In the 2012 C-Mod run campaign, the three-chord polarimetry system was used to measure fluctuations associated with various MHD instabilities, fast-particle driven modes, and broadband turbulence, including a wide frequency range from ~5 to 800 kHz, and with a good signal-to-noise ratio. With the difficulty of separately extracting the magnetic or density fluctuation components from the mixed polarimetry signals, the underlying physics has not yet been thoroughly studied. In this chapter, we will briefly discuss the polarimetry fluctuation measurements. Detailed physics analysis could follow with future experiments, especially if the

system were upgraded to six horizontally viewing chords with at least one chord through the magnetic axis.

Section 6.1 presents fluctuations measured with the polarimetry system during EDA H-mode [87][88] discharges. These fluctuations are found to be altered with LH waves. The quasi-coherent mode (QCM) drifts down in frequency and the broadband fluctuations first observed by the polarimeter are suppressed during LH. A shot-by-shot LH power scan shows that the change of the fluctuations clearly begins when the LH power is higher than 500 kW, and then scales with the LH power.

Section 6.2 presents polarimetry fluctuations for I-mode [89][90] plasma, including the weakly coherent mode (WCM) [89][90][91] and neo-classical tearing modes (NTMs) [92]. Three polarimetry chords confirm the poloidal asymmetry of the WCM, previously discovered by fast magnetic coils [10].

## **6.1 LH Waves Alter Fluctuations during EDA H-mode**

H-mode means high-confinement mode, compared to the traditional low-confinement mode (L-mode) [93]. With a transport barrier formed near the plasma edge, H-mode enhances both energy and particle confinement, and forms steep density and temperature gradients just inside the LCFS. Auxiliary heating with ICRF is usually necessary to transition the plasma from L-mode to H-mode on C-Mod. There are three different kinds of H-modes on C-Mod, ELM-free H-modes [87], ELMy [87][94][95] and EDA H-modes. The EDA H-mode, which is named for the enhanced  $D_{\alpha}$  signals, can last for more than ten times the energy confinement time, and the duration is primarily limited by the length of the ICRF pulse, increased impurity levels or injections.

Fluctuations in EDA H-mode, as measured by the polarimeter, are shown in Figure 6-1(a). A QCM at  $\sim 100$  kHz is observed on all three chords, which is consistent with PCI [10][96] and reflectometry measurements, as shown in Figure 6-1(b). This mode is already well

studied with a 3D edge fluid code BOUT (BOUT++) [97][98] and extensive experiments on C-Mod [99][100]. It is recognized to be a localized mode near the edge plasma density gradient region (pedestal), and is identified as responsible for enhanced outward impurity transport across the barrier region, which results in long pulse stability, and is unlike ELM-free H-modes, which are usually transient because of impurity accumulation. The QCM was believed to be related to resistive ballooning mode instabilities [101], but there is new experimental evidence on C-Mod suggesting that the QCM is an electron drift-Alfven wave [102]. Three polarimetry chords crossing the pedestal at different locations and with different angles all see very similar QCM activity, which confirms that there is no evidence of a poloidal asymmetry in the location of the QCM from Magnetics measurements.

In addition, broadband fluctuations are observed in 200-600 kHz range by the polarimeter. This mode has smaller amplitude, and is much broader and upshifted in frequency compared to the QCM. It appears on chord#1 and #2, but not on the edge chord, which indicates that the broadband fluctuations are core fluctuations. Also, the fluctuations in this frequency range are not observed by the reflectometer or PCI, which are sensitive only to density fluctuations. From these initial measurements, one possible conclusion is that the broadband fluctuations are core magnetic fluctuations. Since the probing FIR laser beams have a diameter  $D \approx 1.5$  cm in the plasma, the polarimeter should measure fluctuations with a wavenumber of up to  $k_{polar} \approx \frac{2\pi}{D} \approx 4.2/\text{cm}$ . Therefore, it is also possible that the broadband fluctuations are density fluctuations but with a wave-number outside of the range that PCI (1-15/cm) [103] is most sensitive to. From these observations, we confirm that the polarimeter can make low phase noise measurements of small amplitude perturbations.

LH power ( $P_{LH}=650$  kW) significantly changed both the QCM and broadband fluctuations, as shown in the spectrograms in Figure 6-2(a). The LH power is applied from 0.92 to 1.25 s, during the EDA H-mode. The QCM downshifts from  $\sim 120$  to 60 kHz, and becomes

more coherent during the LH pulse. This phenomenon also appears on the PCI, reflectometer and Gas Puff Imaging (GPI) [10][104] measurements.

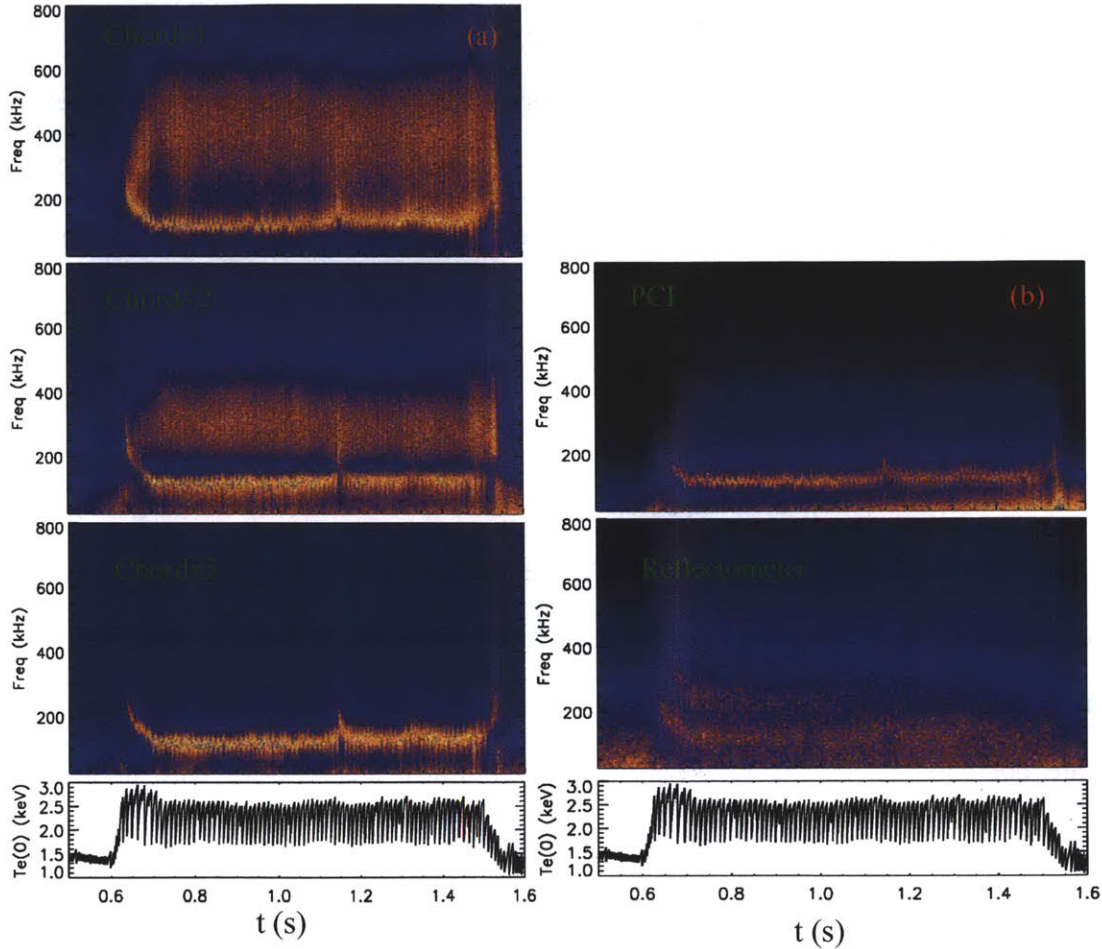


**Figure 6-1: (a) Three-chord polarimetry fluctuation measurements with the EDA H-mode. Polarimetry observed QCM mode is consistent with PCI and reflectometer measurements in (b). Higher frequency broadband fluctuations are only found on core channels (#1, #2). (b) QCM on PCI and reflectometer signals. A second order harmonic of the QCM is shown on reflectometer.**

The fluctuation intensity, integrated over 250-600 kHz is shown as a function of time in Figure 6-2(b). It significantly drops when LH turns on for both chord#1 and #2 and rises when LH turns off. The line-averaged density decreases  $\sim 10\%$  during the LH (a similar change in the core density is seen with TS), which partially explains the reduction of the core magnetic

fluctuations, since the polarimetry magnetic fluctuation component is weighted by electron density. The core rotation from the High Resolution X-ray Spectroscopy (HIREX) [105][106] measurements increases during LH, as shown in the sixth frame of Figure 6-2(b). The higher rotation shear may suggest a higher ExB shear, which stabilizes the core turbulence and explains the suppression of the broadband magnetic fluctuations [107][108]. The broadband fluctuations are correlated with sawtooth events, as sawtooth crashes are clearly seen on the integrated power signals of chord#1 and chord#2.

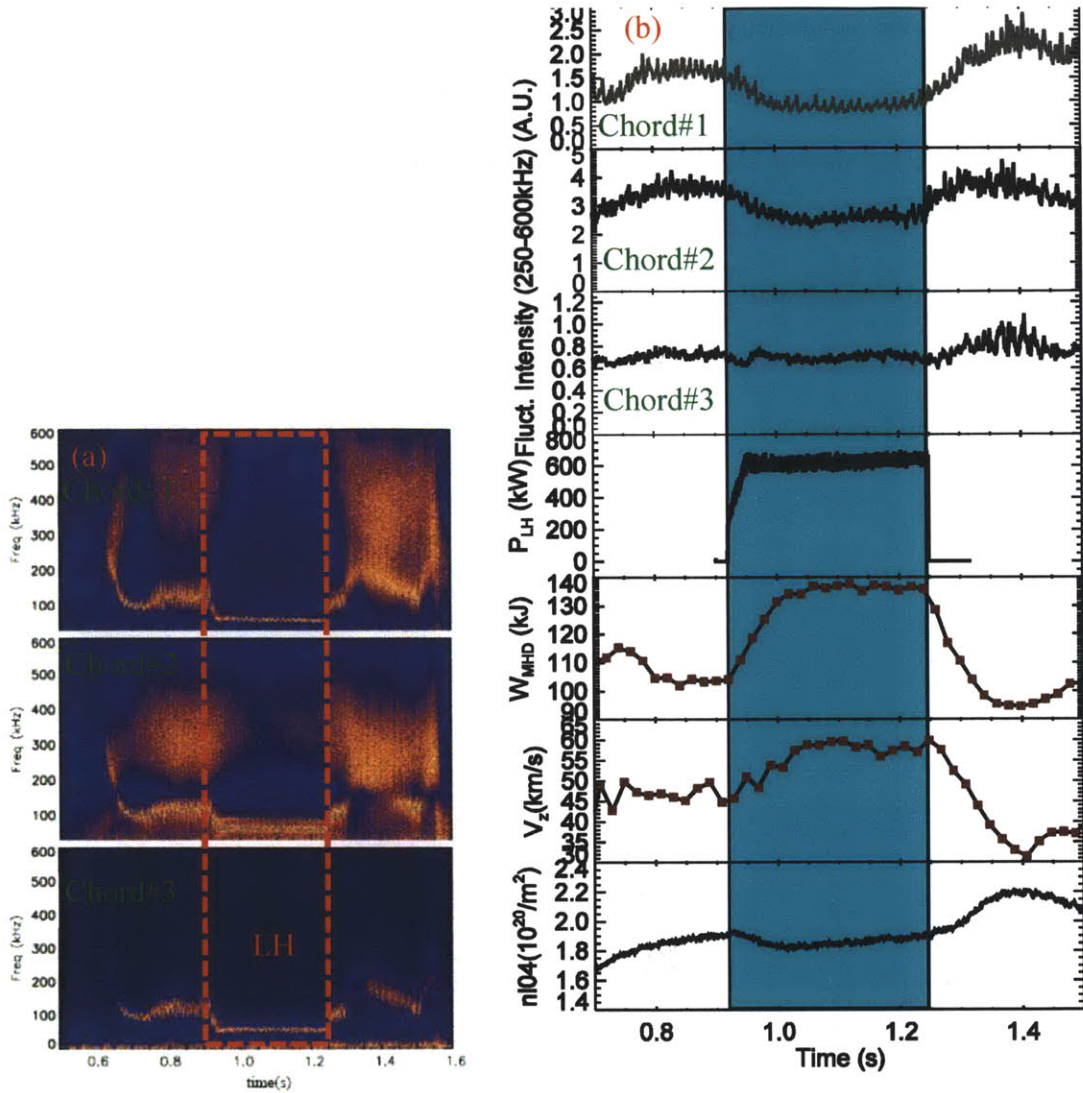


**Figure 6-2: (a)** With 600 kW LH applied during the EDA H-Mode, the QCM drifts down in frequency and becomes more coherent. **(b)** The fluctuation intensity integrated over 250-600 kW is reduced with LH. Sawtooth crashes are seen on the integrated fluctuation intensity. The plasma stored energy from EFIT and the core toroidal rotation increase, and the line averaged density decreases, during the LH.

To determine if the LH effects on EDA H-mode fluctuations scale with LH power or not, a shot-by-shot LH power scan was done. Figure 6-3 shows polarimetry fluctuations (chord#1) for four shots with LH power from 0 to 600 kW. In (a), the QCM and the broadband turbulence are continuous throughout the whole EDA H-mode. In (b), there is still no obvious change on the fluctuations with 300 kW LH power. When the LH power is increased to 500 kW, a down shift in

frequency for the QCM, and suppression of the broadband fluctuations appear in (c). This phenomenon is more significant with higher LH power, at 600 kW in (d). The broadband fluctuation intensity decreases with the LH power (300-600 kW) as shown in Figure 6-4.

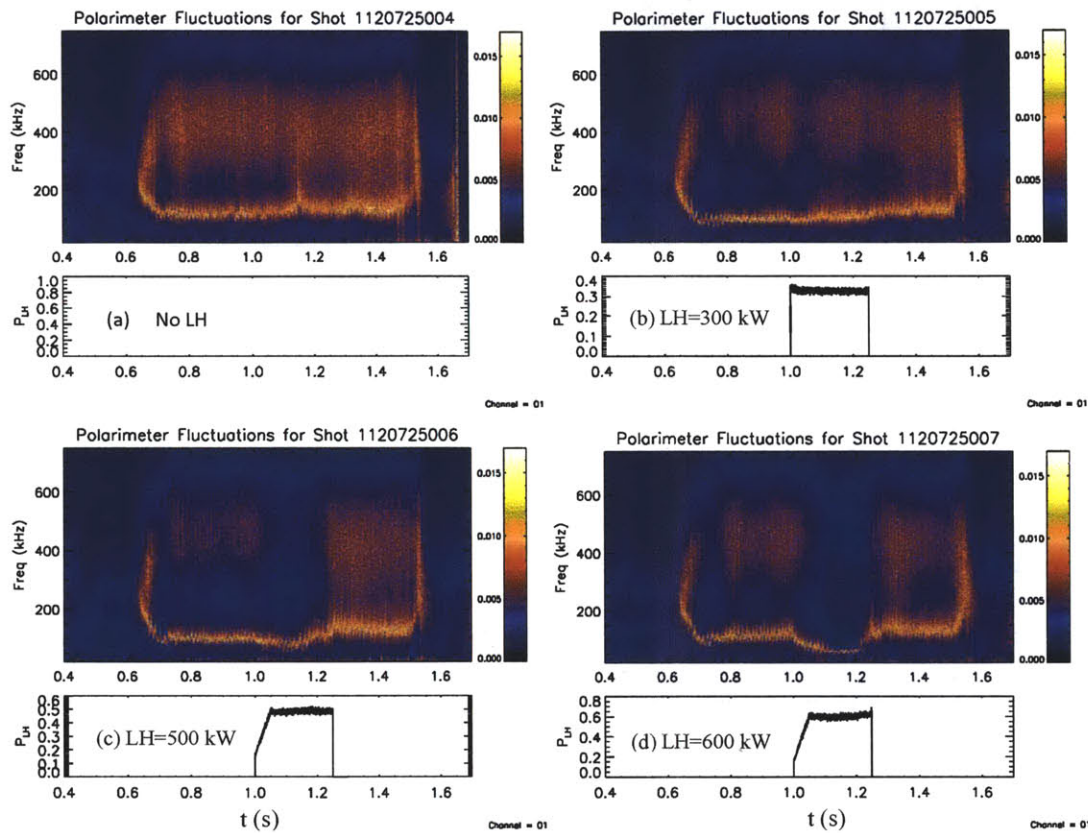


**Figure 6-3: LH power scan for four discharges(0, 300, 500 and 600 kW). As the LH power is increased, so too does the downshift in frequency for the QCM mode, while the broadband fluctuations decrease.**

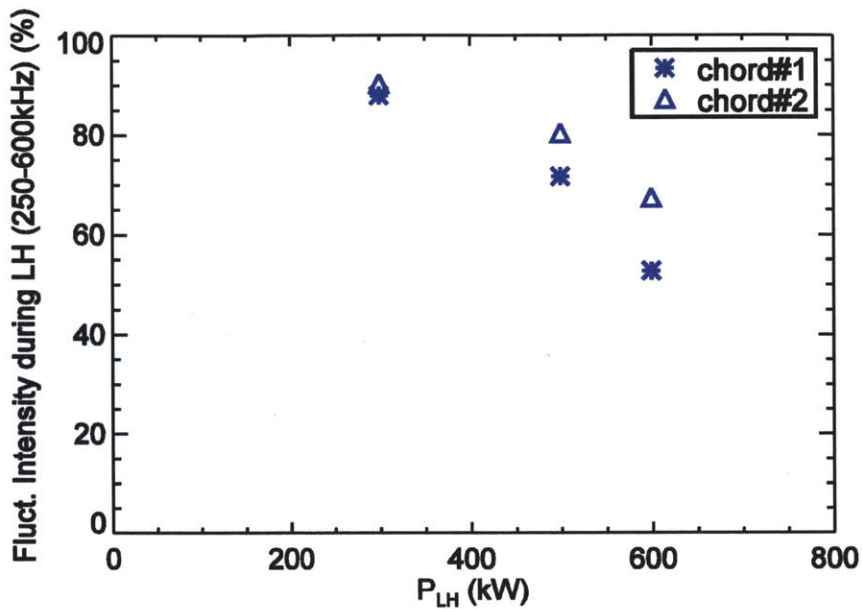


Figure 6-4: The broadband fluctuation intensity (integrated over 250-600 kHz) decreases as the LH power is increased.

## 6.2 I-mode Fluctuations

I-mode is a recently explored plasma operating regime on C-Mod [89][90]. It has good energy confinement, similar to H-mode, and particle confinement similar to L-mode. Its outward impurity diffusion is larger than H-mode, so there is less of an impurity accumulation problem. I-mode can be run in a stationary manner, since it does not need edge localized modes (ELMs) to suppress the core build-up of impurities. Fluctuations for I-mode plasmas have been thoroughly analyzed with some diagnostics on C-Mod. The new polarimetry system also observes fluctuations during I-mode, such as WCM [89][90][91] and NTMs [92], and its measurements will contribute to I-mode physics research on C-Mod.

Polarimeter fluctuations for a steady I-mode are shown in Figure 6-5. When the confinement transitions to I-mode, at  $t \approx 0.8$  s, the broadband fluctuations are reduced, while another higher frequency ( $\sim 300$ -500 kHz) mode appears on chords #2 and #3. This mode is called the Weakly Coherent Mode (WCM), as it is broader in frequency than the QCM. The

WCM is strongest on chord#3 and is almost invisible on chord#1. Thus, there is a poloidal asymmetry for the WCM, with increased fluctuation amplitude away from the mid-plane, which is consistent with previous fast magnetic coil measurements [91][109].

If we check a lower frequency region, from 20 to 50 kHz, NTMs are observed in the polarimeter signals (Figure 6-6). NTMs are resistive tearing mode islands that are sustained by a helically perturbed bootstrap current. They have been frequently observed in I-mode plasmas on C-Mod, and are usually triggered by large sawtooth crashes [92]. The NTMs are mainly studied using edge magnetic coil measurements. The magnetic coils observe intense NTMs in the 30 to 45 kHz frequency band (top frame), which clearly correlate with sawtooth crashes shown in the core temperature signal (bottom trace). The polarimeter finds NTMs in the same frequency range. Chord#1 observes both 45 and 30 kHz NTMs, though they are weak. Chord#2 only detects 30 kHz NTMs, similar to the observation from the PCI measurements.

There are other fluctuation modes observed by polarimetry, such as energetic particle driven mode during ICRH (200-400 kHz), snakes (5-20 kHz) and potential Alfvénic activity (150-450 kHz) [110].

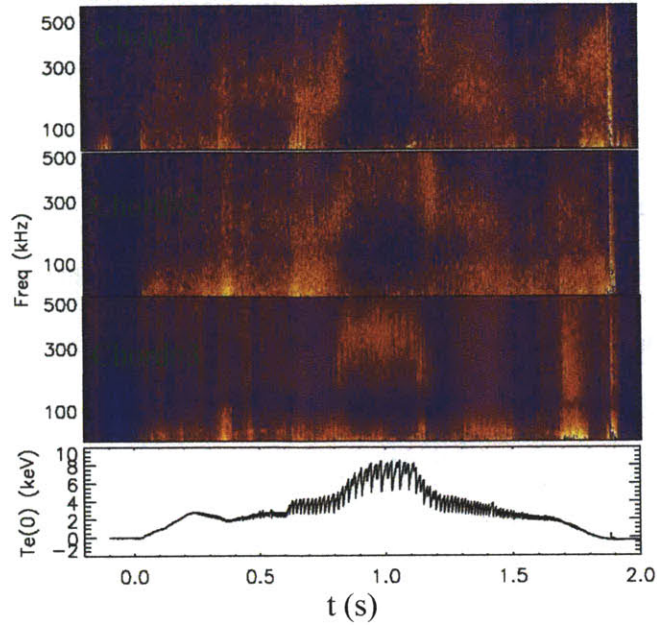


Figure 6-5: Poloidal asymmetry of WCM during I-mode observed by polarimeter. (Figure from [110])

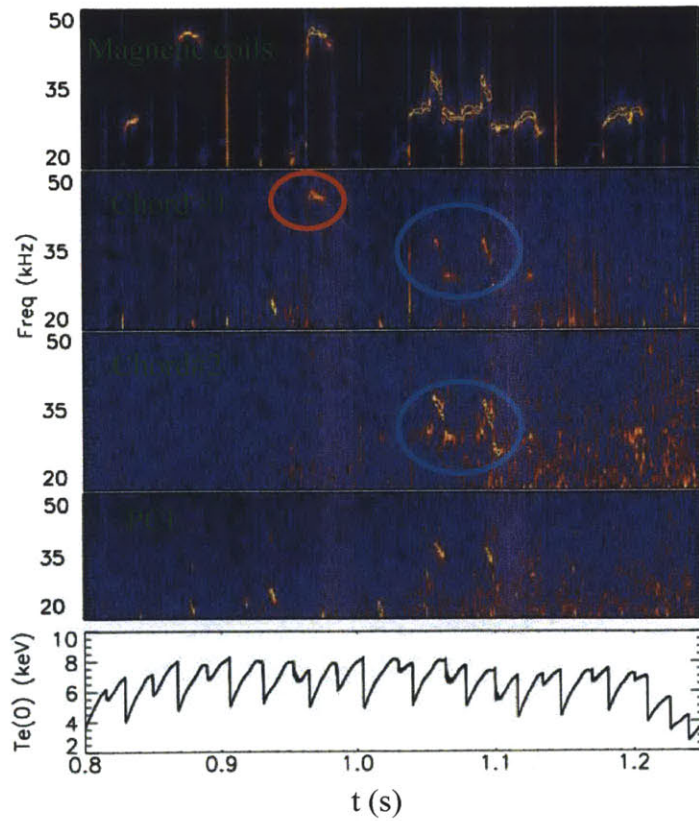


Figure 6-6: NTMs shown on polarimetry, with the same frequencies as the magnetic coil measurements, during I-mode. (Figure from [110])

While both magnetic and density fluctuations have been observed by the three-chord polarimeter, the relative strength of these two fluctuations is still unresolved. A top priority going forward is to understand the relative magnitude of the fluctuation components, and to determine how that weighting changes with different chords.

Isolating the contributions from density and magnetic fluctuations requires an upgrade to the present polarimetry system. Simultaneously measuring the density fluctuations along the same beam-path, can be achieved by adding the interferometry or C-M measurement capability to our system, which would go a long way toward isolating contributions to the fluctuation levels from magnetic and density effects. By comparing with the fluctuations found by the interferometer, we will be able to estimate the magnetic fluctuation levels seen by the polarimeter. Another way to estimate the magnetic fluctuation, without requiring an extra FIR laser, is to provide a polarimetry chord going through the mid-plane. The density fluctuation term will be zero, since there is no component of the equilibrium field parallel to the probe beams on the mid-plane. Fluctuations observed on this chord provide a direct measurement of the line-integrated radial magnetic field fluctuations. A chord on the midplane will be a high priority for any upgrade of the polarimeter.



## 7. Summary and Future Work

We have developed a three-chord polarimeter, which contributes to the LHCD study on C-Mod. It is the first time an FIR polarimeter with a poloidally viewing geometry (double pass) has been operated on a tokamak. The system has also been used to measure core magnetic fluctuations for the first time in a tokamak. Experimental results and recommended future work will be summarized in the following sections.

### 7.1 Summary

The development of the three-chord polarimetry system was introduced in chapter 3. An FIR wavelength was chosen, to achieve a measurable Faraday rotation with typical C-Mod plasma discharges, while keeping the CM effect and beam refraction in the plasma at acceptable levels. Significant efforts were taken to maximize the laser power and stabilize the lasers during the plasma discharges by designing a laser gas flowing system, laser table enclosures, an IF feedback control system and a magnetic shielding box. We also custom designed most of the FIR optics used in the system. The quartz vacuum window and waveplates were AR coated which not only enhances the optical transmission, but also reduces the laser beam ellipticity after going through a quarter-waveplate. The wire mesh beamsplitters were thoroughly tested, and meshes with optimal mesh density and mesh grid orientation were used. Custom-designed long focal length TPX lenses focus the beams down onto the retro-reflectors installed on the C-Mod inner-wall. The retro-reflectors are protected with a shutter assembly system, which can be closed during boronization or plasma disruption experiments. Three old style FIR detectors were tested, and a novel planar Schottky diode detector with much higher sensitivity has been specifically designed and fabricated for our laser wavelength. Both digital and analog phase comparators have been tested and benchmarked against each other.

In chapter 4, we describe improvements made in the polarimeter to reduce the noise level. Acoustic noise is damped with sound proofing material surrounding the enclosures and lasers. The lasers and optics are all secured on stable optical tables to reduce vibration noise. Since the vibrations were coupled to the lasers through the original metal pumping lines, we replaced the lines with Teflon pipes, and moved the laser coolers and vacuum pumps as far away from the lasers as possible. The laser beam co-linearity was optimized by using a 2D pyroelectric camera. Spurious reflections were taken care of by dumping the unused beams onto FIR absorption materials, and replacing the corner-cube detectors with the new detectors which could be optimized to reduce reflections. Phase errors induced by TF ramps were studied, and the baseline drift problem was found to be mitigated by programming the TF to start 100 ms earlier than usual. System calibration found the phase error from the beam polarization change is less than 5%. After dealing with these sources of noise, the polarimeter was found to be sensitive to plasma density changes, current changes and plasma position sweeps. All three chords observe the sawtooth crash events with very good time resolution.

In chapter 5, we used the polarimeter to infer current density profile changes during LHCD experiments. The current profile was confirmed to be flattened by the application of LH power, and to peak after the LH was turned off. The driven current increases with the LH power, and decreases with higher plasma densities (weak driven current beyond  $n_e=1.0 \times 10^{20}/\text{m}^3$ ). The driven current was observed to have significant components close to the plasma edge with a high plasma current ( $I_p \approx 820$  kA), consistent with the CQL3D predictions. The polarimeter observed better current driven efficiency for lower LH phasing during both a shot-by-shot and a within-shot LH phase scan. The polarimeter was also used to benchmark reconstructions from both normal EFIT and Kinetic-EFIT. Synthetic polarimetry signals from Kinetic-EFIT agree with the measurements much better than those from the normal EFIT during LHCD, indicating more accurate internal magnetic field reconstruction for Kinetic-EFIT. Polarimetry measurements were

used to constrain the central safety factor  $q_0$  in EFIT, which shows the current profile is broadened and in some of the particular cases studied,  $q_0$  increases to  $\sim 2$  with LH.

Polarimetry fluctuation measurements were presented in chapter 6. Both density and magnetic fluctuations can be captured by the polarimeter. It not only observed fluctuation features consistent with observations from other diagnostics, such as QCM, WCM, NTMs, sawtooth precursors and snakes, but also was used to discover a new class of core broadband magnetic fluctuations during EDA H-mode. The broadband fluctuations were then suppressed by the LH waves, which may be explained by increased ExB shear. The polarimeter also confirmed the poloidal asymmetry of the WCM during I-mode operation.

## 7.2 Future work

Since the FIR lasers are sensitive to stray magnetic fields and vibrational noise, it is beneficial to move the lasers away from C-Mod. The lasers were moved into an interface room after the 2012 C-Mod run campaign. The room has a concrete floor, and good temperature control, and the laser vacuum pumps and coolers will be installed in a neighboring room. Therefore, the lasers can operate in a quiet and temperature controlled environment. The magnetic field in this room is only  $\sim 3$  G during the plasma discharge, so that the shielding box will not be necessary. The lasers beam will be directed onto the vertical table in the cell using only two more mirror reflections. The total beam path increases from  $\sim 14$  to  $\sim 24$  m with the new optical layout, but the beam size on the vertical table will not change appreciably because of the rather large diameter of the beam (long Rayleigh length).

The next system upgrade will be to enhance the system to allow measurements along at least six horizontally viewing chords, with one chord below the magnetic axis, which should allow direct measurement of the central safety factor without the need for profile inversion [55][56]. A radial chord going through the magnetic axis will also benefit the measurement of the magnetic fluctuations, since the effects of density fluctuations should be negligible on the

midplane, where the equilibrium magnetic fields are perpendicular to the beam path. More space near the horizontal port is needed to achieve this multi-chord upgrade, and thus we might need to relocate some existing diagnostics sharing the same port window with the polarimeter. A separate vacuum window will be used for each chord, so that we can use small thin windows with very little absorption and with the thickness chosen to act as an etalon.

Another important upgrade is incorporating the interferometric measurement capability into the polarimeter, by adding a third FIR laser [45][47]. In this configuration, either density/current profiles or density/magnetic fluctuations can be measured simultaneously.

The polarimeter has been used to constrain  $q_0$  as described in this thesis. A step going forward is to constrain the whole safety factor or current density profile. With more polarimetry measurement chords available in the future, parametric fitting for these profiles will also be available. The current density profile from both the polarimetry-EFIT and parametric fitting can be compared to the Kinetic-EFIT current profile and CQL3D simulations. The evolution of the current density profiles during sawtooth crashes, and with LHCD will be further analyzed. It is also interesting to measure the current density profile changes during plasma disruptions and current ramp experiments. Controlling the current density or safety factor profiles in real-time requires a real time measurement, and polarimetry can provide this with excellent time resolution.

## Bibliography

- [1] J. D. Lawson. "Some criteria for a power producing thermonuclear reactor", Proceedings of the Physical Society 70, 6 (1957).
- [2] E. Moses. "The National Ignition Campaign: Status and Progress", 24<sup>th</sup> International IAEA Fusion Energy Conference, (2012).
- [3] J. P. Freidberg. Plasma Physics and Fusion Energy, (2007).
- [4] V. P. Smirnov. "Tokamak foundation in USSR/Russia 1950–1990." Nuclear Fusion 50, 014003 (2010).
- [5] F. F. Chen. Introduction to Plasma Physics, (1974)
- [6] [www.efda.org/2011/09/tokamak-principle-2/](http://www.efda.org/2011/09/tokamak-principle-2/)
- [7] I. H. Hutchinson, R. Boivin, F. Bombarda, P. Bonoli, S. Fairfax, C. Fiore, J. Goetz et al. "First results from Alcator C-Mod." Physics of Plasmas 1, 1511 (1994).
- [8] S. J. Wukitch, P. T. Bonoli, E. Nelson-Melby, M. Porkolab et al. "ICRH and Current Ramp-up Experiments in Alcator C-Mod", EPS, (1998).
- [9] S. J. Wukitch, Y. Lin, A. Parisot, J. C. Wright et al. "Ion cyclotron range of frequency mode conversion physics in Alcator C-Mod: Experimental measurements and modelling", Physics of Plasmas 12, 056104 (2005).
- [10] N. P. Basse, A. Dominguez, E. M. Edlund, C. L. Fiore, R. S. Granetz, A. E. Hubbard, J. W. Hughes et al. "Diagnostic systems on alcator C-mod." Fusion science and technology 51, 476(2007).
- [11] E. S. Marmor, M. Porkolab, I. H. Hutchinson. "Alcator C-Mod National Tokamak Facility Five Year Research Plan (2008-2013) ", (2008).
- [12] J. Ko, Steve Scott, Manfred Bitter, and Scott Lerner. "Design of a new optical system for Alcator C-Mod motional Stark effect diagnostic." Review of Scientific Instruments 79, 10F520 (2008).
- [13] J. Ko, Current Profile Measurements Using MSE on Alcator C-Mod, PhD Thesis, (2009)
- [14] R. Mumgaard, S. Scott, R. Granetz. "Real-time MSE polarization background subtraction and simultaneous MSE  $\sigma$  and  $\pi$  measurement on Alcator C-Mod", 54<sup>th</sup> APS-DPP, (2012).
- [15] T. C. Luke. "Measurement of Particle Transport Coefficients on Alcator C-Mod", PhD Thesis, (1994).
- [16] D. Ernst. Private communication.
- [17] Y. Ma. "Study of H-mod access conditions on the Alcator C-Mod tokamak", PhD thesis, (2012).

- [18] L. L. Lao, H. St. John, R. D. Stambaugh, A. G. Kellman, W. Pfeiffer. "Reconstruction of current profile parameters and plasma shapes in Tokamaks." *Nuclear Fusion* 25, 1611 (1985).
- [19] L. L. Lao, J. R. Ferron, R. J. Groebner, W. Howl., H. St. John, E. J. Strait, T. S. Taylor. "Equilibrium analysis of current profiles in Tokamaks", *Nuclear Fusion* 30, 1035 (1990).
- [20] <http://www.mdsplus.org/index.php/Introduction>
- [21] S. Shiraiwa. "Progress in LHCD Modeling and Experiments towards AT Regime on Alcator C-Mod", 53<sup>rd</sup> APS-DPP, (2011).
- [22] N. J. Fisch. "Theory of current drive in plasma", *Review of Modern Physics* 59, 175 (1987).
- [23] R. A. James, G. Giruzzi, B. de Gentile, L. Rodriguez, R. Harvey et al. "Electron-cyclotron-current-drive experiments in the DIII-D tokamak." *Physics review A*, (1992).
- [24] A. G. Peeters. "The bootstrap current and its consequences." *Plasma Physics and Controlled Fusion* 42, B231 (2000).
- [25] G. M. Wallace. "Behavior of Lower Hybrid Waves in the Scrape Off Layer of a Diverted Tokamak", PhD Thesis, (2010).
- [26] A. P. Smirnov, R. W. Harvey. "Calculations of the Current Drive in DIII-D with the GENRAY Ray Tracing Code." 37<sup>th</sup> APS-DPP, (1995).
- [27] O. Meneghini, S. Shiraiwa, and R. Parker. "Full wave simulation of Lower Hybrid waves in Maxwellian plasma based on the finite element method." *Physics of Plasmas* 16, 090701 (2009).
- [28] R. W. Harvey, M. G. McCoy. "The CQL3D Fokker-Planck Code." IAEA Technical Committee Meeting on Advances in Simulation and Modeling of Thermonuclear Plasma, (1992).
- [29] J. E. Liptac. "Lower Hybrid Modeling and Experiments on Alcator C-Mod" PhD Thesis, (2006).
- [30] J. Chen, G. Zhuang, Z. J. Wang, L. Gao, Q. Li, W. Chen, D. L. Brower, and W. X. Ding. "First results from the J-TEXT high-resolution three-wave polarimeter-interferometer." *Rev. Sci. Instrum.* 83,10E306 (2012).
- [31] J. Zhang, W. A. Peebles, T. A. Carter, N. A. Crocker, E. J. Doyle et al. "Design of a millimeter-wave polarimeter for NSTX-Upgrade and initial test on DIII-D." *Rev.Sci. Instrum.* 83,10E321(2012).
- [32] F. De Marco, and S. E. Segre. "The polarization of an em wave propagating in a plasma with magnetic shear. The measurement of poloidal magnetic field in a Tokamak." *Plasma Physics* 14, 245(1972).
- [33] H. Soltwisch. "Current Distribution Measurement in a Tokamak by FIR polarimetry." *Rev. Sci. Instrum.* 57, 1939 (1986)

- [34] B. W. Rice. "Fifteen chord FIR polarimetry system on MTX." *Rev. Sci. Instrum.* 63, 5002 (1992).
- [35] G. Dodel and W. Kunz. "A far-infrared 'polari-interferometer' for simultaneous electron density and magnetic field measurements in plasmas", *Infrared Phys.* 18, 773 (1978).
- [36] J. Zhang, W. A. Peebles, T. A. Carter, N. A. Crocker, E. J. Doyle, S. Kubota, T. L. Rhodes, G. Wang, L. Zeng. "Initial tests of NSTX-U millimetre-wave Polarimeter on DIII-D", 54<sup>th</sup> APS-DPP, (2012)
- [37] Y. Kawano, S. Chiba, H. Shirai, A. Inoue, A. Nagashima. "First Measurement of Tangential Faraday Rotation of CO<sub>2</sub> Laser Wave in a Tokamak Plasma." *Rev. Sci. Instrum.* 70, 1430 (1999).
- [38] I. H. Hutchinson. *Principles of Plasma Diagnostics*, (2005).
- [39] S. E. Segre. "A Review of Plasma Polarimetry-Theory and Methods." *Plasma Phys. Control. Fusion* 41, R57(1999).
- [40] S. E. Segre and V. Zanza. "Derivation of the Pure Faraday and Cotton-Mouton effects when polarimetric effects in a Tokamak are Large." *Plasma Phys. Control. Fusion* 48, 339 (2006).
- [41] G. Braithwaite, N. Gottardi, G. Magyar, J. O'Rourke, J. Ryan, D. Veron. "JET Polari-interferometer." *Rev. Sci. Instrum.* 60, 1989.
- [42] A. C. A. P. van Lammeren, S. K. Kim, A. J. H. Donne. "Multichannel Interferometer/Polarimeter System for the RTP tokamak." *Rev. Sci. Instrum.* 61, 2882 (1990)
- [43] J.-L. Lachambre, M. Gagne. "Multichannel Submillimeter Interferometer/Polarimeter for Tdev." *Rev. Sci. Instrum.* 65, 3428 (1994)
- [44] M. O'Gorman, E. Zilli, L. Giudicotti, S. Prunty et al. "The Multichord Far Infrared Polarimeter of the RFX Experiment", 1063 (2000)
- [45] B. H. Deng, D. L. Brower, W. X. Ding, M. D. Wyman et al. "High-speed Three-wave Polarimeter-interferometer Diagnostic for Madison Symmetric Torus." *Rev. Sci. Instrum.* 77, 10F108 (2006).
- [46] A. J. H. Donne. "High Spatial Resolution Interferometry and Polarimetry in hot plasmas. " *Rev. Sci. Instrum.* 66, 3407 (1995).
- [47] J. H. Rommers, J. Howard. "A New Scheme for Heterodyne Polarimetry with High Temporal Resolution." *Plasma Phys. Control. Fusion* 38, 1805 (1996).
- [48] Y. Kawano, S. Chiba, A. Inoue. "Infrared Laser Polarimetry for Electron Density Measurement in Tokamak Plasmas." *Rev. Sci. Instrum* 72, 1068 (2001).
- [49] K. Smith. "Results from Prototype Polarimeter/Interferometer on Alcator C-Mod." Master Thesis. 2007.

- [50] T. Akiyama, K. Kawahata, S. Okajima, K. Nakayama, T. C. Oakberg. "Bench Testing of New Polarimeter with Silicon Photoelastic Modulator for Short Wavelength FIR Laser." *Plasma and Fusion Research* 2, S1113 (2007).
- [51] T. Akiyama, S. Tsuji-lio, R. Shimada, N. Nakayama et al. "CO<sub>2</sub> Laser Polarimeter for Electron Density Profile Measurement on the Large Helical Device." *Rev. Sci. Instrum.* 74, 2695 (2003).
- [52] T. Kondoh, Y. Kawano, A. E. Costley, A. Malaquias, T. Sugie, C. Walker. "Toroidal Interferometer/Polarimeter Density Measurement System for Long Pulse Operation on ITER." 30<sup>th</sup> EPS Conf. on Contr. Fusion and Plasma Phys. 27A (2003).
- [53] G. H. Golub, C. Reinsch. "Singular Value Decomposition and Least Squares Solutions." *Numer. Math.* 14, 403 (1970).
- [54] W. R. Geck, C. W. Domier, N. C. Luhmann. "Multiple View Fan Beam Polarimetry on Tokamak Devices." *Rev. Sci. Instrum.* 68, 416 (1996).
- [55] J. H. Rommers. "Faraday Rotation Measurements in the RTP Tokamak." PhD Thesis.(1996)
- [56] D.L. Brower, W.X. Ding, and S.D. Terry. "Measurement of the Current-Density Profile and Plasma Dynamics in the Reversed-Field Pinch", *Physics Review Letters*, 88, No.18 (2002)
- [57] E.Russell and E.Bell. "Measurement of the Optical Constants of Crystal Quartz in the Far Infrared with the Asymmetric Fourier-Transform Method", *Journal of the Optical Society of America*, 57, number 3 (1967)
- [58] J. H. Rommers, A. J. H. Donne, and F. A. Karelse, "The multichannel triple-laser interferometer/ polarimeter system at RTP", *Rev. Sci. Instrum.* 68, 1217 (1997)
- [59] N. E. Lanier, J. K. Anderson, C. B. Forest, D. Holly et al. "First Results from the Far-infrared Polarimeter System on the Madison Symmetric Torus Reversed Field Pinch. " *Rev. Sci. Instrum.* 70, 718 (1999).
- [60] F. Auriemma, M. Brombin, A. Canton, L. Giudicotti, P. Innocente, R. Lorenzini, E. Zilli, "Characterization of magnetic field profiles at RFX-mod by Faraday rotation measurements", 51<sup>th</sup> APS Division of Plasma Physics, (2009).
- [61] K. Kawahata, T. Akiyama, K. Tanaka, K. Nakayama and S. Okajima. "Development of Two Color Laser Diagnostics for the ITER Poloidal Polarimeter", 15<sup>th</sup> International Symposium on Laser-Aided Plasma Diagnostics (2011)
- [62] S. Barry and C. Nieswand, S. L. Prunty, H. M. Mansfield, and P. O'Leary. "Beach test results on a new technique for far-infrared polarimetry", *Rev. Sci. Instrum.* 68, 2037 (1997)
- [63] [http://www.farran.com/index.php?option=com\\_content&task=view&id=81&Itemid=47](http://www.farran.com/index.php?option=com_content&task=view&id=81&Itemid=47)
- [64] Y. Jiang, D.L. Brower, L. Zeng, J. Howard. "Application of digital phase comparator technique to interferometer data", *Rev. Sci. Instrum.* 68, 902 (1997).
- [65] A. J. H. Donne. "Design study for the ITER polarimetry diagnostic", EFDA Technology Workprogramme (2002)

- [66] T. Yamaguchi, Y. Kawano, H. Fujieda, K. Kurihara, M. Sugihara and Y. Kusama. "Optimization of the viewing chord arrangement of the ITER poloidal Polarimeter", *Plasma Phys. Control. Fusion* 50, 045004 (2008)
- [67] W. X. Ding, D. L. Brower, W. F. Bergerson and L. Lin. "Upgrade of far-infrared laser-based Faraday rotation measurement on MST", *Rev. Sci. Instrum.* 81, 10D508 (2010)
- [68] L. Lin, W. X. Ding, D. L. Brower, W. F. Bergerson and T. F. Yates. "Differential interferometry for measurement of density fluctuations and fluctuation-induced transport", *Rev. Sci. Instrum.* 81, 10D509 (2010)
- [69] Jin-Seok Ko. "Current Profile Measurements Using MSE on Alcator C-Mod", PhD Thesis, (2009).
- [70] R. J. Hastie. "Sawtooth Instability in Tokamak Plasma", *Astrophysics and Space Science* 256, 177 (1998)
- [71] S. D. Terry, D. L. Brower, and W. X. Ding. "Measurement of current profile dynamics in the Madison Symmetric Torus." *Physics of Plasmas* 11, (2004)
- [72] S. Ishida, N. Isei, M. Sato. "Operation of a 20-channel grating polychromator diagnostic system and its application to sawtooth observations in JT-60U." Technical report, (1992).
- [73] Y. Peysson and Tore Supra Team. "High Power Lower Hybrid Current Drive Experiments in the Tore Supra Tokamak." *Nuclear Fusion* 41, 1703 (2001).
- [74] A. Ekedahl, G. Granucci, J. Mailloux, Y. Baranov et al. "Long Distance Coupling of Lower Hybrid Waves in JET Plasmas with Edge and Core Transport Barriers." *Nuclear Fusion* 45, 351 (2005).
- [75] V. Pericoli Ridolfini, P. Bibet, F. Mirizzi, M. L. Apicella et al. "LHCD and Coupling Experiments with an ITER-like PAM Launcher on the FTU Tokamak." *Nuclear Fusion* 45, 1085 (2005)
- [76] M. Seki, S. Moriyama, S. Shinozaki, K. Hasegawa, S. Hiranai et al. "Performance of the LH antenna with Carbon Grill in JT-60U." *Fusion Engineering and Design* 74, 273(2005).
- [77] P. T. Bonoli, J. Ko, R. Parker, A. E. Schmidt, G. Wallace, J. C. Wright, C. L. Fiore et al. "Lower hybrid current drive experiments on Alcator C-Mod: Comparison with theory and simulation." *Physics of Plasmas* 15, 056117 (2008).
- [78] G. M. Wallace, A. E. Hubbard, P. T. Bonoli, I. C. Faust, R. W. Harvey, J. W. Hughes, B. L. LaBombard et al. "Lower hybrid current drive at high density in Alcator C-Mod." *Nuclear Fusion* 51, 083032 (2011).
- [79] G. M. Wallace, I. C. Faust, O. Meneghini, R. R. Parker, S. Shiraiwa, S. G. Baek, P. T. Bonoli et al. "Lower hybrid current drive at high density in the multi-pass regime." *Physics of Plasmas*, 062505 (2012)
- [80] A. E.W. Schmidt. "Measurements and Modeling of Driven Fast Electrons on Alcator C-Mod", PhD Thesis, (2011).

- [81] R. Parker, P. Bonoli, O. Meneghini, S. Shiraiwa et al. "Progress Toward Steady-State Regimes with LHCD in Alcator C-Mod", 54<sup>th</sup> APS division of plasma physics (2012).
- [82] Y. A. Podpaly. "Rotation Generation and Transport in Tokamak Plasma", PhD Thesis, (2011).
- [83] A. Boboc, L. Zabeo, and A. Murari. "Simultaneous Cotton-Mouton and Faraday rotation angle measurements on JET." *Rev. Sci. Instrum.* 77, 10F324 (2006).
- [84] L. Zabeo, A. Murari, E. Joffrin, D. Mazon, and C. Taliercio. "A versatile method for the real time determination of the safety factor and density profiles in JET." *Plasma physics and controlled fusion* 44, 2483 (2002).
- [85] D. Mazon, X. Litaudon, D. Moreau, V. Pericoli-Ridolfini, L. Zabeo, F. Crisanti, P. De Vries et al. "Active control of the current density profile in JET." *Plasma physics and controlled fusion* 45, L47 (2003).
- [86] D. Mazon, J. Blum, C. Boulbe, B. Faugeras, A. Boboc, M. Brix, P. De Vries, S. Sharapov, and L. Zabeo. "Real-time identification of the current density profile in the JET Tokamak: method and validation." *Proceedings of the 48th IEEE Conference*, 285 (2009).
- [87] J. W. Hughes, A. E. Hubbard, D. A. Mossessian, B. LaBombard, T. M. Biewer et al. "H-mode pedestal and L-H transition studies on Alcator C-mod." *Fusion science and technology* 51, 317 (2007).
- [88] Greenwald, M., R. Boivin, P. Bonoli, C. Fiore, J. Goetz, R. Granetz, A. Hubbard et al. "Studies of EDA H-mode in Alcator C-Mod." *Plasma Physics and Controlled Fusion* 42, A263 (2000).
- [89] D. G. Whyte, A. E. Hubbard, J. W. Hughes, B. Lipschultz, J. E. Rice, E. S. Marmor, M. Greenwald et al. "I-mode: an H-mode energy confinement regime with L-mode particle transport in Alcator C-Mod." *Nuclear Fusion* 50, 105005 (2010).
- [90] A. E. Hubbard, D. G. Whyte, R. M. Churchill, I. Cziegler, A. Dominguez, T. Golfinopoulos, J. W. Hughes et al. "Edge energy transport barrier and turbulence in the I-mode regime on Alcator C-Mod." *Physics of Plasmas* 18, 056115 (2011).
- [91] A. Dominguez. "Study of Density Fluctuations and Particle Transport at the Edge of I-Mode Plasma." PhD Thesis (2012)
- [92] Y. Lin, R. S. Granetz, A. E. Hubbard, M. L. Reinke, J. E. Rice, S. M. Wolfe, and S. J. Wukitch. "Characterization of neo-classical tearing modes in high-performance I-mode plasmas with ICRF mode conversion flow drive on Alcator C-Mod." *IAEA Fusion Energy Conference* (2012).
- [93] ASDEX Team. "The H-Mode of ASDEX", *Nucl. Fusion* 29, 1959(1989).
- [94] F. Ryter, K. Buchl, C. Fuchs, O. Gehre, O. Gruber, A. Herrmann, A. Kallenbach et al. "H-mode results in ASDEX Upgrade." *Plasma physics and controlled fusion* 36, A99 (1994).

- [95] D. J. Campbell, A. Bickley, A. Chankin, S. Clement, S. J. Davies, J. Ehrenberg, S. K. Erents et al. "Studies of reactor-relevant H-mode regimes in the JET-pumped divertor." *Plasma Physics and Controlled Fusion* 38, 1497 (1996).
- [96] M. Porkolab, J. C. Rost, N. Basse, J. Dorris, E. Edlund, L. Lin, Y. Lin, and S. Wukitch. "Phase contrast imaging of waves and instabilities in high temperature magnetized fusion plasmas." *Plasma Science, IEEE Transactions on* 34, 229 (2006).
- [97] X. Q. Xu, R. H. Cohen, T. D. Rognien, and J. R. Myra. "Low-to-high confinement transition simulations in divertor geometry." *Physics of Plasmas*, 1951(2000)
- [98] B. D. Dudson, M. V. Umansky, X. Q. Xu, P. B. Snyder, and H. R. Wilson. "BOUT++: a framework for parallel plasma fluid simulations." *Computer Phy. Communications* 180, 1467 (2009)
- [99] A. Mazurenko, M. Porkolab, D. Mossessian, and J. A. Snipes et al. "Experimental and Theoretical Study of Quasicoherent Fluctuations in Enhanced  $D_{\alpha}$  Plasmas in the Alcator C-Mod Tokamak." *Physical Review letters*, 225004 (2002)
- [100] J. W. Hughes, P. B. Snyder, X. Xu, J. R. Walk, E. M. Davis, R. M. Churchill, R. J. Groebner et al. "Pedestal stability and transport on the Alcator C-Mod tokamak: experiments in support of developing predictive capability." 24<sup>th</sup> IAEA Fusion Energy Conference (2012)
- [101] B. N. Rogers, J. F. Drake and A. Zeiler. "Phase Space of Tokamak Edge Turbulence, the L-H Transition and the Formation of the Edge Pedestal." *Physical Review Letters*, 4396 (1998)
- [102] B. LaBombard. Private communication, (2013)
- [103] P. Ennever, M. Porkolab, J. Candy et al. Gyrokinetic Simulations of Impurity Seeded Ohmic Plasmas in Alcator C-Mod and Comparisons. E.U. Joint Transport Task Force Workshop (2013)
- [104] J. Terry. "Effects of LH on edge/SOL turbulence as seen in run 1120725", C-Mod Science Meeting, July30,2012.
- [105] A. Ince-Cushman, J. E. Rice, M. Bitter, M. L. Reinke, K. W. Hill, M. F. Gu, E. Eikenberry et al. "Spatially resolved high resolution x-ray spectroscopy for magnetically confined fusion plasmas." *Rev. Sci. Instrum.* 79, 10E302-10E302 (2008).
- [106] M. Reinke, Y. A. Podpaly, M. Bitter, I. H. Hutchinson, J. E. Rice, L. Delgado-Aparicio, C. Gao et al. "X-ray imaging crystal spectroscopy for use in plasma transport research." *Rev. Sci. Instrum.* 83, 113504-113504 (2012).
- [107] T. S. Hahm. "Rotation shear induced fluctuation decorrelation in a toroidal plasma", *Physics of Plasma* 1, 2940 (1994).
- [108] M. Barnes, F. I. Parra, E. G. Highcock, A. A. Schekochihin et al. "Turbulent Transport in a Tokamak Plasmas with Rotational Shear", *Phys. Rev. Lett*, 175004(2011).
- [109] D. G. Whyte, N. Tsujii, A. White, S. Wolfe, D. Pace. "Is the WCM poloidally centered at the outer midplane?" C-Mod Weekly Science Meeting (4/19/2011)

[110] W. F. Bergerson., P. Xu, D. L. Brower, W. X. Ding, and J. H. Irby. "C-Mod Polarimeter Development and Application to Magnetic Fluctuation Measurements." APS 56<sup>th</sup> Annual Meeting of the Division of Plasma Physics (2012)